Near Infrared Laser Spectroscopy

of Carbon-containing Plasmas

YEUNG, Shun Hin

A Thesis Submitted in Partial Fulfillment

of the Requirements for the Degree of

Doctor of Philosophy

in

Chemistry

The Chinese University of Hong Kong

March 2010

UMI Number: 3445945

UMI®

Dissertation Publishing

ProQuest®

THESIS/ASSESSMENT COMMITTEE

Prof. Zhifeng LIU (Chair)

Prof. Man Chor CHAN (Thesis Supervisor)

Prof. Sik Lok LAM (Committee Member)

Prof. Allan Shi Chung CHEUNG (External examiner)

Prof. Kentarou KAWAGUCHI (External examiner)

ABSTRACT

This thesis reports the construction of a custom-designed experimental setup for the high resolution near infrared spectroscopic studies of molecular ions and radicals generated in gaseous plasma. The home-built near infrared spectrometer system has a frequency resolution of 500 kHz and a frequency accuracy of ~0.0010 cm^{-1} with a detection sensitivity of $\Delta I/I$ of 10^{-6} using zero background concentration modulated phase sensitive detection scheme. An in-house program has been designed for data acquisition, frequency calibration and data processing and storage.

The unprecedented sensitivity and resolution achieved by our spectrometer allows the measurement of the very weak Phillips band system ($A^1\Pi_u$ - $X^1\Sigma_g^+$) of C$_2$ in the plasma of methane and helium at a ratio of 1:170 generated under very mild *ac* hollow cathode discharge conditions. A total of eleven vibronic bands of the Phillips system have been observed in the region from 10300 cm^{-1} to 14250 cm^{-1} and analyzed based on the previous work. Combining the observed transition frequencies with those from Douay *et al.* [*J. Mol. Spectrosc.* **131**, 250 (1988)], a set of spectroscopic constants for both the $X^1\Sigma_g^+$ and $A^1\Pi_u$ states have been obtained using least-squares fitting. Excellent agreement has been found between determined molecular constants and those found in the literature. The observation

of the high v levels in the ${}^{1}\Pi_{u}$ state allows the determination of high order anharmonic constants $\omega_{e}z_{e}$ and $\omega_{e}a_{e}$ for the first time.

In addition, two unknown vibronic bands have been observed in the 12150 cm^{-1} region and 12450 cm^{-1} region. From the observed linewidths, isotopic shift of the transition frequency and appearance of intricate spectral pattern, it is plausible that these bands may be due to C_2 under the perturbation of a state inaccessible by dipole transition. Further analysis of these bands are underway.

Submitted by YEUNG Shun Hin

for the degree of Doctor of Philosophy in Chemistry

at The Chinese University of Hong Kong in March 2010.

摘要

這篇論文論述了我們如何建造一套特定設計的實驗裝置，而分析一些透過等離子體所產生之離子和自由基的高分辨近紅外光光譜之研究。我們利用具有頻率分辨率為 500 千赫和頻率精度為 ~0.0010 cm⁻¹ 的自製紅外光光譜儀系統，並配合零背景濃度調頻技術之下，能使檢測靈敏度 $\Delta I/I$ 提昇至百萬分之一。另外，一副自設的電腦程式可以同時用於數據採集，頻率校準和數據處理及存儲。

由於我們的光譜儀具有很好靈敏度和分辨率，因而使我們能夠測量非常薄弱的雙碳菲利普斯系統〔$A^1\Pi_u - X^1\Sigma_g^+$〕。透過交流空心陰極放電站之下，來使甲烷和氦混合物〔比例 1：170〕產生放電作用，並使我們在波數段 10300 cm⁻¹ 至 14250 cm⁻¹ 之中觀察到一共十一條振動帶的吸收光譜。然後，透過合併我們和 Douay 們的實驗結果，我們用最小二乘法擬合得到一組高準確度的光譜常數，並且與文獻所載的十分吻合。基於所觀察 $A^1\Pi_u$ 電子態是屬於高振動能級，所以我們可以首次確定高階非諧性振動常數〔$\omega_e z_e$〕和〔$\omega_e a_e$〕。

此外，我們還能夠測量兩條不知明的振動帶〔分別在 12150 cm⁻¹ 至 12450 cm⁻¹ 之中〕。從觀察到的線寬，同位素變化的躍遷轉換頻率和光譜的外觀模式，我們有理由認為這些振動帶可能是由於一些擾動之下所形成的。因此，我們有需要進一步分析這些振動帶。

ACKNOWLEDGEMENTS

TABLE OF CONTENTS

LIST OF FIGURES

LIST OF TABLES

To my love, Rita

Chapter 1

Introduction

Molecules are the building block of matter of any kind. Molecules can be found everywhere, including all living and non-living matter, materials, atmosphere, the Earth and outer space such as the Sun, interstellar media and *etc*. Chemistry, as a science to investigate and manipulate matter at the molecular level, emphasizes on the understanding of molecular systems. Molecular spectroscopy provides the experimental and theoretical basis for the determination of molecular structure and dynamics.

As one of the oldest sciences to study interactions of light and molecules, molecular spectroscopy was initiated by Isaac Newton[1] in the 15th century. In his extraordinary experiment, Newton was able to obtain the emission spectrum of the Sun by dispersion technique using prisms and lenses. Over the years, spectroscopy has evolved from a purely observational science to a fundamental means in understanding the structural and dynamic properties of molecular systems.

The correlation between spectra and structure and dynamics was first pointed out by Herzberg in his three volumes of classic books[2, 3 and 4] in the 1940s. This monumental work marked the beginning of modern spectroscopy. In these concise

texts, detailed discussion on structure and spectroscopy was presented using the theory of quantum mechanics. Following this lead, many developments have been made throughout 1950s to 1980s.[5]

The advancement of laser radiation sources in the 1970s has led to revolutionary developments in molecular spectroscopy. The much improved resolution in frequency and sensitivity brought by laser sources allow the observation of very detailed structures in the spectra of molecules at very low concentration. Numerous interesting molecular systems such as radicals,[6] van der Waals complexes,[7] molecular ions,[6] as well as quantum crystals[8] have been extensively studied using laser spectroscopy. In addition to the wealth of structural information, various dynamic information on tunneling and intermolecular interactions can also be obtained from the detailed features in the spectra.[7]

The study of molecular ions and radicals, species known as "reactive species" because of their short lifetime (in order of $\lesssim 10^{-2} \sim 10^{-6}$ s), is important in understanding mechanisms of chemical reactions since they often act as reactive intermediates or transition states. For instance, carbene radicals (CH_2) have been involved in various organic reactions as an intermediate. In addition, some species exhibit intriguing quantum mechanical phenomenon such as the scrambling of protons in $C_2H_3^+$ [9] and CH_5^+ [10] and inversion tunneling of H_3O^+ [11] that is of great

academic interest. Molecular ions and radicals also play important roles in astrochemistry of the interstellar medium[12] under low temperature and low pressure conditions. Studies of molecular ions and radicals therefore provide some insights in understanding the formation of complex molecules (*e.g.* the chemistry of carbon family[13] and nitrogen family)[13] in the early stage of star evolution. Hence, the studies of molecular ions post great challenge yet great interest.

In pursuing the spectroscopic studies of molecular ions and radicals, we have built a state-of-the-art experimental setup to carry out *in situ* measurements in weakly ionized plasmas generated by high power (high current and high voltage) alternating current (*ac*) gas discharges in a hollow cathode discharge tube. As discussed in the following chapters, this approach produces reactive species with sufficient abundance for spectroscopic observations.

During my residence as a graduate student, I have mainly involved in constructing and testing the apparatus for spectroscopic studies of molecular ions and radicals. The apparatus built for this work includes a near infrared (NIR) high resolution laser spectrometer, a high voltage *ac* discharge power supply and a hollow cathode discharge cell. Using these equipments a number of plasma systems have been studied.

In this dissertation, the details of this work will be presented. An extensive

description of the apparatus will be given in Chapter 2. The general scheme in the

production of the reactive species and their detection will also be discussed. In

Chapter 3, our recent work on the Phillips system of C_2 radical generated in CH_4/He

plasma will be discussed. In Chapter 4, a brief discussion and conclusion will be

presented.

Chapter 2

Experimental Apparatus

2A. Overview

In pursuing spectroscopic studies of reactive species (molecular ions and radicals) in the gas phase, a number of criteria must be fulfilled. First of all, the species of interest must be produced with sufficient abundance that is within the detection limit of the instrument. One of the most widely used techniques is based on the high voltage discharges of parent gas with large amount of buffer gas. Depending the nature of discharges, the discharge conditions as well as discharge products are different. Common discharge techniques are *ac* glow discharges,[14] *ac* hollow cathode discharges,[15] microwave discharges[16] and *etc*. The *ac* hollow cathode discharges, which allow high discharge current, were used in this work.

The typical concentration of reactive species produced in the discharges is on the order of ppm (part per million) level. This low abundance posts a challenge for their detection. Multi-traversal technique together with zero-background phase-sensitive detection based on the modulation of absorption signals were employed in our study to achieve a fractional sensitivity of $\Delta I/I \sim 10^{-6}$. As shown in the following chapters, the very weak Phillips system and the $\Delta v = -4$ sequence of the

Swan system of C_2 were observed with a typical signal-to-noise (S/N) ratio of 10-20.

A home-built high resolution spectrometer covering the range of 10000 to 14500 cm^{-1} based on a continuous wave (cw) Titanium-doped sapphire ring laser source was used to study the transitions between low lying electronic states and overtones of the species produced in the plasma systems. The high spectral purity of the source allows to record the spectra at Doppler-limited resolution. Two carbon-containing species produced by the *ac* hollow cathode discharges have been studied using concentration modulation technique. In the CH_4/He plasma, the absorption spectrum of very weak Phillips system was observed while in the C_2H_2/He plasma, the absorption spectra of both the Phillips and Swan systems have been observed at unprecedented accuracy and sensitivity. In the following, the detailed experimental setup will be discussed.

2B. Near infrared laser spectrometer

The schematic diagram of our home-built high resolution near infrared laser spectrometer is shown in Fig. 1. The centerpiece of the instrument is the Titanium-doped sapphire (Ti:sapphire) ring laser source (COHERENT 899-21), which is optically pumped by a ~15 W Argon ion laser (Spectral physics 2080) operated at mutli-line configuration to give the NIR output with a spectral purity at

Fig. 1   Schematic diagram of laser spectrometer. The main beam is sent to survey

system.   The calibration channels uses about 10% of the laser output power.
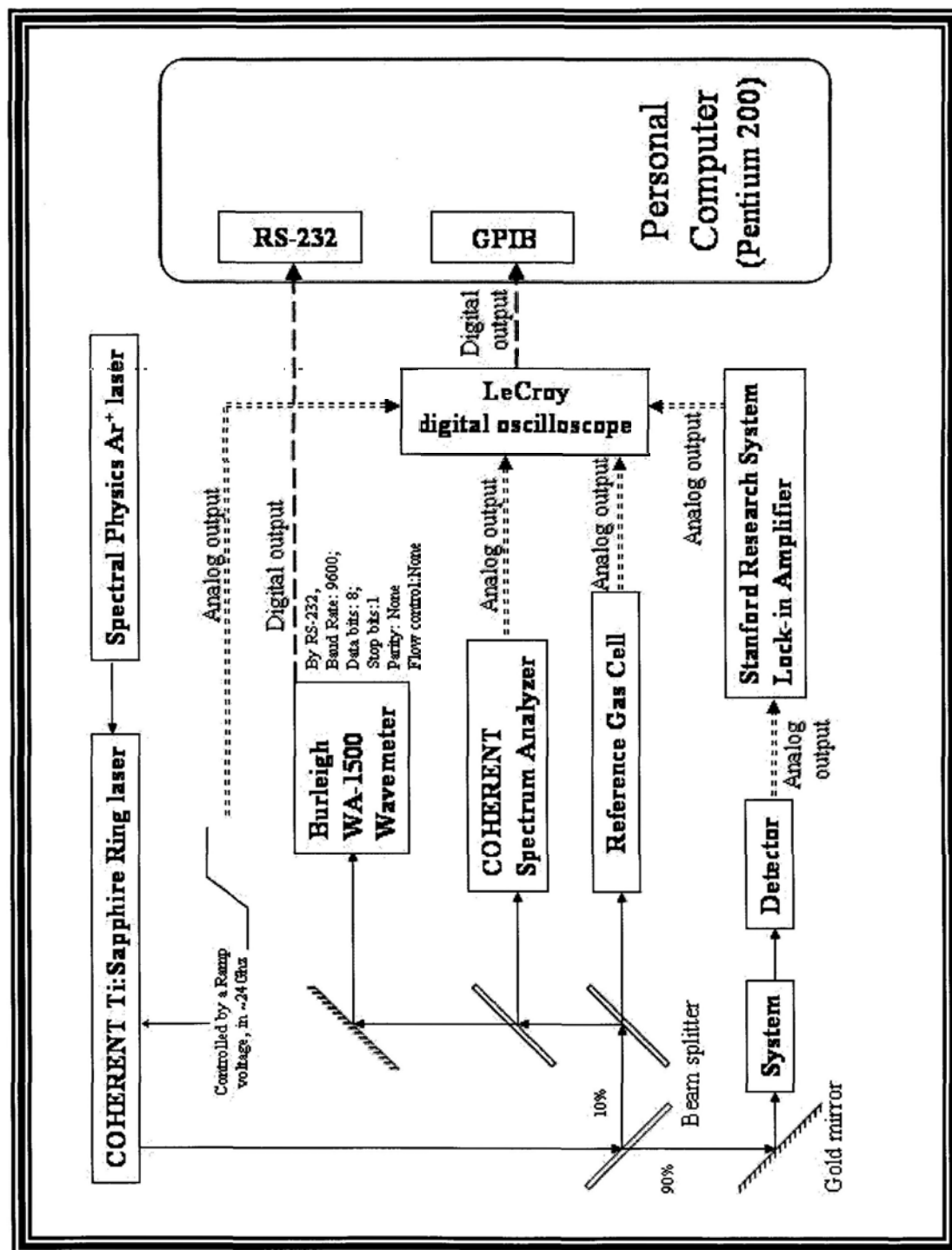
about 500 kHz root-mean-square frequency jittering. The typical NIR output is about 1.5 W. The monochromatic NIR output frequency can be continuously swept by applying a dc ramp voltage (V_r) from –5 V to +5 V to electrically tune the etalon assembly in the laser cavity. This scanning mechanism allows a continuous frequency change for a range of 0.8 cm^{-1} (24 GHz) without mode hopping. The starting frequency of each scan can be adjusted by applying an offset voltage to the etalon assembly to choose from one of the etalon modes, which are separated by about 0.3 cm^{-1}. Repeating these two procedures, one can continuously change the laser output with about 0.2 cm^{-1} overlap in frequency for each scan. By changing the Ti:sapphire ring laser cavity mirrors, the complete coverage of the Ti:sapphire laser may reach from 10000 to 14500 cm^{-1}. The detailed description of the laser source can be found elsewhere.[17]

To improve the efficiency of the spectroscopic measurements, an in-house computerized data acquisition/frequency calibration program has been set up. The use of computer routines provides much better reproducibility with little error due to human bias. With the speed of modern personal computer, the calibration and the processing of data can be done in seconds. In addition, the data obtained can be stored in the computer for further manipulation and analysis. In our data acquisition (DAQ) program, five channels of data from the ramp voltage (V_r), the

wavelength meter (W), the spectrum analyzer (SA), the survey species (S) and the

reference gas (R) are collected respectively as shown in Fig. 1.

While the NIR output is highly monochromatic, its absolute frequency is not

exactly known until a calibration procedure is carried out. The calibration channels,

including W, SA, R and V_r as shown in Fig. 1, use about 10% of the laser output

power. In practice, two approaches have been used in frequency calibration. In

the first approach, a wavelength meter (wavemeter WA-1500, Burleigh

Instrumentation) based on the principle of Michelson interferometry[18] with a

resolution of 0.001 cm^{-1} has been used in measuring the absolute frequency of light.

This approach allows the rapid determination of the frequency of the NIR radiation

without using any reference transition. Since the frequency reading of the

wavemeter is subjected to systematic and random errors, we have set up least-squares

fitting routine between the wavemeter reading and the ramp voltage to calculate the

absolute frequency during each scan. In the second approach, the laser output

frequency has been calibrated against some known spectra with well-documented

transition frequencies (*e.g.* I_2 in the NIR region).[19] Artificial frequency markers

produced by spectrum analyzer have been added to improve the accuracy of

measurements. The spectrum analyzer is based on a Fabry–Perot type confocal

interferometer[20] in which an optical cavity is formed by two concave mirrors with

high reflectivity as shown in Fig. 2. The separation between the two mirrors is the same as their radii of curvature. Light trapped into the cavity will produce interference pattern as shown in Fig. 3. The linewidth (full-width-at-half-maximum, FWHM) of the constructive interference[18] is related to reflectivity of the mirrors (Fig. 4) by

$$\delta v_{\frac{1}{2}} = \frac{c}{2\pi L \cos\theta} \left(\frac{1 - R}{\sqrt{R}} \right) \quad ,$$

where c is the speed of light, R is the reflectance, L is the distance between the two mirrors and θ is the angle of the incident light at the normal of the mirror.

The free spectral range[18] (the separation of intensity maxima in the TEM_{00} mode) shown in Fig. 3 and 4 is a function of the mirror separation

$$\Delta v_{FSR} = \frac{c}{4L} \quad ,$$

where c is the speed of light and L the distance between the two mirrors.

The spectrum analyzer used in our spectrometer was 25 cm in length with an FSR of 300 MHz. The constructive interference signals of the SA have been used as our frequency marker to obtain a "ruler" with 0.01 cm^{-1} scale. Since the length of the SA varies with changing temperature as a result of thermal expansion/contraction, the FSR will change accordingly. A vacuum housing has been built for the SA to maintain a thermally stable environment of operation. As

Fig. 2   Schematic view of spectrum analyzer.   The spectrum analyzer is made of a pair of high reflectivity concave mirrors, which is separated at a distance equal to the radii of curvature of the mirrors.
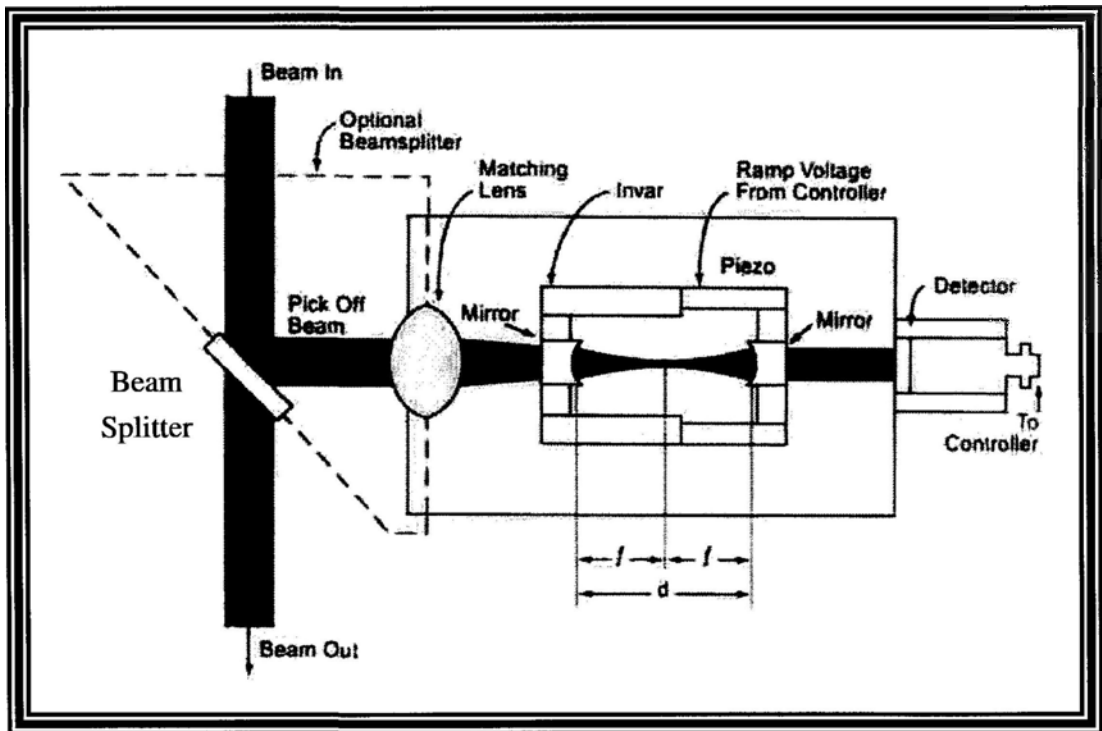
Fig. 3   The signals of the spectrum analyzer.   The range between two intensity
maxima is called free spectral range (FSR).
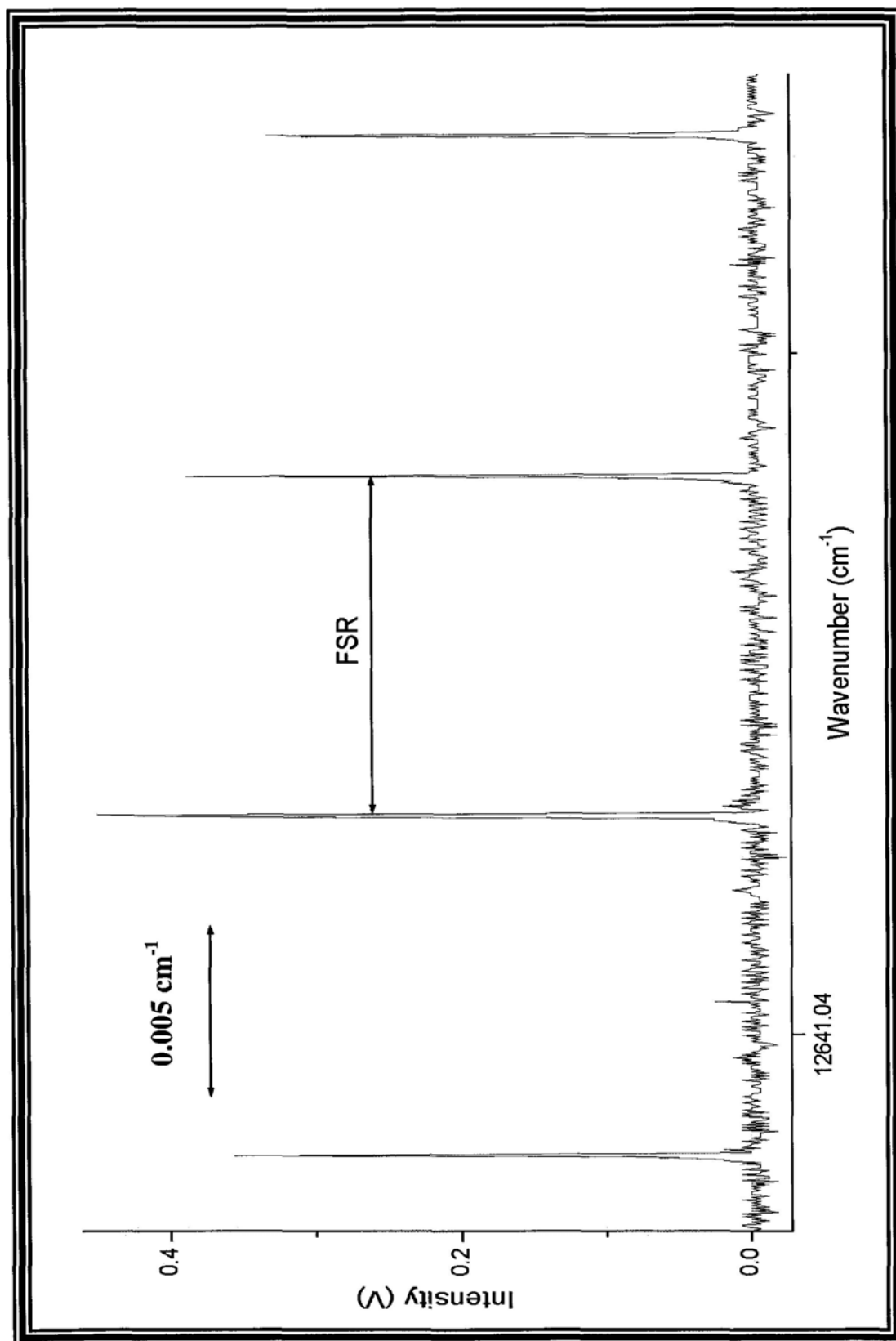
Fig. 4   The effect of mirror reflectivity on the spectral linewidth (FWHM) of SA. When the reflectivity of the pair of concave mirrors increases, the linewidth of the spectrum analyzer decrease.   The definitions of FSR and FWHM are also shown.
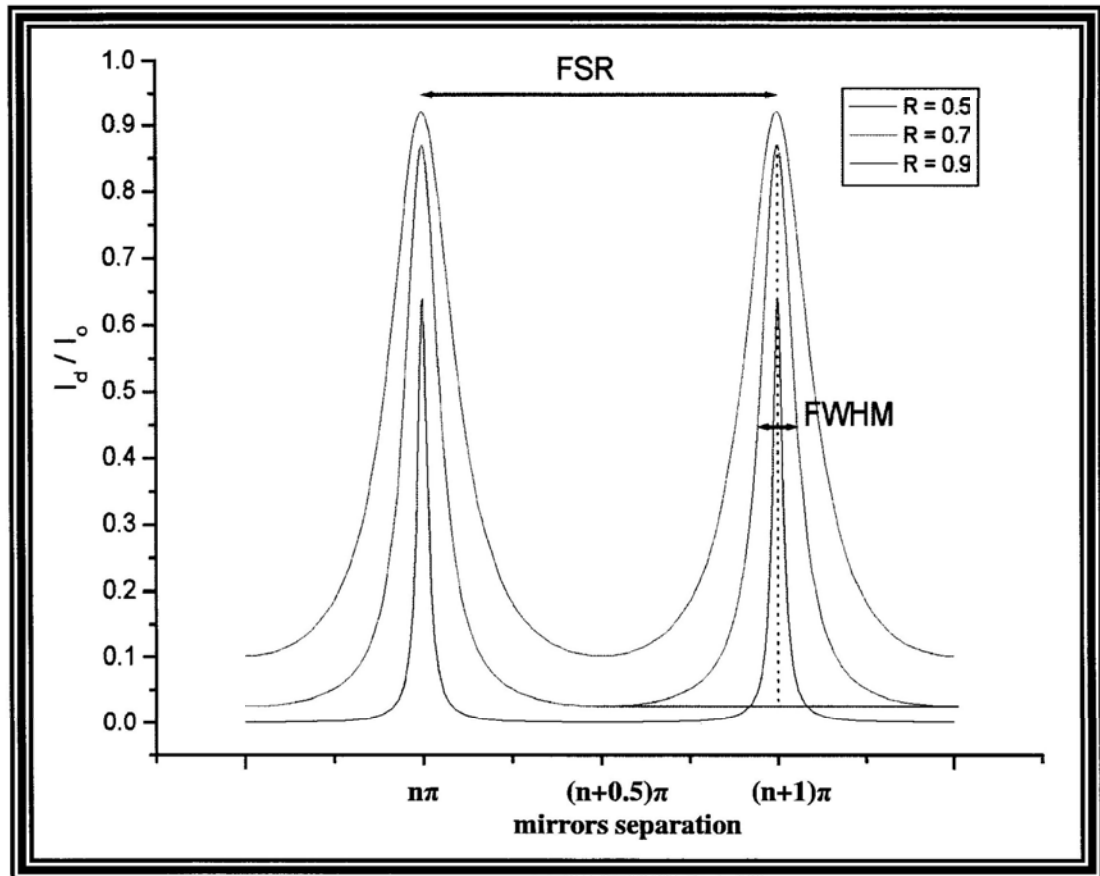
shown later, this arrangement produces satisfactory results.

The absolute frequency of the survey absorption can be determined by its frequency shift from the reference absorption calculated from the FSR of the SA multiplied by the number of frequency markers sandwiched by the two absorptions being considered. Since the separation of frequency markers only depends on the mirror separation regardless of the laser output frequency, the major error in counting the number of FSR arises from determining the non-integral values at both ends. We found an uncertainty of about 2% of an FSR obtained in repeated measurements. This corresponds to about 0.0002 cm^{-1} of error. This approach will provide accurate measurements provided that the FSR of the SA is accurately known. Nevertheless, if the FSR is not known accurately, the error will be enlarged due to the accumulation effect. In practice, the measurement of spectra can be done simply by plotting the spectra of reference gas, spectrum analyzer and survey species on a paper using a two-channel chart recorder. The frequency of absorption peaks can then be measured using a ruler, a pencil and a calculator. Two reference gases, I_2 and H_2O, whose transition frequencies are well documented,[19 and 21] have been used for frequency calibration. A typical pressure of 10-100 Torr has been used for reference gas cells of 80 cm long. I_2 and H_2O cells are made. These reference gases can also be used to examine the performance of the wavemeter as discussed below.

The analog output signal of V_r, SA, R and S have been collected by a four-channel synchronous 8-bits digital oscilloscope (LeCroy Waverunner LT344L) with a GPIB interface. The digital oscilloscope has collected the analog data and converted them into digital data at certain sampling rate (100 samples per second). In the digitization process, the most important concern is to maintain the data integrity after the digitization. As shown in Figure 5, the signal will be distorted significantly if the sampling rate is too slow. On the other hand, much resource of computer will be occupied if the sampling rate is too fast. The minimum sampling rate/frequency[22] can be determined by

$$Sample\ frequency = 2 \times Nyquist\ frequency,$$

where Nyquist frequency is the maximum frequency with aliasing, and the Nyquist frequency must be higher than the sampling frequency. Since the frequency marker from the spectrum analyzer has exhibited a width of 0.025 MHz full-width-at-half-maximum (FWHM), we have used a sampling rate of 100 Hz for a scanning range of 24 GHz at a scanning speed of 0.002 cm^{-1}/s. At this sampling rate, about 10 data points have been obtained for each marker to maintain their shape after digitization (Fig. 6). The processed and digitized data were then transferred to a personal computer, pc (a Pentium 200 MHz machine with 64 MB EDO RAM and 2 GB hard disk storage running on Windows 2000 operating system) through the GPIB

15

Fig. 5   Aliasing effects of an improper sampling rate.   The dotted trace is the true analog sinusoidal signal, while the solid line is the digitized signal.   The digitalized is totally distorted to a linear signal in (a); for (b), the frequency of the digitalized sinusoidal signal is different to the analog one; for (c), the minimum sample rate to present the digitized signal without any analog signal distortion; for (d), the optimum sample rate is achieved, when it has enough data to present the wave form of the analog one.

(a) 1 sample/1 cycle

(b) 7 samples/4 cycles

(c) 8 samples/4 cycles

(d) 40 samples/4 cycles
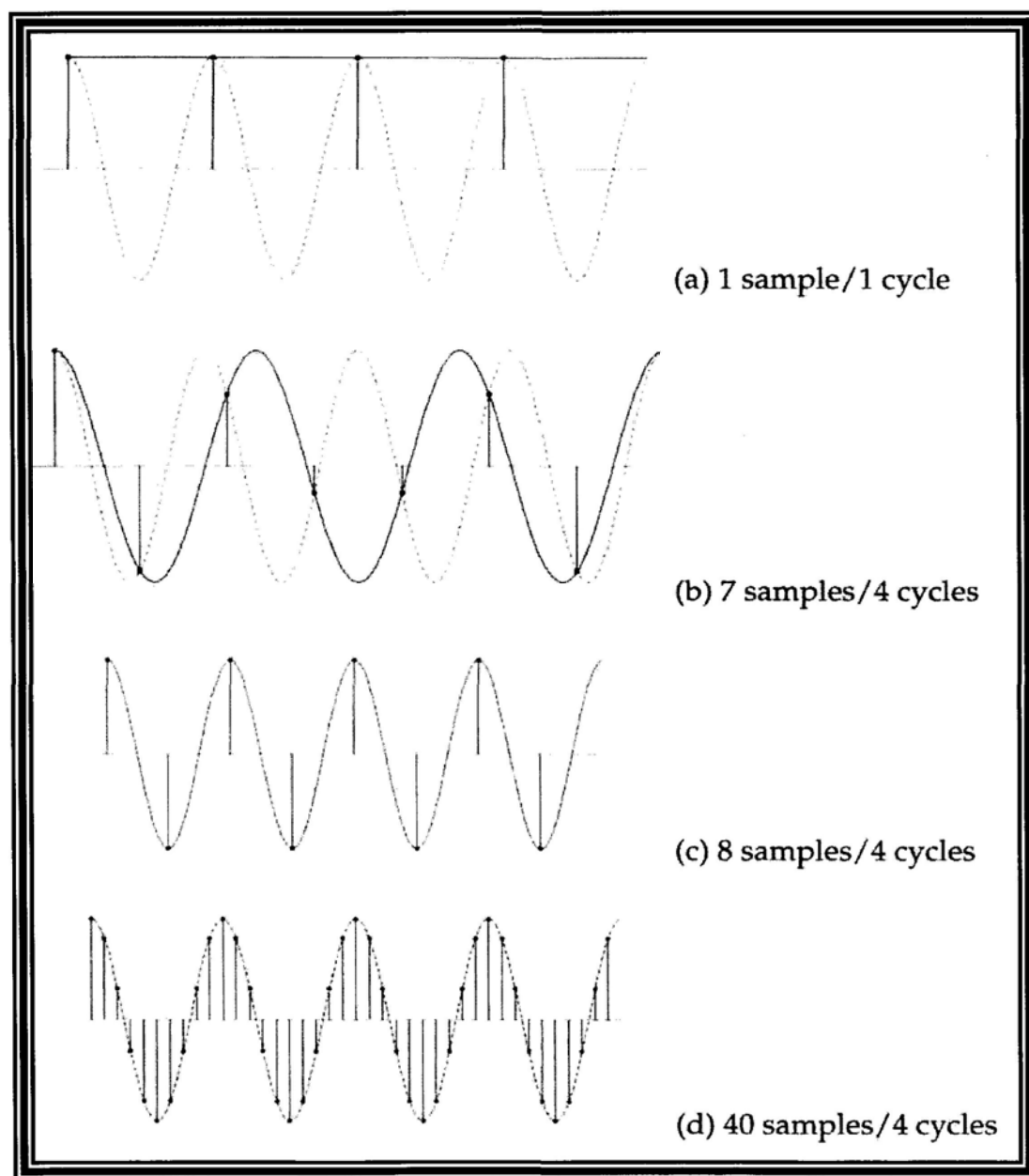
Fig. 6   The shape of the signal of SA with proper sampling rate.   For each peak,

it contains about ten data points to prevent aliasing the signal pattern.
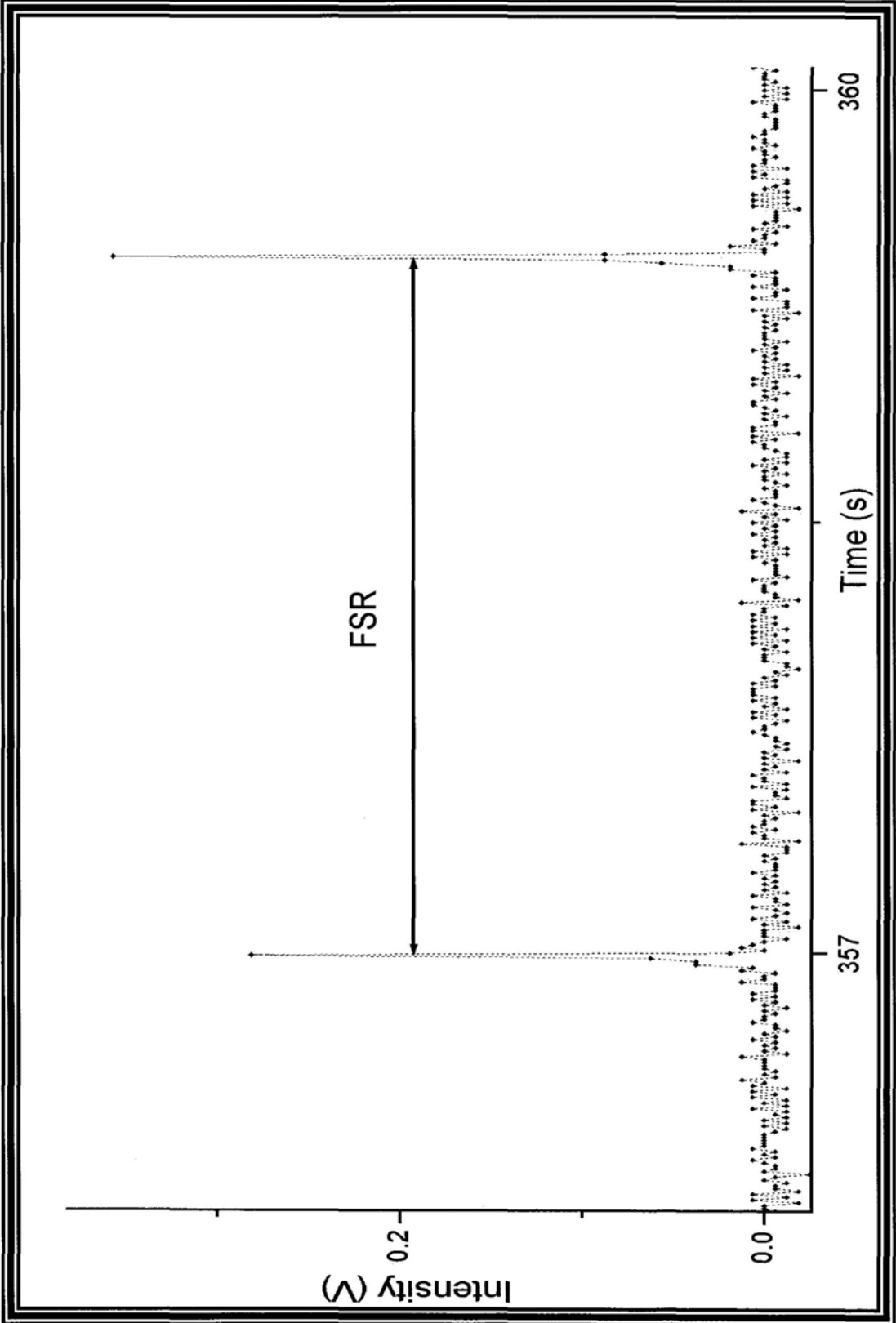
interface for further processing. On the other hand, the acquisition of the digital

frequency readout from the wavemeter was sent to the pc via the RS-232 interface at

a rate of ~1 Hz, which was much slower than the sampling rate of 100 Hz for the

digital oscilloscope. Therefore, there were two digital data with different sampling

rates through different interfaces. It is essential to have a common reference time

for data from both GPIB and RS-232 interfaces for frequency calibration. The pc

clock was used to measure the common time for both interfaces.

After the collection of digital data of various channels from different interfaces,

a correlation between time and laser output frequency within a scan should be

established. This was done by plotting the data from the wavemeter against time as

shown in Fig. 7. The correlation was then obtained by least-squares fitting to a

third power polynomial. As shown in Fig. 7, the smooth varying curve usually

gives an excellent correlation coefficient, $r^2 > 0.9999$. Using the fitted polynomial

equation, the frequency output at the time of collecting data from V_r, SA, R and S

has been calculated. Fig. 8 shows the same SA signal obtained using this approach.

It is seen that there is no distortion of the spectrum after converting the x coordinates

form time to wavenumber. In using reference absorptions for frequency calibration,

a correlation between the frequency marker from SA and time has been established.

By comparing the time of the reference absorption and with the documented

Fig. 7   A typical plot of wavenumber versus time showing the correlation and

smoothness.

$y = -7.3369066E-10x^3 + 2.7995797E-07x^2 + 2.361646E-03x + 1.2728396E+04$

$R^2 = 0.99986155$

Wavenumber (cm^{-1})

time (s)

[7]) The frequency of the laser radiation versus time

19
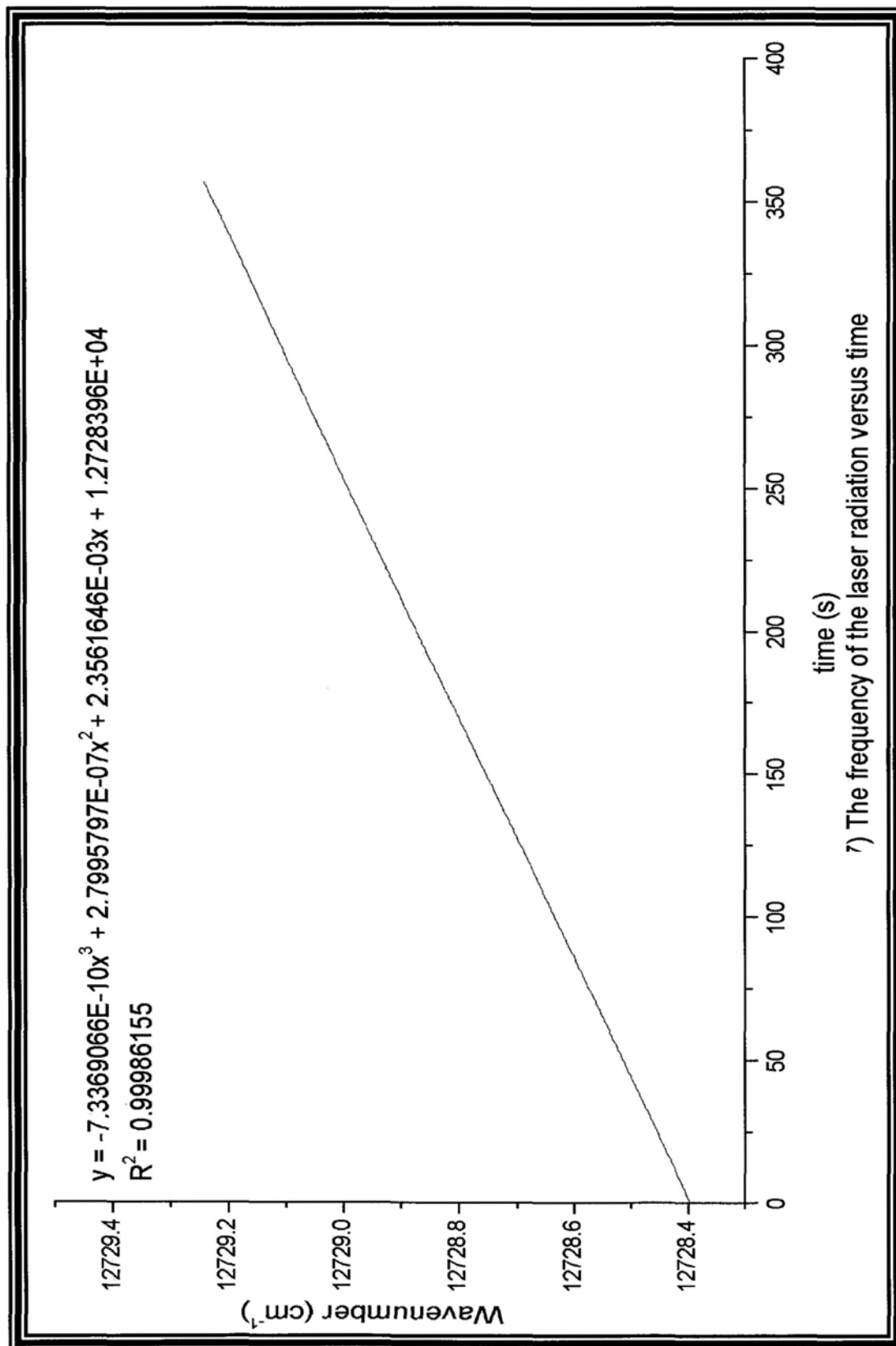
Fig. 8a   SA spectrum obtained in time.   Fig. 8b   SA   spectrum   obtained   in wavenumber.   It is shown that there is no signal distortion due to extrapolation of the data.
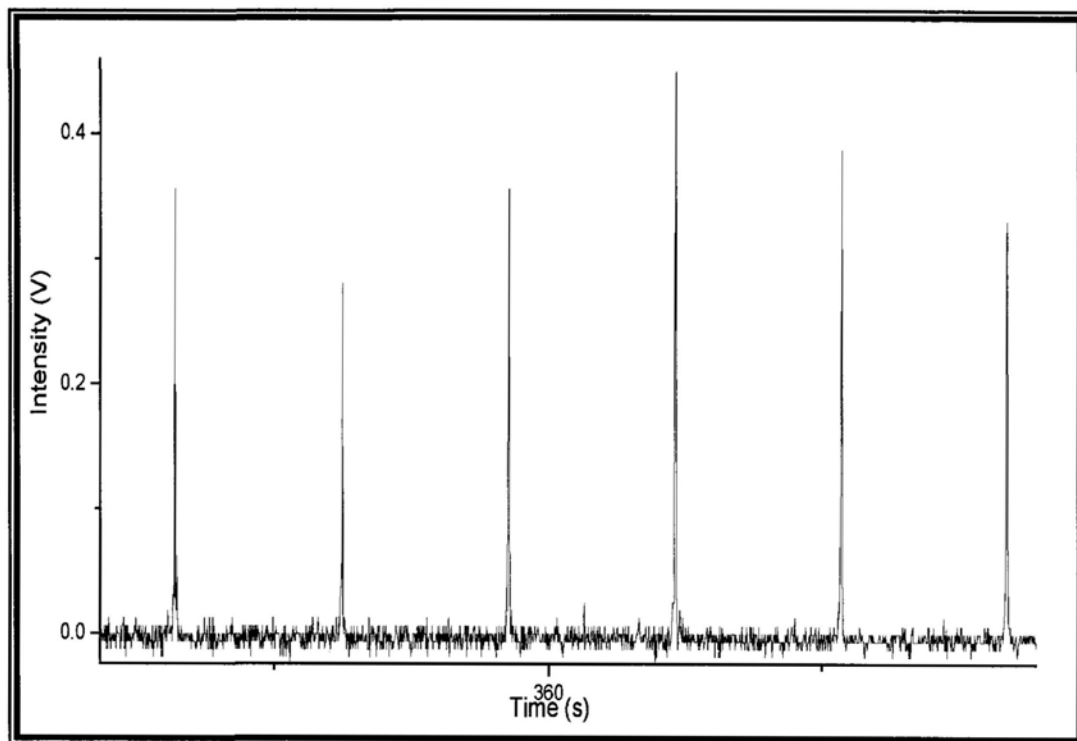
Fig. 8a SA spectrum obtained in time
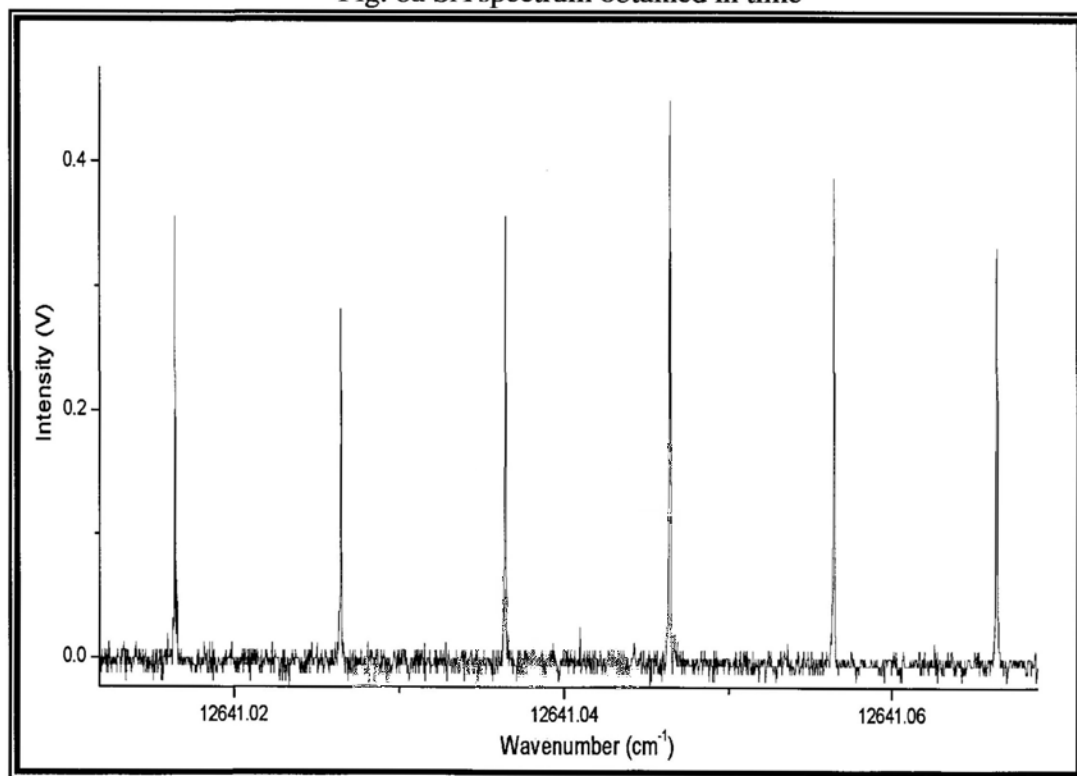
Fig. 8b SA spectrum obtained in wavenumber

frequency, the frequency shift of each frequency marker from the reference transition was then calculated. The frequency of the survey spectrum can then be calibrated based on the marker frequencies. Using both approaches, we can obtain a frequency reading with an accuracy of ≤ 0.001 cm^{-1} as shown as later.

An in-house program with graphical user interface (GUI) written in the LabVIEW® programming language (G language) from National Instruments Corporation is written for this special purpose. LabVIEW®, which is an interactive language using graphical symbols rather than textual language to describe programming actions, is widely used for instrument control and data acquisition in industry as well as academia. In LabVIEW® programming, objects such as controls, displays, indicators, functions, icons and connecting wire are used to set up a flow chart of algorithms. Each of these objects represents a subroutine written in C-language. By properly combining these controls, indicators, functions and icons with connecting wire, a variety of software programs called virtual instruments (vi) can be set up for instrument control, data acquisition, calibration, data analysis and manipulation.

During the experiment, the acquisition of the digital frequency readout from the wavemeter was sent to the pc via the RS-232 interface at a rate of ~1 Hz, which was much slower than the required sampling rate of 100 Hz for the digital oscilloscope.

To solve this difficulty, we had set up two independent routines in our in-house program to acquire data at different sampling rates from the RS-232 interface and GPIB interface, respectively. All digital data were referenced to the same pc clock after the initiation of the program. Fig. 9 shows the block diagram for the program logics. The complete DAQ program diagram written in LabVIEW® objects is shown in Fig. 10, and the GUI surface is shown in Fig. 11.

The accuracy of the frequency calibration program has been tested in the following ways. The absolute frequency measurement using the wavemeter examined by comparing the measured transition frequencies of H_2O to those found in HITRAN 96 database.[21] TABLE 1 shows the results of the tests. The values obtained from our program based on the wavemeter reading are consistently higher than the literature values. An average shift of $+0.0002$ cm^{-1} can be obtained by averaging the shifts for all the measured transitions. After correcting for this systematic error of the wavemeter, the measurements from our program gave an accuracy on the order of 0.0006 cm^{-1}, which is obtained from the standard deviation derived from the repeated measurements. This accuracy approaches the limit of the resolution (0.001 cm^{-1}) specified by the wavemeter.

In testing the accuracy using reference absorptions together with the SA markers, the accurate value of the FSR of the SA is needed. While the factory-specified FSR

Fig. 9   Schematic diagram for the DAQ setup using time as common parameter.
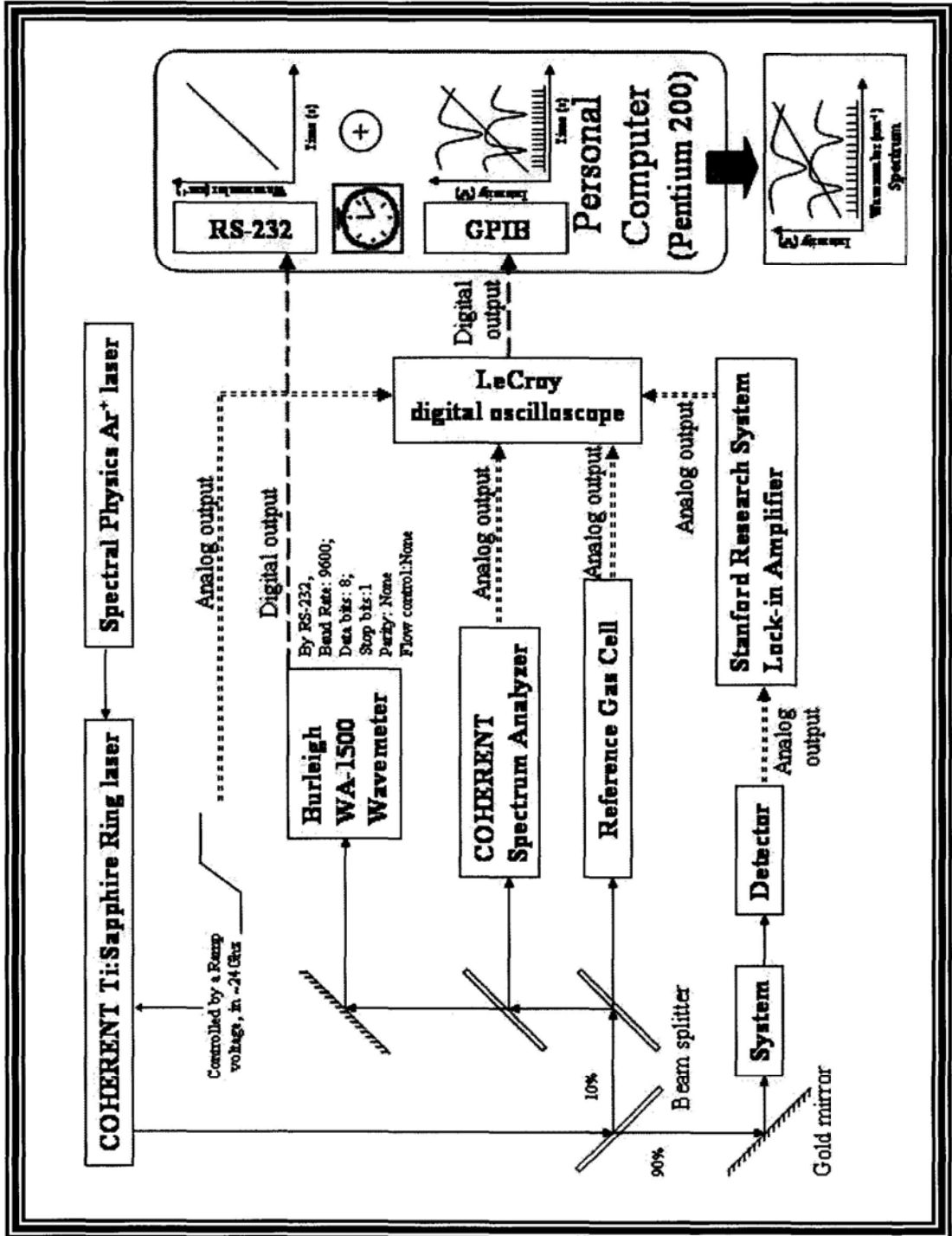
Fig. 10　The DAQ program written in LabVIEW® showing icons are connected by wires to set up a flow chart of algorithms.
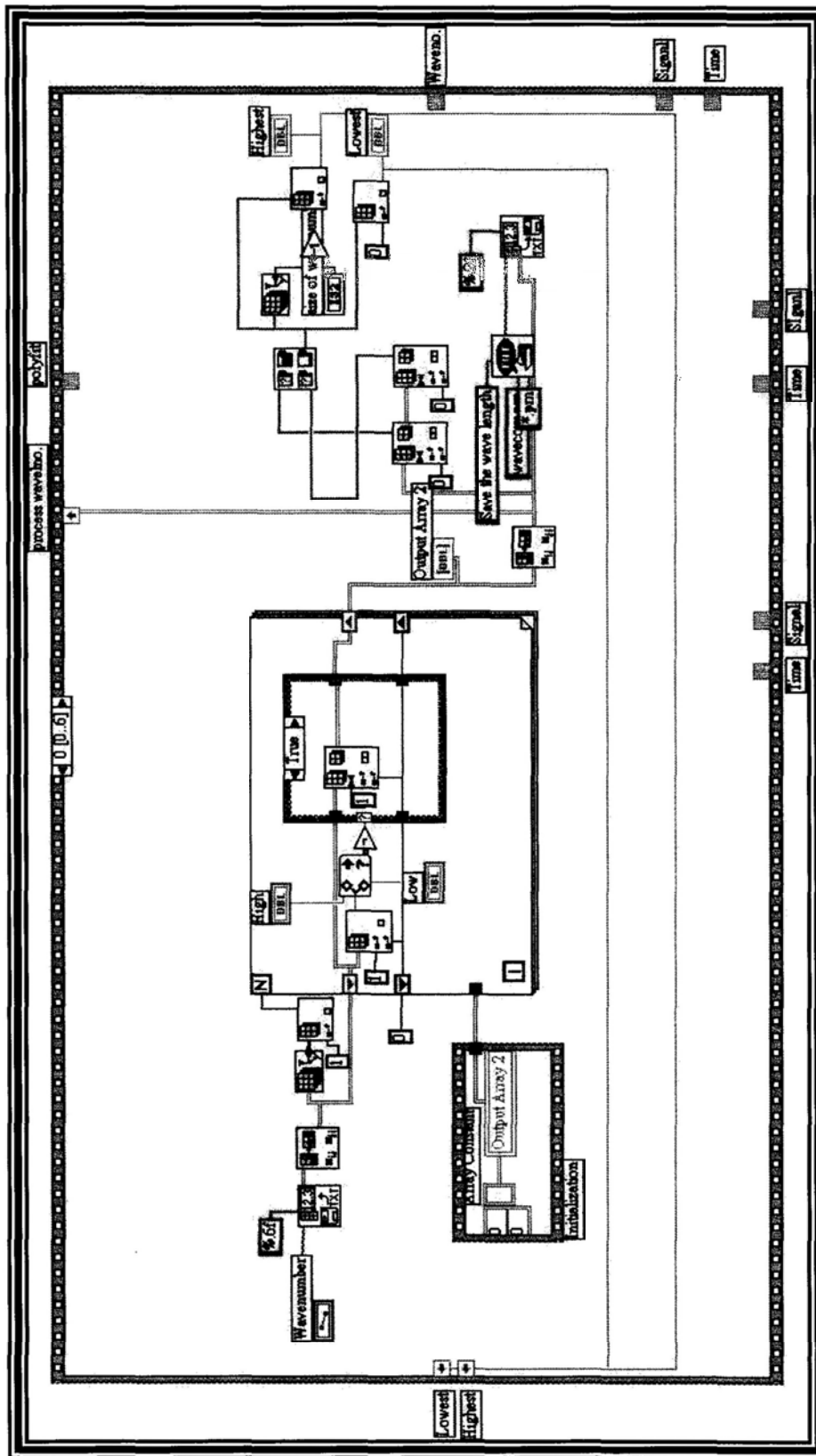
Fig. 11 The GUI surface of the DAQ program written in LabVIEW® after compilation.
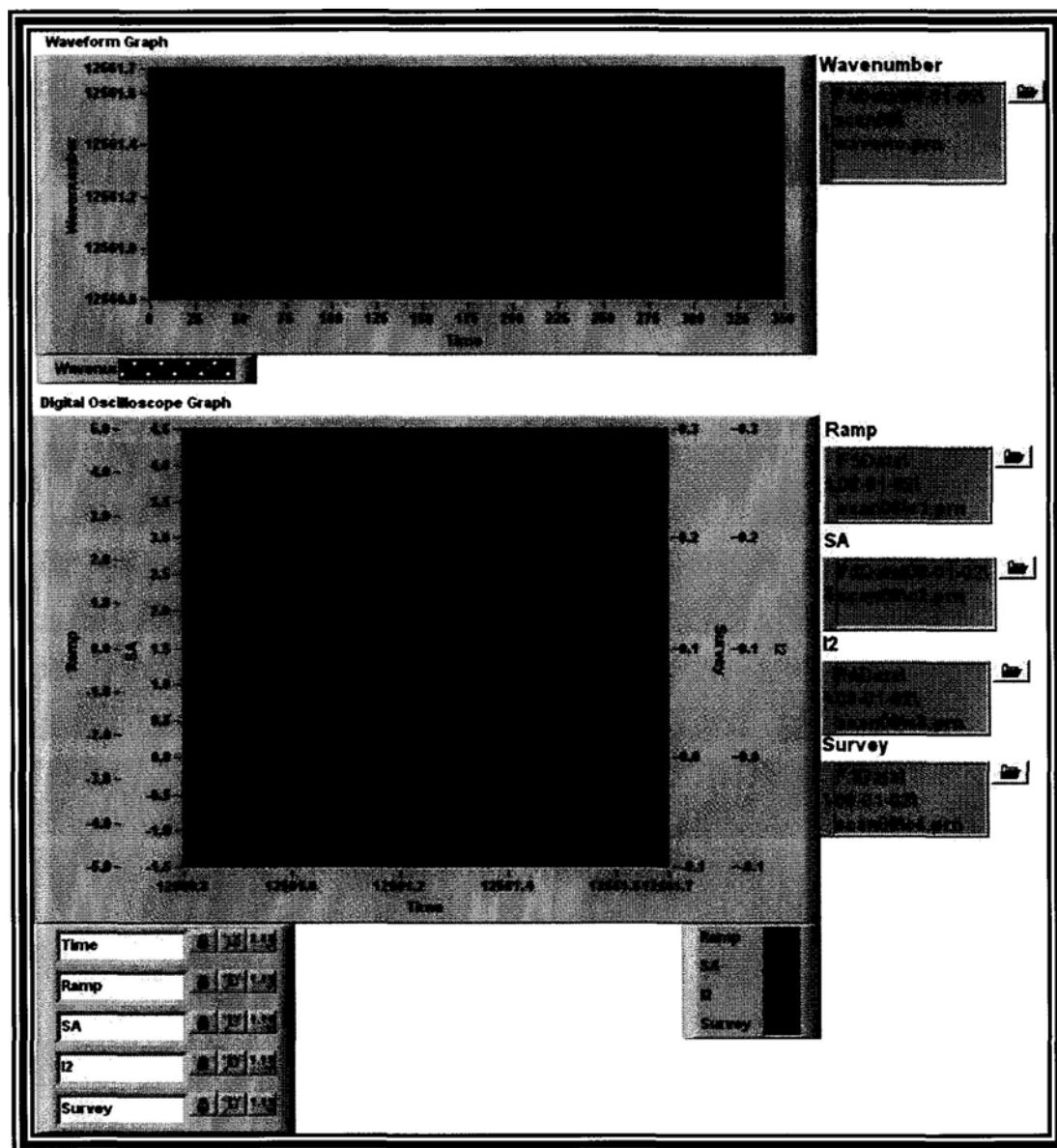
TABLE 1   Frequency calibration of wavenumber measurements using transition frequencies of H_2O.

Literature value[21] (cm^{-1})	Measured value (cm^{-1})	Measured value - Literature value[21] (cm^{-1})
12661.1102	12661.1100	+0.0008
12661.9495	12661.9485	-0.0010
12665.1595	12665.1597	+0.0002
12667.7522	12667.7525	+0.0003
12671.8620	12671.8619	-0.0001
12675.4320	12675.4327	+0.0007
12678.8100	12678.8097	-0.0003
12685.7690	12685.7699	+0.0009
12692.4101	12692.4106	+0.0005

The average of measured value - literature value[21] of Peak B is +0.0002 cm^{-1}.

The standard deviation of measured value - literature value[21] of Peak B is 0.0006cm^{-1}.

(An average shift of +0.0002 cm^{-1} from the literature value was obtained.)

of our SA is 300 MHz, more tests are needed to accurately determine its value. By more than 120 repeated measurements of the FSR based on the separation of pairs of I_2 absorptions[19] in different frequency regions, an average value of 0.00999394 cm^{-1} (299.611 MHz) was obtained. Using this value, we measured the frequencies for 5 other pairs of I_2 transitions[19] to examine its accuracy. The results of these measurements are shown in TABLE 2. It is seen that the accuracy obtained from this approach is $\leq$0.0010 cm^{-1}. Although both approaches of frequency calibration give about the same accuracy, the use of reference gas only works when at least one transition frequency (from either reference gas or survey species) in the spectrum is known. In case there is no documented transition frequency, the use of the wavenumber becomes the only choice.

2C. *AC* hollow cathode gaseous discharge station

Since the molecular ions and radicals are readily react with collision partners, their lifetime is very short, only on the order of $\leq 10^{-6}$ s. While matrix isolation[23] (shown in Fig. 12) pioneered by G. C. Pimentel[24] and M. E. Jacox[25] has been widely used for spectroscopic studies of reactive species, it also has many limitations. For instance, the observed transition frequencies in matrix often shift from the corresponding gas phase values due to stronger intermolecular interactions in the

TABLE 2   Frequency calibration using reference absorptions of I_2 and frequency markers.   Each pairs of the transitions were measured repeatedly for 30 times.   The values shown in the table are averages of 30 measurements.

Peak A (Literature value[19]), cm^{-1}	Peak B (Measured value), cm^{-1}	Peak B (Literature value[19]), cm^{-1}	Peak B (Measured value - Literature value[19]), cm^{-1}
12375.2147	12375.4420	12375.4414	+0.0006
12560.9690	12561.4910	12561.4884	+0.0026
12640.7628	12640.9251	12640.9257	-0.0006
12802.0302	12802.1400	12802.1413	-0.0013
12802.0302	12802.2907	12802.2915	-0.0008

The average of measured value - literature value[19] of Peak B is 0.0001 cm^{-1}.

The uncertainty of measured value - literature value[19] of Peak B is ±0.0008 cm^{-1}.

(The high uncertainty of the measured values means the result has only accuracy ≲0.0010 cm^{-1}.)

Fig. 12   Diagram representing matrix isolation.   The reactive species are isolated

form each other in the rigid host matrix lattice preventing bimolecular reaction.
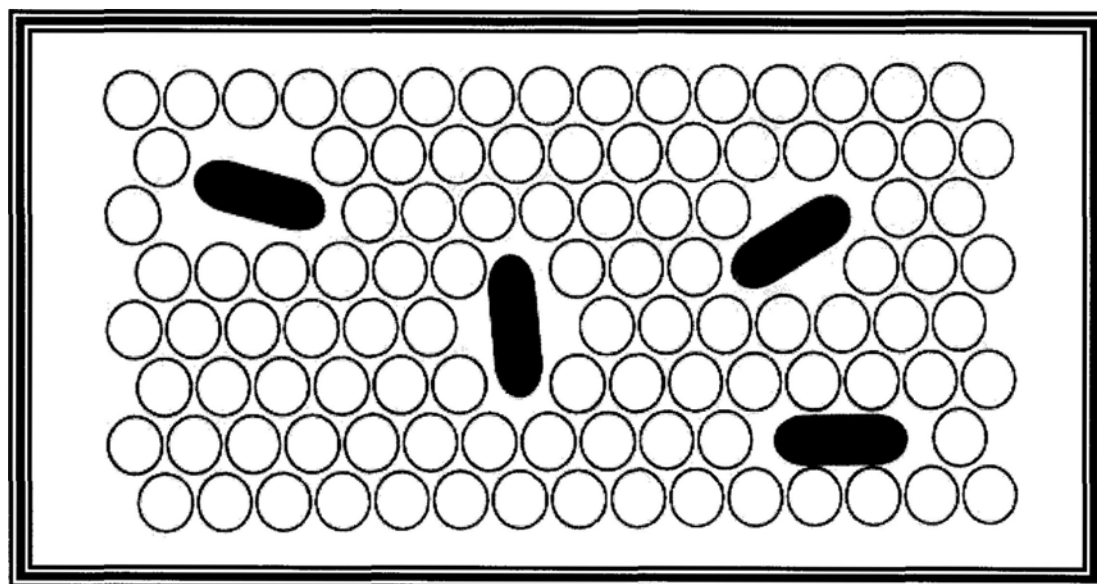
where

is represented as reactive species, and

is represented as matrix material.

solid environment. In addition, the absorption peaks obtained are usually very board due to serious inhomogeneous broadening resulting from different micro-environments for the embedded molecules and homogeneous broadening resulting from fast relaxation and dephasing processes. With very few exceptions, the observed linewidth is typically around 1-10 cm^{-1} (Fig. 13), which makes it very difficult to study rotationally resolved spectra. By analysis only the vibrational frequencies; it is difficult in identifying larger molecules, particularly in case of more than one reactive species.

An alternate approach is to study reactive species in the gas plasma generated by gas discharges. However, the efficiency of the production for the reactive species is very low ($\leq$1 ppm). Their detection therefore requires special technique to reduce the noise as much as possible. On the other hand, their short lifetime requires the detection should be completed before they react with surrounding molecules. In order to employ the phase sensitive detection of absorption signals to overcome the difficulties, an *ac* hollow cathode discharge system composed of a high current *ac* discharge power supply and a 2 m hollow cathode cell has been built. The details of the systems are described as below.

The *ac* power supply was assembled from a function generator, an audio power amplifier and a pair of audio transformers. High frequency sinusoidal waves (*e.g.*:

Fig. 13   One of the example[26] (FT-IR spectrum of a five-component mixture of 1,3-, 1,4-, 1,5-, 2,3- and 2,6-dimethylnaphthalene) using matrix isolation.   The resolution of this spectrum is 1 cm^{-1}.   The poor resolution of this spectrum is due to the limitation of matrix isolation method.
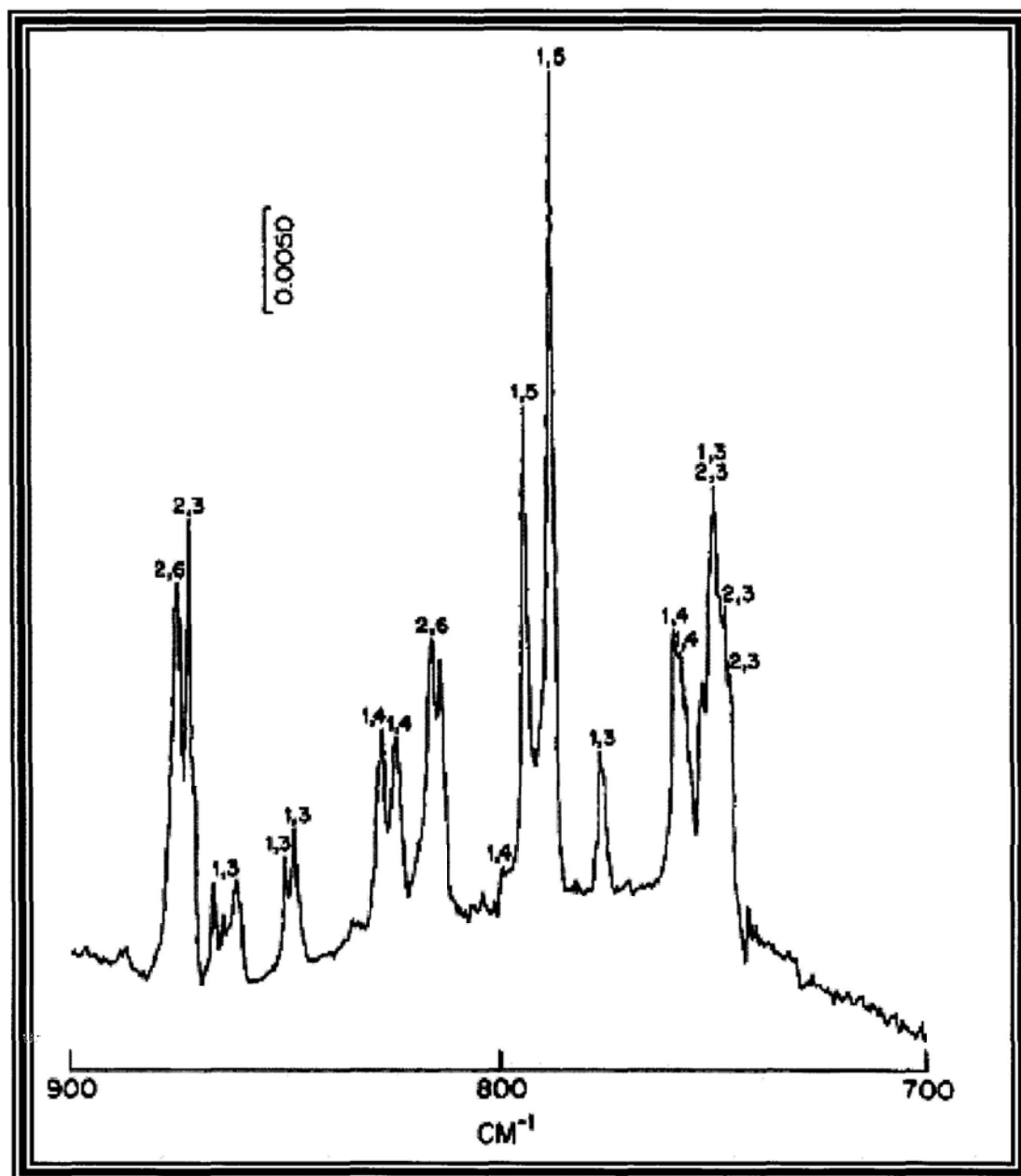
5 kHz) generated from the function generator were synchronously fed into both channels of the audio power amplifier (Crown MA-3600VZ). The amplified signals from each channel were then stepped up separately using a pair of high power audio transformers (100 W). This provided us with a pair of two high voltage channels (~2 kV) for carrying out the discharge process. The total peak-to-peak output current could reach about 2.5 A using this configuration. During our experiment, a milder discharge voltage (~1500 V) and current (1 A as shown in Fig. 14) has been applied so that the heat generated by the system was manageable.

The cathode of our home-built hollow cathode discharge cell was made of stainless steel tube of 2 m in length and 2 inch in inner diameter. The tube was cooled with ethanol equilibrated at 200 K to remove the heat generated during the discharge process. Each end of the cathode tube was connected to a Pyrex glass tube fitted with CaF_2 window at Brewster angle. Two side arms were then fitted on the glass tube for the gas inlet and anode, respectively, as shown in Fig. 15. At the center section of the hollow cathode tube, a pump port was installed to evacuate the gas mixture from the cell. In a normal run, the gas mixture was continuously flew into the cathode cell through the gas inlets and was being pumped out through the pumping port using a Roots pump station (Alcatel RSV 601 backed by Edwards E2M80) so that a constant flow of gas was maintained to give a steady state pressure

Fig. 14   The typical discharge current of our discharge system.   The discharge is

on and off periodically due to the periodically alternating discharge current.   Under

the normal working case, 1 A is applied on the system.
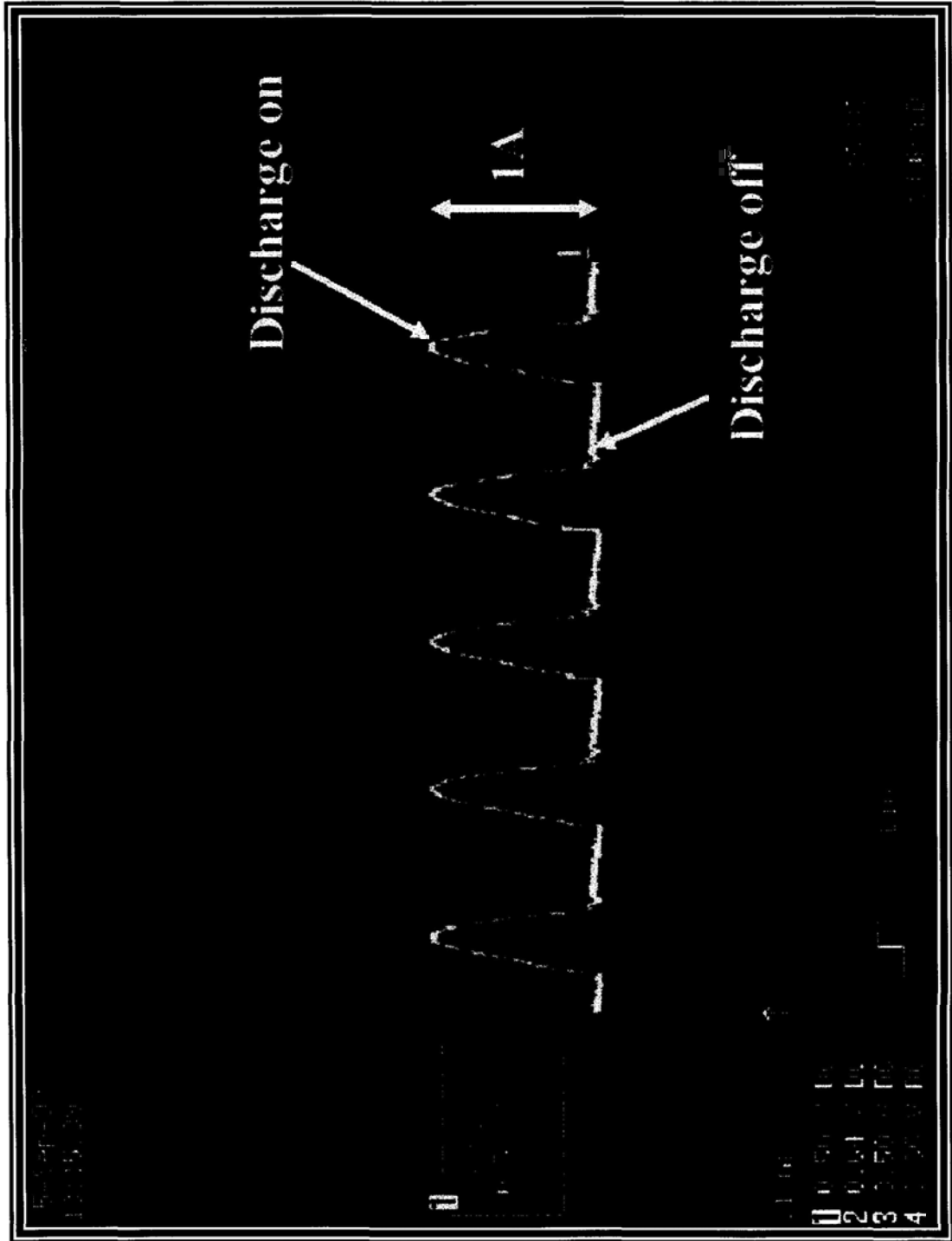
Fig. 15   Schematic diagram of the optical layout and the circuit diagram of the *ac*

hollow cathode discharge system.
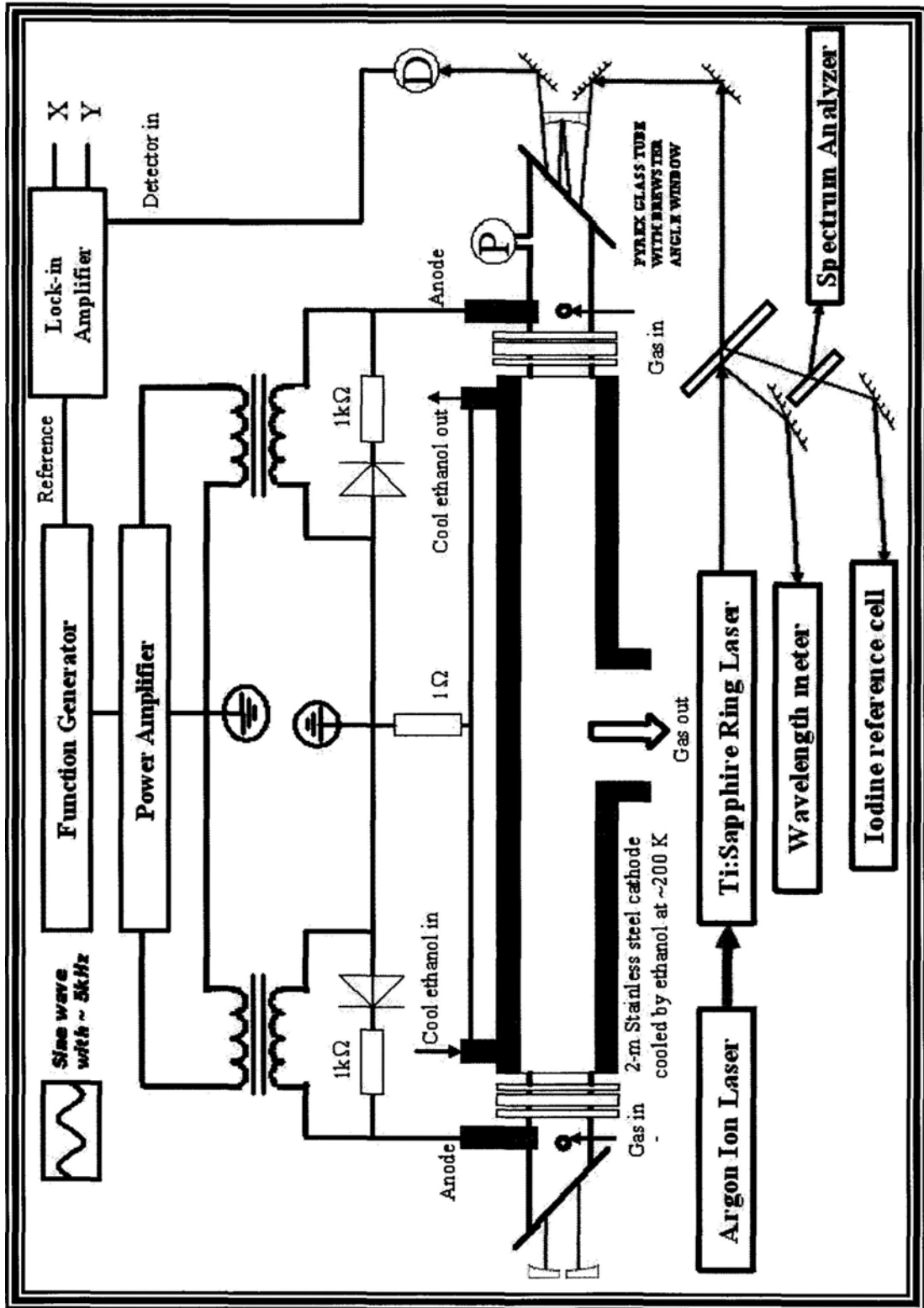
of about 1 Torr. The constant flow approach allows a steady state production of the short-lived ions and radicals. The high speed Roots pump ensures the supply of fresh parent gas for discharges.

In order to increase the optical path length, a set of multi–traversal concave mirrors with 2.5 m in radius of curvature was set up in White configuration[27] (Figs. 16a) to allow the NIR laser radiation to achieve 24 passes (by counting the number of image on the "field" mirror, as shown in Fig. 16b) with an effective optical path length of 48 m. Since the ions/radicals production in the gas discharges is very low, at the level of ppm, further enhancement of detection sensitivity is needed. The phase sensitive detection technique[28] based on concentration modulation has been employed to achieve zero-background absorption spectroscopy.

In applying concentration modulation, *ac*, instead of *dc*, high voltage is used to drive the gas discharges using the hollow cathode cell. Due to the nature of hollow cathode, discharges only occur in half of the high voltage *ac* cycle when the cathode tube is at lower voltage. Hence, the absorption signals of the species whose concentrations vary synchronously with the *ac* discharge cycle (*e.g.* ions, radicals as well as parent species) can be picked up by the phase sensitive detection referenced at the discharge frequency. As a result, all signals not synchronized with the reference frequency will be rejected to significantly reduce the noise from the laser

Fig. 16a Schematic diagram of the White configuration multi-pass setup.[27] Laser radiation is bounced back and forth by the White spherical concave mirrors.

Fig. 16b Location of images on the "field" mirror. The number in the boxes means the image due to nth reflection.
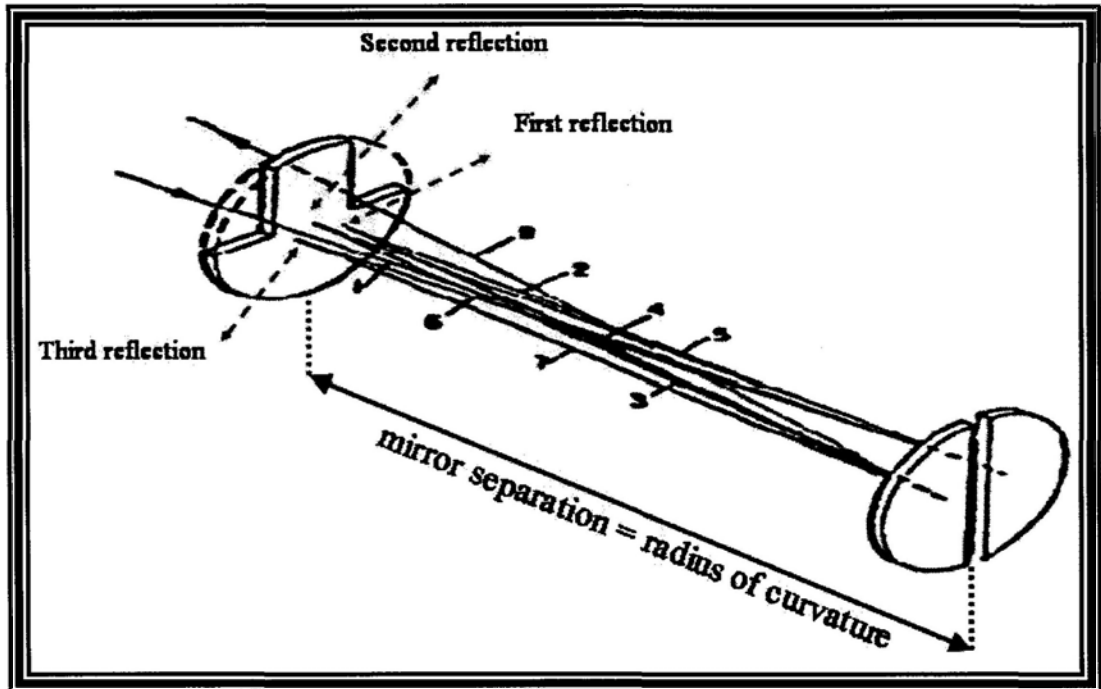
Fig. 16a Optical pathway using the White configuration.
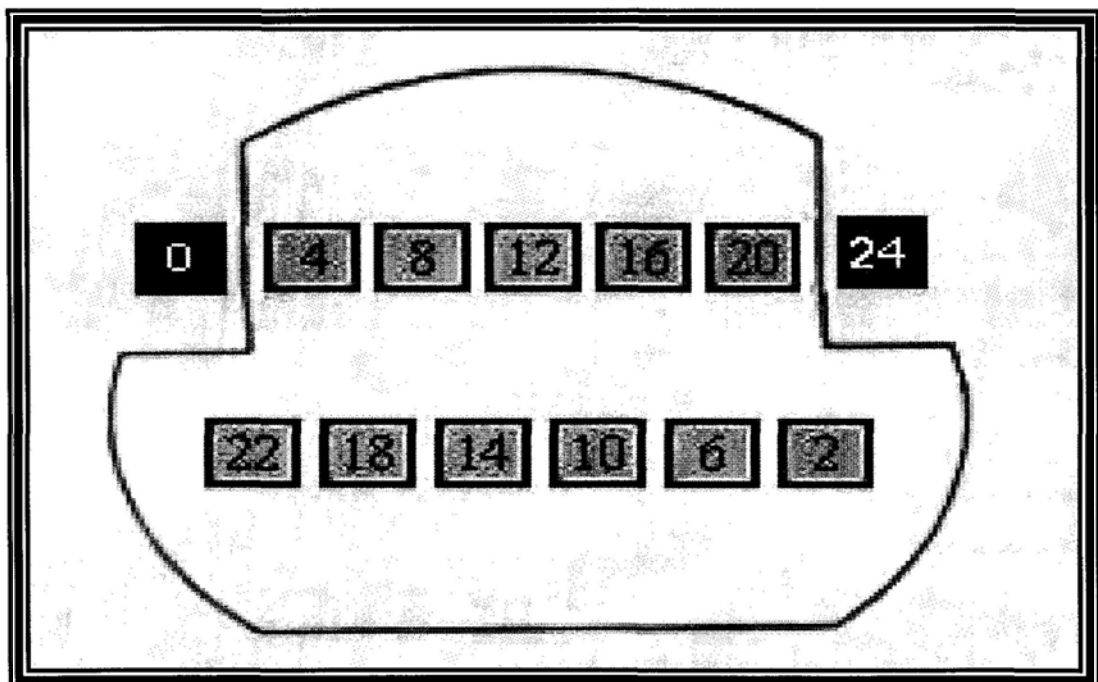
Fig. 16b Location of images on the "field" mirror

system or other source. In practice, the absorption signals were detected by a silicon PIN diode and then processed (demodulated) in a lock-in[29] amplifier (SRS SR830). The processed signals were then sent to the survey channel of the DAQ system for digitization and further analysis as mentioned above.

The typical discharge frequency is a few kHz depending on the nature of parent gas mixture, which is made of small amount of parent gas with large amount of buffer gas such as He, Ar or H_2. For instance, a gaseous mixture of CH_4/He in a ratio of 1:170 with a total pressure of ~860 mTorr was used in the study of the Phillips system of C_2.

The performance of the gas discharge system together with the spectrometer and the data acquisition system was examined using the weak transition of N_2^+.[30] As seen in Fig. 17, a sensitivity is found to be $\Delta I/I \sim 1.2 \times 10^{-6}$. Comparing to other similar setup, our sensitivity no doubt approaches the limit of simple concentration modulation.

2D. Summary

In summary, we have set up a high resolution near infrared laser spectrometer with the high power *ac* hollow cathode discharge station by using high sensitivity concentration modulation detection scheme. The routine for calibrating the

Fig. 17 Performance test of apparatus using N_2^+ absorptions. The detection limit ($\Delta I/I$) is at the ppm level ($\sim 1.2 \times 10^{-6}$).
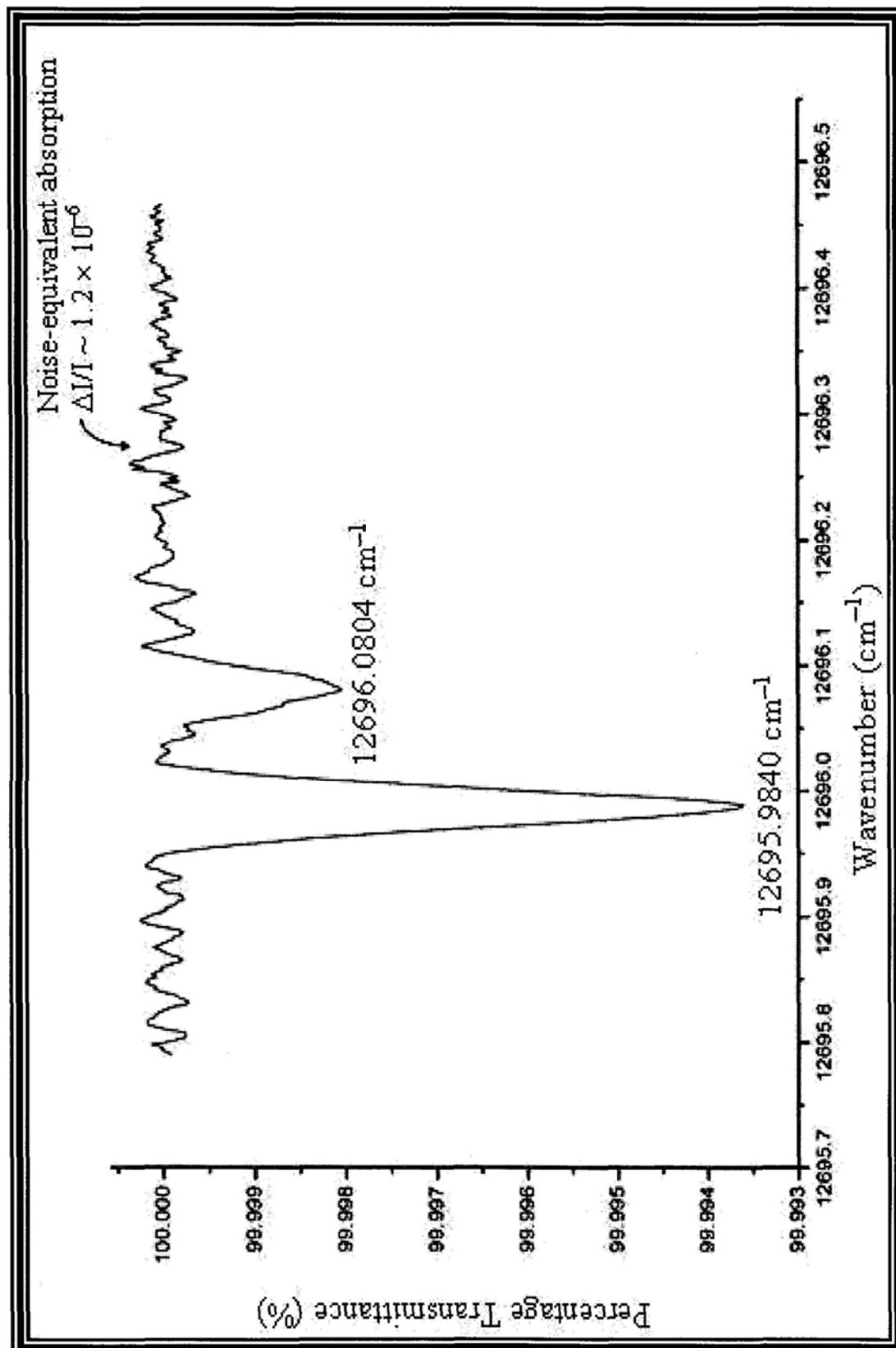
absolute frequency of the laser output gives an accuracy better than 0.0010 cm^{-1}.

The detection limit of our system is around 1.2 ppm using multi–traversal technique with zero-background concentration modulation scheme.

Chapter 3

The CH$_4$/He Plasma:

Absorption Spectrum Of

The Phillips System Of C$_2$ Radicals

3A. Introduction

Reactive species[13] composed solely of carbon and hydrogen atoms play important roles in various areas such as astrochemistry and organic chemistry. It is believed that the understanding of these species will lead to the understanding of the mystery of life. For instance, the carbon family[13] (Fig. 18) of the interstellar molecular species is a key to the formation of long carbon chains in astronomical objects. Over the years, extensive studies of these species have been carried out in aspects of structure, mechanistic and kinetic studies, astrophysics and astrochemistry. Carbon containing species are important molecules not only found in interstellar media but also found as intermediates and transition states of organic reactions as well as in combustion processes. Studies of these species no doubt provide some insight leading to a better understanding of the mechanisms of organic reactions and flame combustion.

Most carbon containing reactive species possess a number of low-lying

Fig. 18　The carbon family in the interstellar gas clouds.　C_2 is one of the member in the carbon family that is solely composed by carbon atoms.

electronic states.[12] Transitions between these states exhibit spectra in the visible and near infrared regions. *In situ* high resolution spectroscopic studies of these carbon containing species in gaseous plasma provide structural information at unprecedented accuracy as well as dynamic information on the formation mechanism.

In an attempt at searching for a quasi-linear species CH_2^+ [31] in CH_4/He plasma, we have observed the very weak $A^1\Pi_u$ - $X^1\Sigma_g^+$ absorption spectrum, also known as the Phillips system, of C_2 radicals. In the following, the details of this work will be discussed.

3B Quantum mechanics of C_2

The quantum mechanics of C_2 has been extensively studied. As a homonuclear diatomic molecule, it belongs to $D_{\infty h}$ molecular symmetry group with four permutation-inversion operations, namely E, (12), E* and (12)*.[32] The corresponding character table of $D_{\infty h}$ group shown in TABLE 3 has four irreducible representations, $s\Sigma_g^+$, $a\Sigma_u^+$, $a\Sigma_g^-$ and $s\Sigma_u^-$. The (s, a), (+, -) and (g, u) correspond to the symmetric and antisymmetric properties under the permutation (12), space inversion E* and permutation-inversion (12)*, respectively. Since the two ^{12}C are bosons with zero nuclear spin, $I = 0$, the total wavefunction (Ψ_t) of C_2 should be

TABLE 3   Character table of $D_{\infty h}$ group.

	E	(12)	E*	(12)*
$s\Sigma_g^+$	1	1	1	1
$a\Sigma_u^+$	1	-1	1	-1
$a\Sigma_g^-$	1	-1	-1	1
$s\Sigma_u^-$	1	1	-1	-1

invariant under (12) permutation to satisfy the Pauli principle,[33] *i.e.*

$$(12)\Psi_t = \Psi_t.$$

According to the character table of the $D_{\infty h}$ group, the total wavefunction of C_2 must belong to either $s\Sigma_g^+$ representation with positive parity or $s\Sigma_u^-$ representation with negative parity. Since the total wavefunction must be s symmetry, states with positive parity are always of g symmetry whereas states with negative parity of u symmetry.

Under the Born-Oppenheimer approximation,[34] the total wavefunction (Ψ_t) is expressed as

$$\Psi_t = \Psi_e \Psi_v \Psi_r \Psi_{ns}$$

where Ψ_e, Ψ_v, Ψ_r and Ψ_{ns} are electronic, vibrational, rotational and nuclear spin wavefunctions, respectively. In considering the symmetry properties of the total wavefunction, one can separately consider the symmetry property of each component wavefunction and then combine accordingly.

The nuclear spin wavefunction Ψ_{ns} of C_2 belongs to the $s\Sigma_g^+$ representation, which is invariant under all operations, as expected from zero spin nuclei. Similarly, the vibrational wavefunctions Ψ_v of diatomic molecule also belong to $s\Sigma_g^+$ as it is a function of internuclear separation. For the ground electronic state (X state) of C_2, the symmetry is obvious from its label of $^1\Sigma_g^+$, *i.e.* it is totally symmetric under all

44

symmetry operations in group. The symmetry property of rotational wavefunctions therefore determines the symmetry of the total wavefunction in the ground electronic state. It is known that diatomic rotational wavefunctions are spherical harmonics[35] specified by quantum numbers J and M.[2] It has been known that the rotational wavefunctions $|J,M\rangle$ transform according to the following[2]

$$E*|J,M\rangle = (-1)^J|J,M\rangle \text{ and}$$
$$(12)|J,M\rangle = (-1)^J|J,M\rangle.$$

Accordingly, the rotational wavefunctions should be $a\Sigma_g^-$ representation for levels with odd J values and $s\Sigma_g^+$ representation for levels with even J values. It is obvious that rotational levels with $a\Sigma_g^-$ symmetry (*i.e.* odd J levels) cannot satisfy the Pauli principle by combining with the totally symmetric Ψ_e, Ψ_v and Ψ_{ns}. Therefore, all the odd J rotational levels are forbidden in the $^1\Sigma_g^+$ state of C_2 and all the even J rotational levels are of equal nuclear spin weight.

In the excited electronic state ($A^1\Pi_u$), the non-zero electronic orbital angular momentum couples with the rotational angular momentum to give rise to the Λ-doubling, which complicates the symmetry considerations. As a result of the coupling, the lowest J is 1 instead of 0 in the $A^1\Pi_u$ state. Since Ψ_v and Ψ_{ns} has no dependence on the electronic coordinates, they will have the same $s\Sigma_g^+$ symmetry in the excited $A^1\Pi_u$ state as in the ground electronic state $X^1\Sigma_g^+$. The Λ-doubling, however, splits each rovibronic level into doublets with opposed parity,[2]

corresponding to the symmetric and antisymmetric linear combinations of states with

$+\Lambda$ and $-\Lambda$. In the presence of Λ-doubling, the rotational wavefunctions behave as

symmetric top molecules with Ω replacing K with $\Omega = \Lambda$ in the case of singlet states.

Since the electronic wavefunction in the $A^1\Pi_u$ state is u symmetry corresponding to a

phase factor of -1 under the (12)* operation, the allowed rovibronic levels must have

negative parity so that the product of $\Psi_e\Psi_v\Psi_r\Psi_{ns}$ will be symmetric under (12)

operation to satisfy the Pauli principle. It can be shown that only rovibronic

wavefunctions with symmetric combination in the odd J levels or antisymmetric

combination in the even J levels are allowed in the $A^1\Pi_u$ state.

The selection rules for Phillips system of C_2 follow the typical selection rules

for $^1\Pi_u \leftarrow {}^1\Sigma_g^+$ transitions. These rules are $s \leftrightarrow s$, $+ \leftrightarrow -$ and $g \leftrightarrow u$ together with the

rotational selection rule $\Delta J = 0, \pm 1$. Fig. 19 shows the schematic energy pattern of

the rovibronic levels together with the allowed transitions.

3C Spectroscopic studies of C_2 radicals: an overview

Being one of the simplest member of the carbon containing species,[13] C_2 is one

of fundamental importance in different disciplines. C_2 molecules have been found

in a variety of astronomical objects such as the Sun,[36] carbon stars,[37] comets[38] and

interstellar clouds.[39] Also, C_2 can be easily found and generated in the various

Fig. 19 Energy diagram of the Phillips band system of C_2. The levels forbidden by the Pauli principle are shown by dotted lines. The allowed transitions are shown by vertical arrows. The selection rules of this system are also listed as below.

* Selection rules for C_2 Phillips band system:

(1) $\Delta J = 0, \pm 1$, with restriction $J' = 0 \leftarrow J'' = 0$

(2) $+ \longleftrightarrow -$

(3) $s \longleftrightarrow s$

(4) $g \longleftrightarrow u$
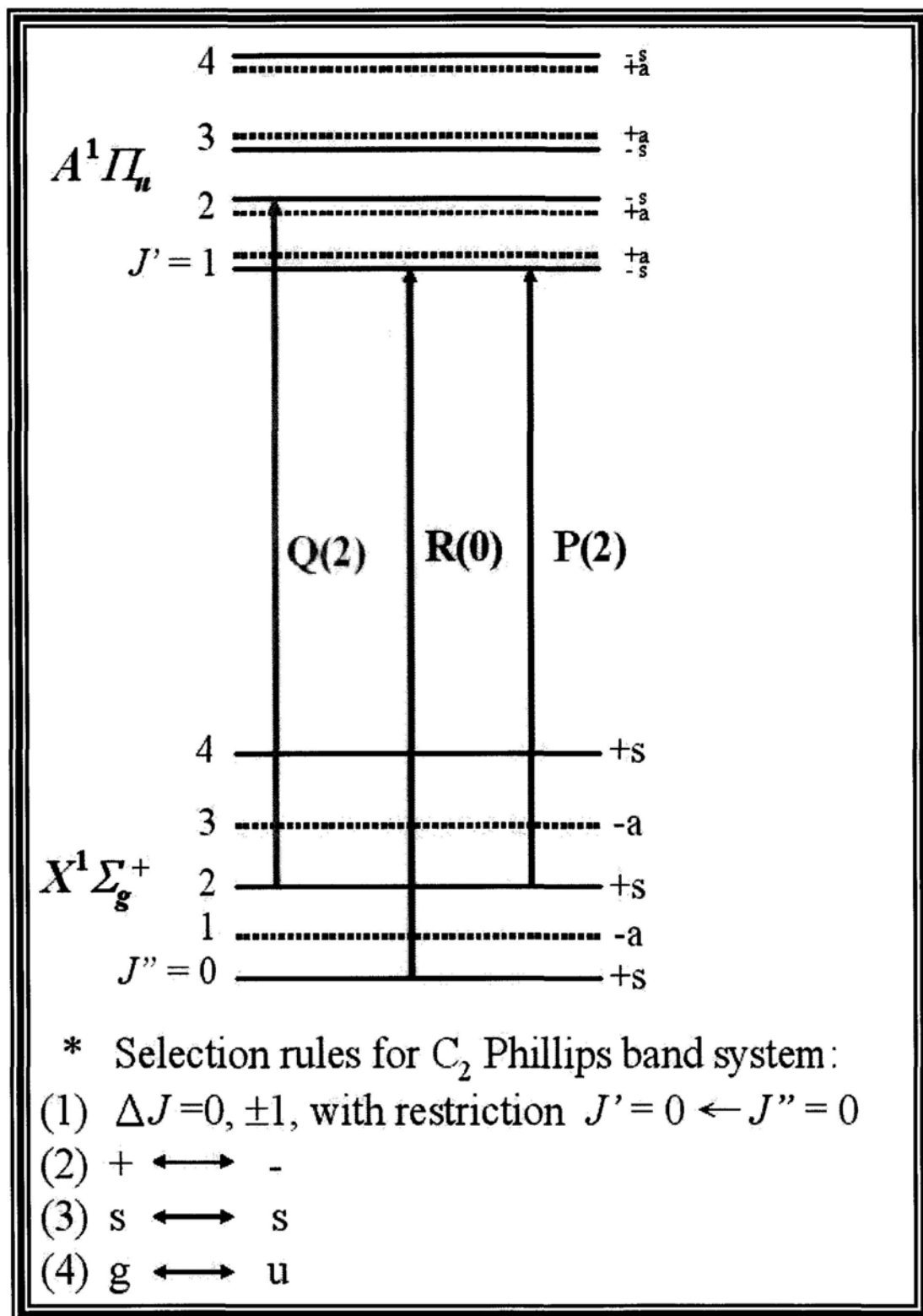
redox processes[40 and 41] such as flame combustion, explosion and discharges of carbon containing species. Furthermore, it provides an interesting topic for *ab initio* calculations[42, 43, 44 and 45] to determine whether the ground electronic state is a singlet or triplet.

Studies of C_2 have a long history and a wealth of information has been documented.[41] Numerous low-lying electronic states of C_2 have been predicted theoretically and observed using emission and absorption spectroscopy.[41] In summarizing these C_2 states, they can be divided into two manifolds: singlet state manifold and triplet state manifold (Fig. 20).[41 and 46] Different band systems have been studied including the Ballik-Ramsay band system ($b^3\Sigma_g^- - a^3\Pi_u$), Swan band system ($d^3\Pi_g - a^3\Pi_u$) and the Fox-Herzberg band system ($e^3\Pi_g - a^3\Pi_u$) of triplet manifold and the Phillips band system ($A^1\Pi_u - X^1\Sigma_g^+$), the Deslandres d'Azambuja band system ($C^1\Pi_g - A^1\Pi_u$), the Mulliken band system ($D^1\Sigma_u^+ - X^1\Sigma_g^+$) and the Freymark band system ($E^1\Sigma_g^+ - A^1\Pi_u$) of singlet manifold.

According to Clementi,[47] the Phillips band system was the weakest band systems among the low-lying states C_2 (TABLE 4) due to its weak oscillator strength (For instance, 0.0027 for Phillips band system compared to 0.0485 for Swan band system). Because of the weakness of the Phillips band system, only zero-background emission spectroscopy in the gas discharges proves to provide

Fig. 20 The energy diagram showing different electronic band systems of C_2.[41 and 46] They can be divided into two manifolds: singlet manifold and triplet manifold.

The energy diagram showing various electronic transitions of C_2
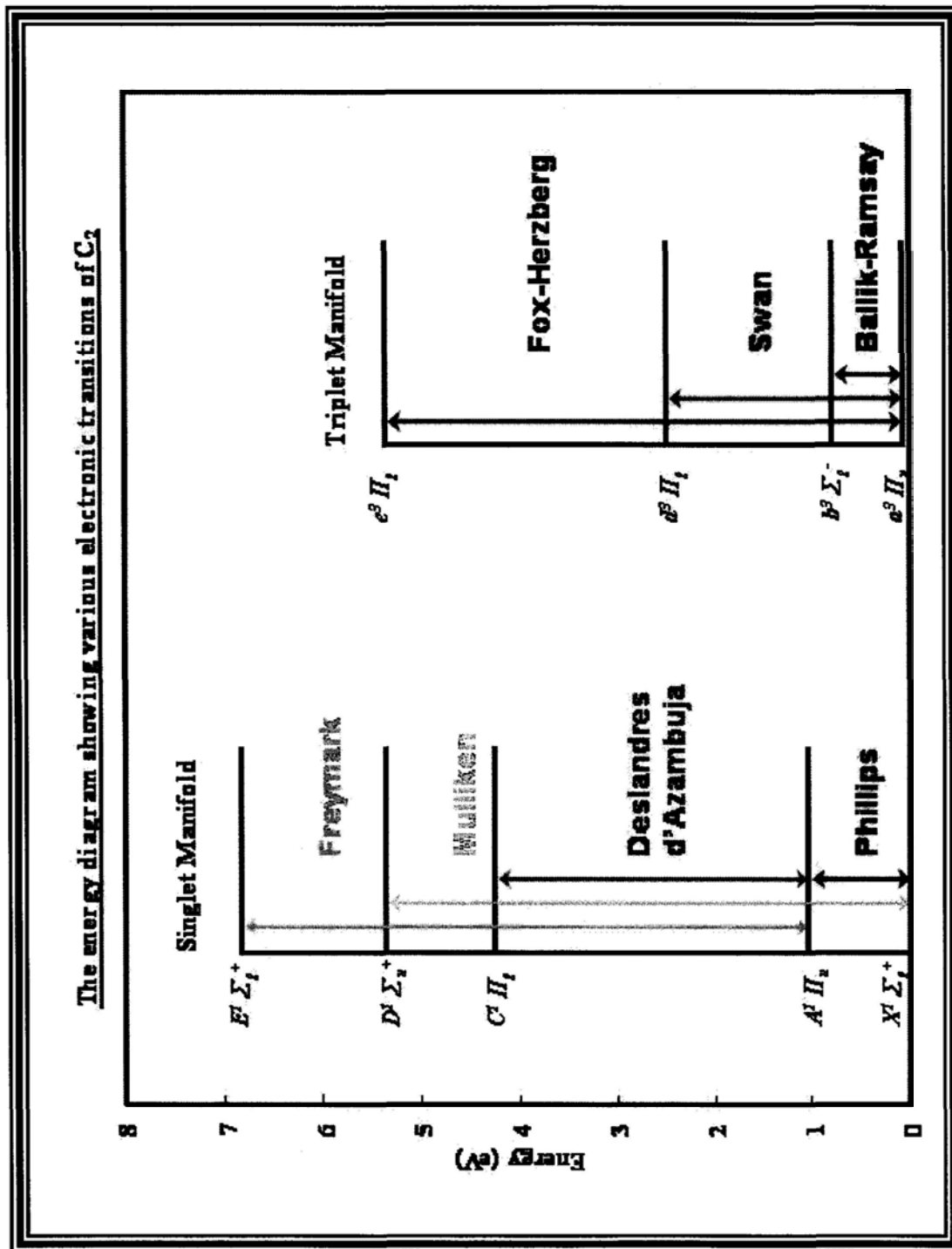
TABLE 4   Predicted oscillator strength for transitions in C_2.[47] Phillips band system has the smallest calculated oscillator strength; hence, it is expected to be the weakest band system of C_2.

Electronic transition band system		Calculated oscillator strength, f *
$b^3\Sigma_g^- - a^3\Pi_u$	Ballik-Ramsay	+0.0066
$d^3\Pi_g - a^3\Pi_u$	Swan	+0.0485
$e^3\Pi_g - a^3\Pi_u$	Fox-Herzberg	+0.8184
$A^1\Pi_u - X^1\Sigma_g^+$	Phillips	+0.0027
$C^1\Pi_g - A^1\Pi_u$	Deslandres d'Azambuja	+0.0650
$D^1\Sigma_u^+ - X^1\Sigma_g^+$	Mulliken	+0.1025

*   Data obtained from

E. Clementi, *Ap. J.* **132**, 898 (1960).

sufficient sensitivity for observing the transitions. On the other hand, the very weak

transitions are buried in the strong radiation background in case of absorption

spectroscopy. The spectrum of the C_2 Phillips system ($A^1\Pi_u$ - $X^1\Sigma_g^+$ or

$KK(\sigma_g2s)^2(\sigma_u2s)^2(\pi_u2p)^3(\sigma_u2p)^1$ - $KK(\sigma_g2s)^2(\sigma_u2s)^2(\pi_u2p)^4$ in electronic configuration)

was first observed by J. G. Phillips[48] in the emission of benzene/helium discharge

(Fig. 21) in 1948. Five rovibronic bands corresponding to (2-0), (3-1), (3-0), (4-1)

and (5-2) of C_2 were identified and analyzed. In 1963, Ballik and Ramsay[49]

recorded the emission spectrum of C_2 in the hydrogen gas discharges using a pair of

carbon electrodes. Nine more rovibronic bands, namely (0-0), (0-1), (4-0), (5-1),

(6-2), (6-3), (7-3), (8-3) and (8-4) of the Phillips system of C_2 were identified. The

analysis of the emission spectrum has led them to propose that the ground electronic

state of C_2 should be singlet $X^1\Sigma_g^+$ state not triplet $a^3\Pi_u$ state. In 1970, Marenin and

Johnson[50] accomplished a comprehensive analysis of the Phillips band system after

global fit by combining the data of Ballik and Ramsay[49] to obtain a new set of

consistent parameters. The development of modern FT-IR spectroscopy in the

1970s made possible the study of Phillips system at high resolution with reasonable

signal-to-noise ratio. In 1977, Chauville et al.[51] recorded five new bands ((0-2),

(1-0), (1-2), (2-1) and (4-2)) in the emission spectrum of a C_2H_2/O_2 flame using a

FT-IR spectrometer at moderate resolution to obtain a new set of molecular constants

Fig. 21 The first spectrum of Phillips band systems of C_2 obtained by J. G. Phillips[48] in 1948. The (2-0) band and (3-1) band are shown where the band heads of these bands are 8750.8 Å and 8980.5 Å respectively.
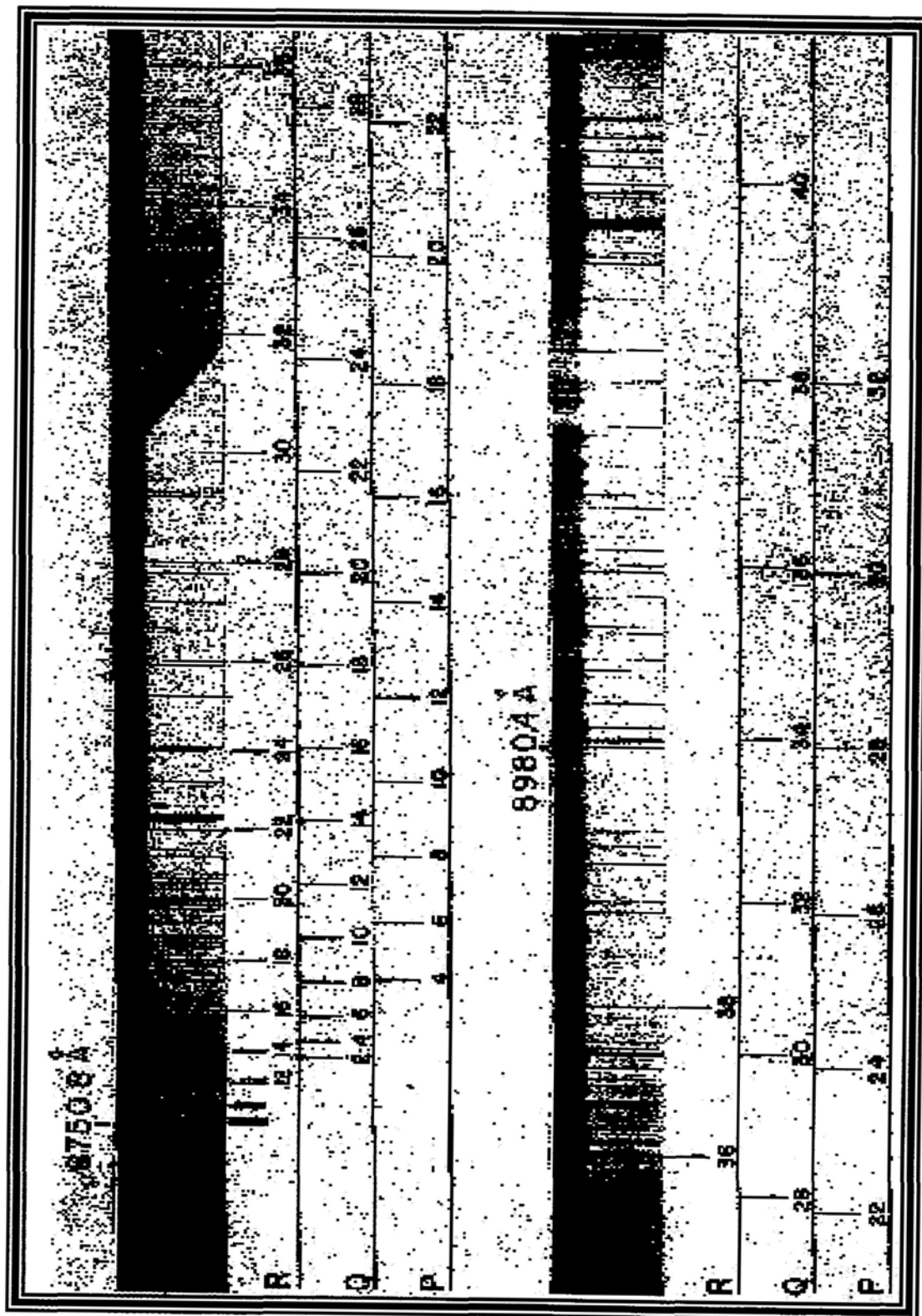
based on least-squares fitting. In the emission of argon discharges using a carbon hollow cathode, Davis *et al.*[52] recorded the (2-3), (1-3) and (2-4) bands of the Phillips system using high resolution FT-IR spectrometer in 1988 to extend the equilibrium parameters to higher vibrational levels. Douay *et al.*[53] extended the measurements using FT-IR emission spectroscopy to rovibronic bands: (3-3), (4-4), (5-5), (3-5) and (4-6) in the CH_4/He and C_3H_4/Ar discharges which allowed for the determination of high anharmonicity constants $\omega_e z_e$ and $\omega_e a_e$ in the $X^1\Sigma_g^+$ state. A list of the observed rovibronic bands is given in TABLE 5.

The previous measurements of the Phillips band system were made possible using zero-background emission spectroscopy, in which the C_2 transitions were detected from the emission of discharges of carbon-containing species mixed with inert gases. Therefore, the success of these emission experiments requires sufficient population of C_2 in the excited $A^1\Pi_u$ state under drastic discharge conditions. On the other hand, absorption spectroscopy probing C_2 in the ground $X^1\Sigma_g^+$ state can be carried out under much milder discharge conditions. The sensitivity of traditional absorption spectroscopy is limited by power fluctuation of the background source that obscures small absorption signals. As discussed in Chapter 2, the apparatus built in our laboratory are suited for pursuing zero-background absorption spectroscopy at high resolution and sensitivity. It has been found that our discharge

TABLE 5   A summary for the previous experiments of Phillips band system in C$_2$. Different vibrational transitions, Δv, for the upper electronic level (v') and lower electronic level (v'') are grouped. Our experimental results are highlighted into red colour, and the references are indicated by the corresponding blue number.

Δv $v'-v''$	-2	-1	0	+1	+2	+3	+4	+5
	0-2[3,4,5]	0-1[2,3,5]	0-0[2,3,5]	1-0[3]	2-0[1,3]	3-0[1,2]	4-0[2]	
	1-3[4,5]	1-2[3,5]		2-1[3,5]	3-1[1,3]	4-1[1,2]	5-1[2]	
	2-4[4,5]	2-3[4]			4-2[3]	5-2[1,2]	6-2[2]	
	3-5[5]		3-3[5]			6-3[2]	7-3[2]	8-3[2]
	4-6[5]		4-4[5]				8-4[2]	
			5-5[5]					

C$_2$ Phillips band system

*Red label indicated our results

[1] J. G. Phillips, Ap. J. 107, 389 (1948).

[2] E. A. Ballik and D. A. Ramsay, Ap. J. 137, 84 (1963).

[3] J. Chauville, J. P. Maillard, and A. W. Mantz, J. Mol. Spectrosc. 68, 399 (1977).

[4] S. P. Davis, M. C. Abrams, J. G. Phillips, and M. L. P. Rao, J. Opt. Soc. Am. B 5, 10 (1988).

[5] M. Douay, R. Nietmann and P. F. Bernath, J. Mol. Spectrosc. 131, 250 (1988).

system produced C_2 radicals at a rotational temperature of about 260 K using ethanol

cooling at about 200 K, which is much lower than previous studies.

3D Optimization of discharge conditions for the production of C_2

As discussed in Chapter 2, the discharge conditions such as voltage, current,

frequency, gas mixtures and temperature are crucial parameters in generating a

particular species. A gas mixture of CH_4/He in a ratio of 1:170 with a total pressure

of ~860 mTorr was used in producing C_2 radicals in our studies. This ratio was

determined by optimizing the intensity of C_2 transitions at different mixing ratio.

As shown in Fig. 22 and Fig. 23, the absorption signals of C_2 was maximized at

about 5 mTorr of CH_4 pressure. In a similar way, the discharge frequency was

determined to be about 5 kHz to give the best signal-to-noise ratio (Fig. 24).

In principle, our discharge power supply is capable of operating at about 2.5 A

peak-to-peak current. However, using such a high current generates too much heat

on the hollow cathode that the cooling efficiency of circulator becomes insufficient.

More importantly, a layer of carbon soot easily builds up on the wall of the hollow

cathode under these violent discharge conditions which makes the discharge unstable.

Therefore, a milder discharge voltage (~1500 V) and current (1 A as shown in Fig. 14)

was used in our experiments. Under normal operations, stable discharges can be

Fig. 22 The C_2 signal at 12958.9208 cm^{-1} at different CH_4 pressure. The optimized CH_4 pressure is about 4-5 mTorr.
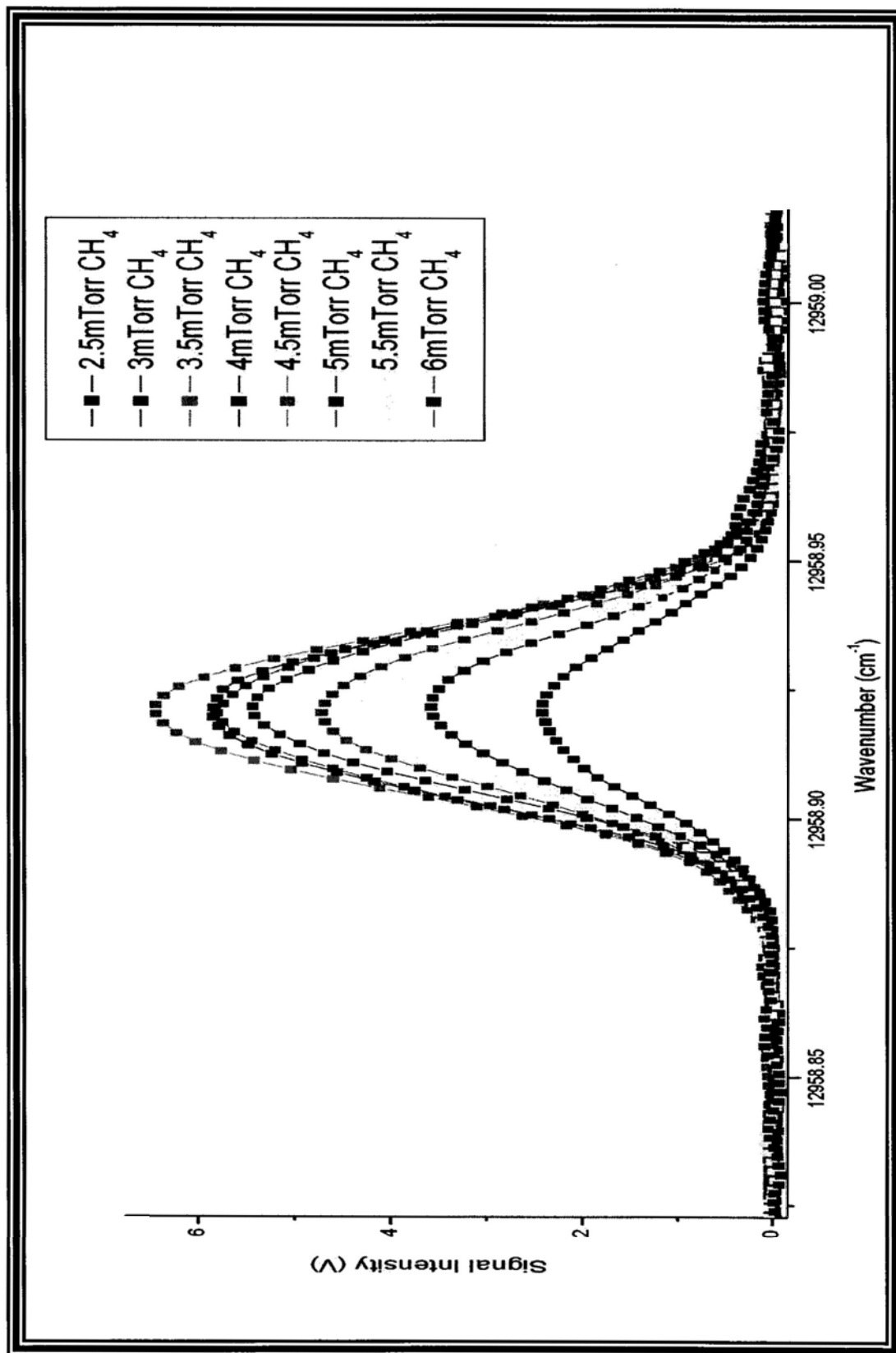
Fig. 23   The plot shown the relation between CH_4 pressure and the relative signal intensity by using C_2 signal at 12958.9208 cm^{-1}.   There is a trend of increase of the relative signal intensity when we increase CH_4 pressure.   But there is a maximum about 4.5-5 mTorr, and then saturate, if we continue to increase the CH_4 pressure.

Relative Intensity against Methane Pressure
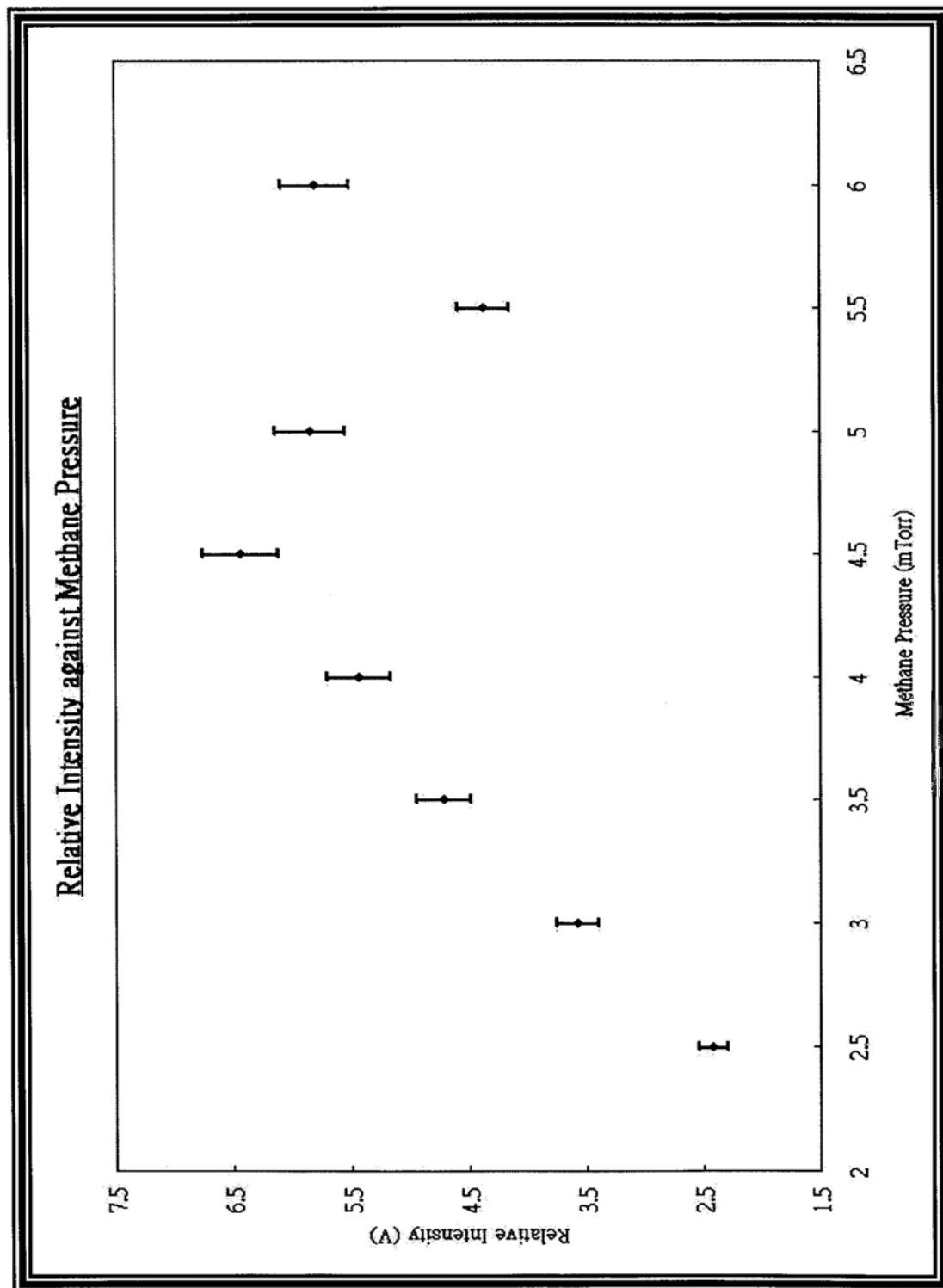
Fig. 24   The signal-to-noise ratio against the discharge frequency by using C_2

signal at 12958.9208 cm^{-1}.   There is a trend of increase of the signal-to-noise ratio

when we increase the discharge frequency.   The signal has maximized at about 5

kHz as shown in the figure.
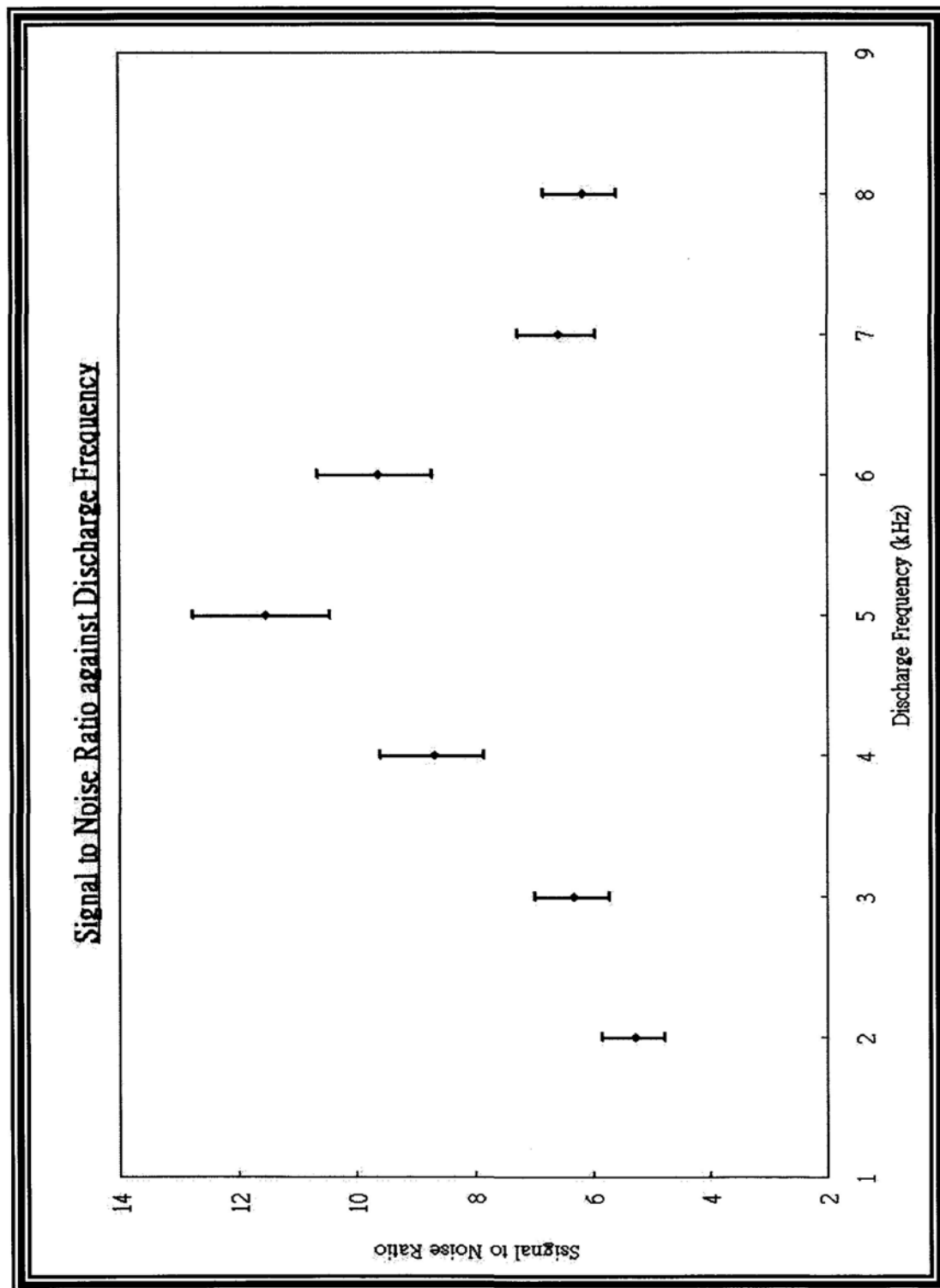
maintained for about 10 hours using these conditions. After operating for about 10 hours, the hollow cathode tube was cleaned and polished to remove the carbon soot that caused unstable discharges.

3E Observation and preliminary analysis

A total of thirteen rovibronic bands of about 550 transitions due to carbon containing species have been observed in the 10300 cm^{-1} to 14250 cm^{-1} region. Based on the works of Ballik and Ramsay[49] and Chauville et al.,[51] eleven bands of a total of about 300 transitions are assigned to be the Phillips system. These bands are (2-0), (3-1) and (4-2) bands of the $\Delta v = +2$ sequence, (3-0), (4-1), (5-2) and (6-3) bands of the $\Delta v = +3$ sequence and (5-1), (6-2), (7-3) and (8-4) bands of the $\Delta v = +4$ sequence, respectively. The high sensitivity and resolution of our system allowed to observe most low J transitions missed in the earlier work of Ballik and Ramsay.[49] Among the observed bands, the signal-to-noise (S/N) ratio varies from about 250 for the strong lines to about 5 for the weak lines. In Fig. 25, a small portion of the experimental spectrum is shown to illustrate the S/N ratio. A stick spectrum regenerated from these observed transitions with relative intensity is shown in Fig. 26. It should be noted that the variation of relative intensity may be significantly affected by the laser output power. In case, atmospheric water absorption is nearby,

Fig. 25 Typical spectrum of Phillips band systems of C_2 in the region between 12625 cm^{-1} and 12640 cm^{-1}. An illustration of showing the experimental S/N ratio is then given out.
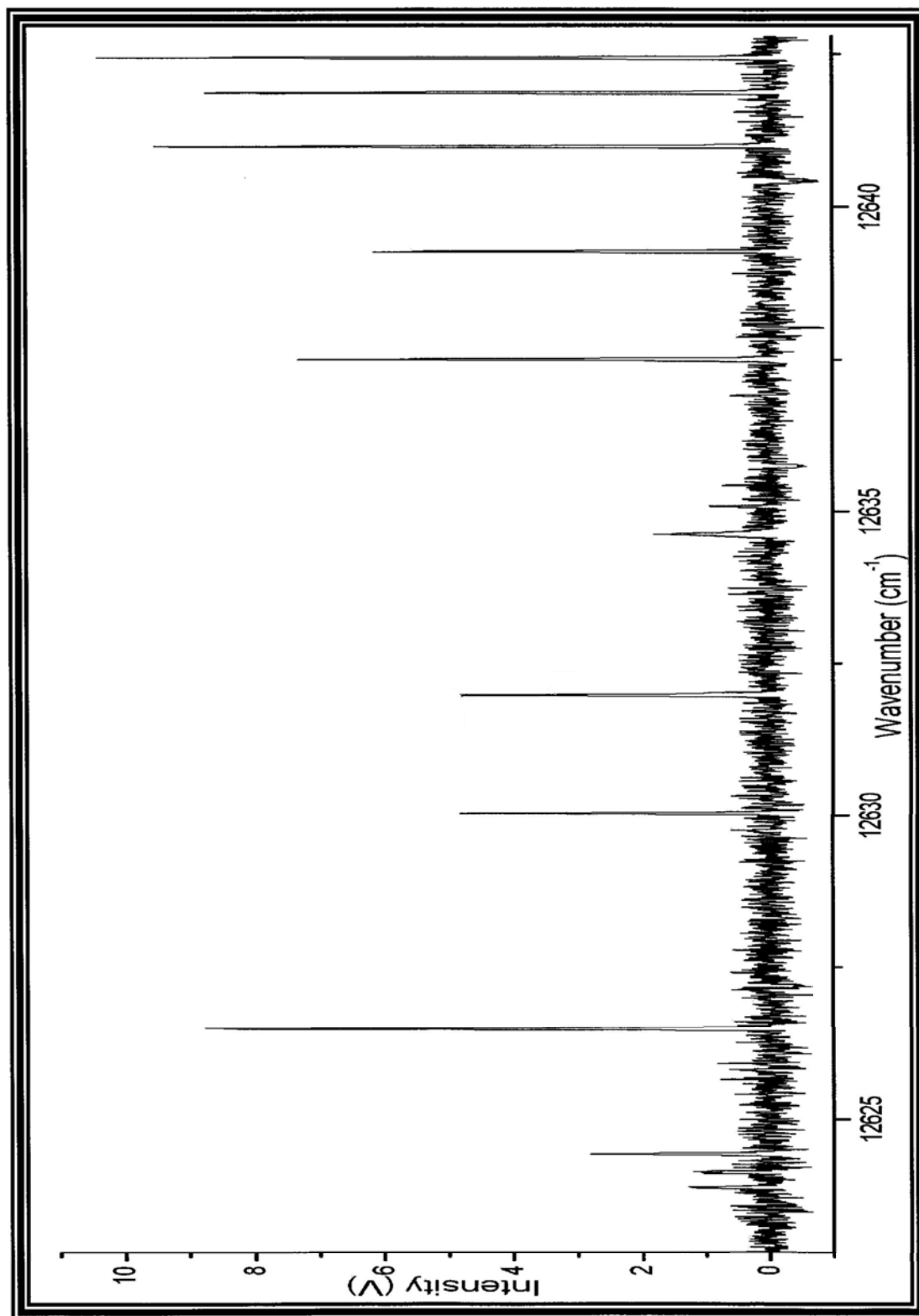
Fig. 26   Stick diagram regenerated based on the observed transitions.   The

vibronic bands of the Phillips syatem are shown with different colour assignments.
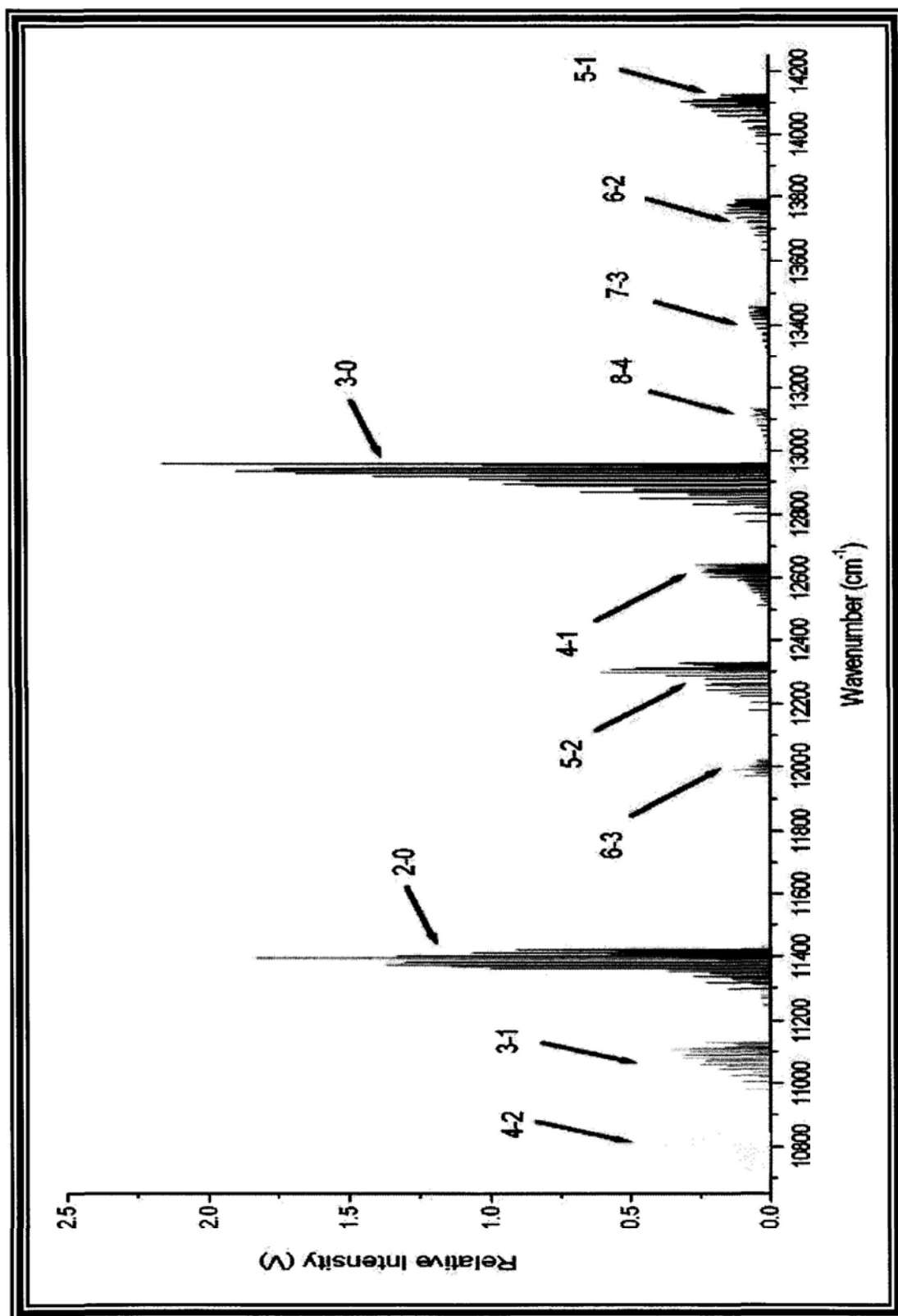
and the laser output power can be very low to give rise to lower signal-to-noise ratio.

The observed C_2 transitions have given a typical linewidth of ~0.033 cm^{-1} (FWHM) as shown in Fig. 27. In the near infrared region, this linewidth is mainly due to effect of Doppler broadening (*i.e.* Doppler width,[2 and 18] $\Delta \upsilon_D$) which is known as

$$\Delta v_D = \frac{2v}{c}\sqrt{2\ln 2 \times \frac{kT_{tran}}{m}}$$

$$\frac{\Delta v_D}{v} = 7.16 \times 10^{-7}\sqrt{\frac{T_{tran}}{M}}$$

where υ is the transition frequency, k is the Boltzmann constant, c is the speed of the light, m is the mass of the species, M is molecular mass of the species and T_{tran} is translational temperature. The average translational temperature of ~350±100 K has then been determined based on the above equation. It is seen that the translational temperature was much higher than the coolant temperature of 200 K suggesting that the plasma had not reached thermal equilibrium.

While the plasma may not reach equilibrium translationally, whose rotational motion is appeared to achieve Boltzmann distribution,[2] as shown in Fig. 28. The rotational equilibrium is observed for all measured rovibronic bands of C_2, with levels of J-value up to about 20. The rotational temperature[2] (T_{rot}) is estimated to be about 260 K according to the J level with maximum intensity (J_{max}) by the following equation[2, 54]

Fig. 27 One of the peak in observed C_2 Phillips band at ~11402 cm^{-1}. The absorption peak gives a linewidth of ~0.033 cm^{-1} where translational temperature is ~400 K.
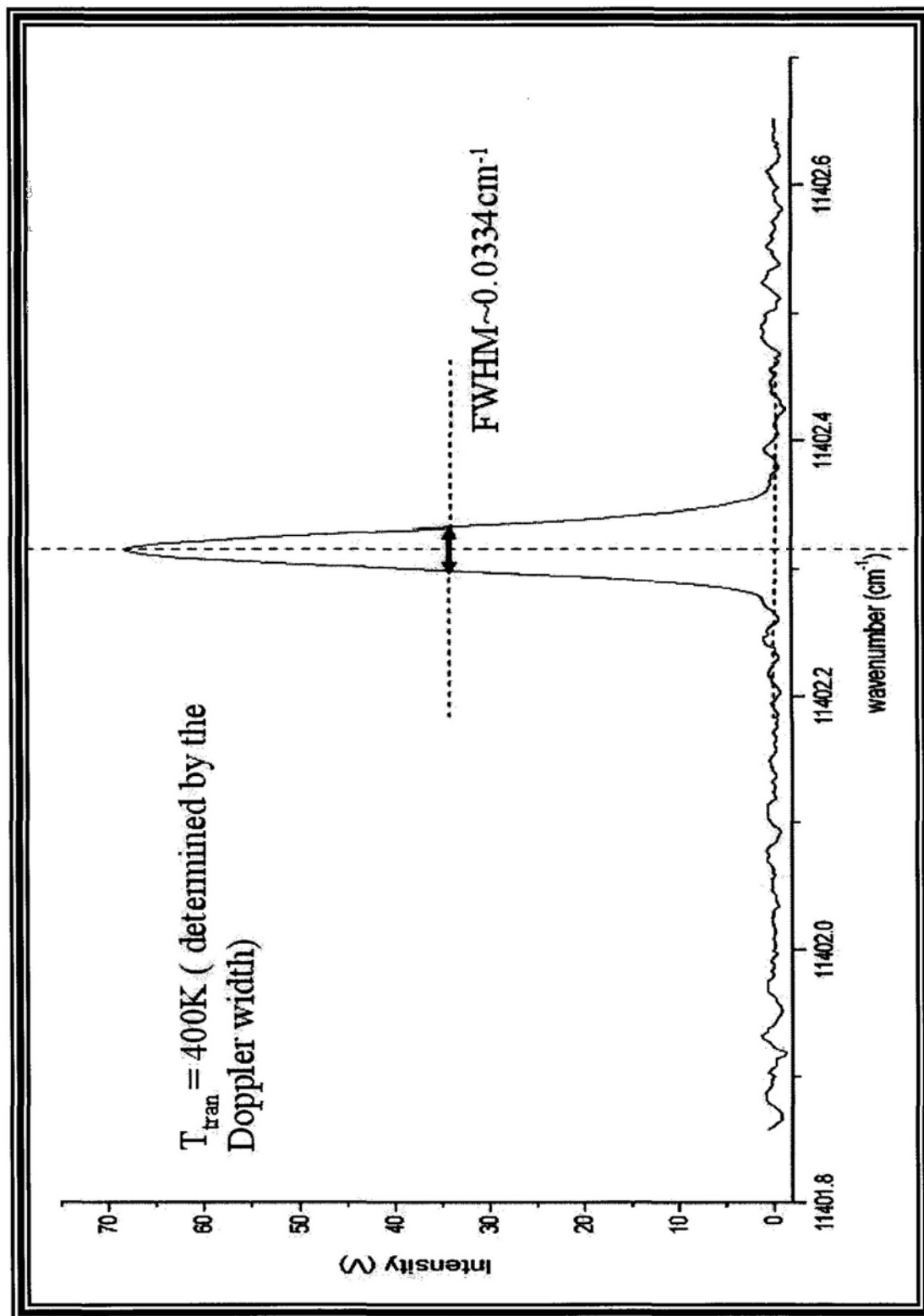
Fig. 28 The intensity variation with different rotation levels in P branch of C_2 Phillips band. The rotation level with maximum intensity (J_{max}) is about 6~8, which rotational temperature is ~260 K.

The intensity variation of the J th rotation level in P branch of C_2 (3-0) Phillips band

T_{rot} = 260K
(determined by relative intensity of rotational levels)
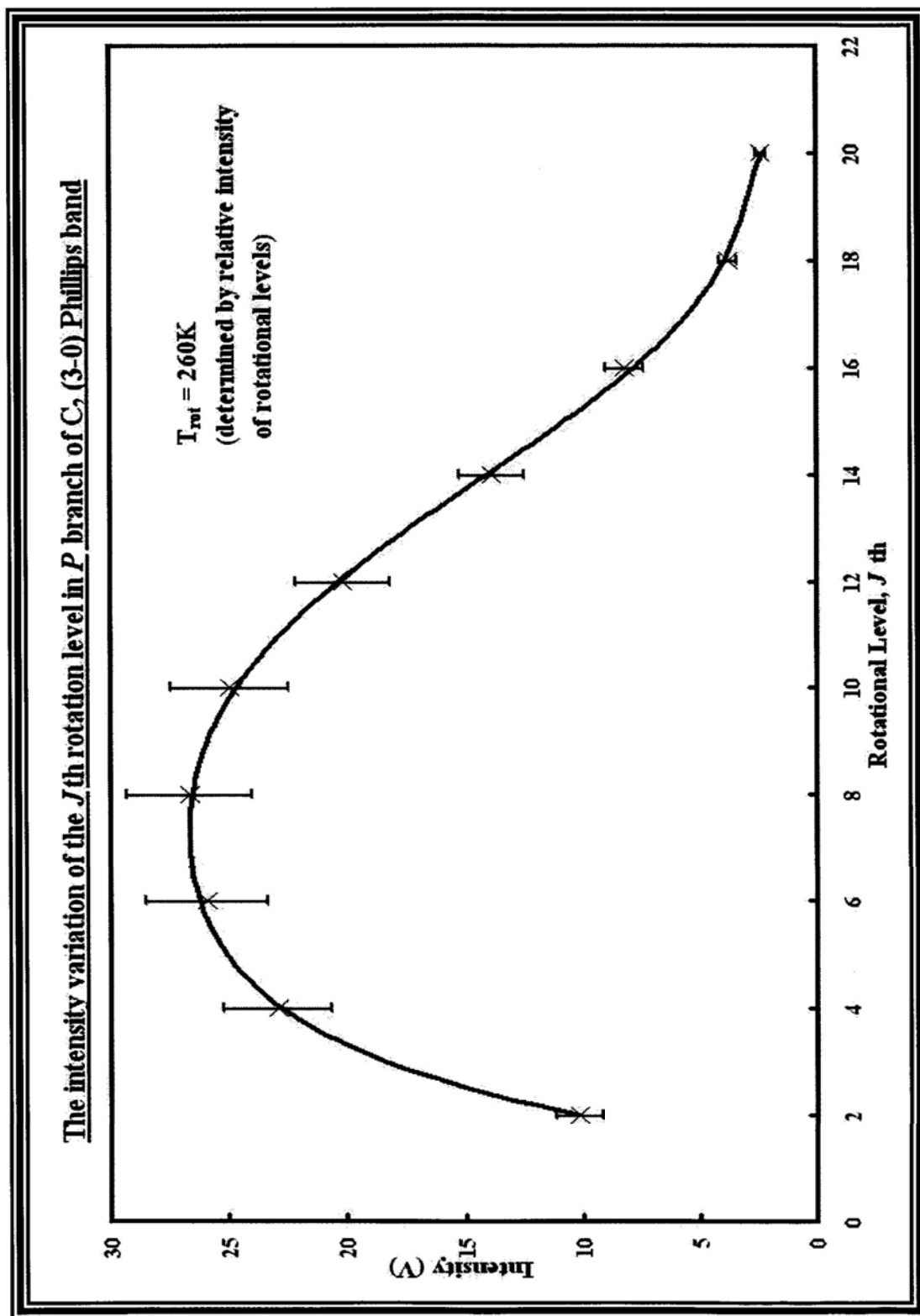
$$J_{max} = \sqrt{\frac{kT_{rot}}{2Bhc}} - \frac{1}{2}$$

$$= 0.5896\sqrt{\frac{T_{rot}}{B}} - \frac{1}{2}$$

where h is the Planck constant and B is the rotational constant. Since both

rotational and translational temperatures were higher than the coolant temperature

(~200 K), it is expected that the gaseous plasma may not be reached thermal

equilibrium with the surroundings.

By comparing the Franck–Condon factors[55] ($f_{v'v''}$) and the relative intensities for

different vibronic bands in each sequence, a vibrational temperature[56] (T_{vib}) was then

estimated to be about 3000 ±1000K using the following equation[2]

$$\log[I_{v'v''} / f_{v'v''}] = \log[N_{v''}] - \frac{E_{vib}}{kT_{vib}}$$

from the equation

$$I_{v'v''} \propto N_{v''} f_{v'v''} e^{-\frac{E_{vib}}{kT_{vib}}}$$

where is $I_{v'v''}$, $N_{v''}$ and E_{vib} are the vibrational intensity, the number of molecule in the

lower state and vibrational energy respectively.

3F Spectroscopic analysis

The observed transitions in each vibronic band were assigned based on the

previous work of Ballik and Ramsay[49] and Chauville et al.[51] The observed

transition frequencies σ were fitted to the standard Hamiltonian[52] for $^1\Pi$ - $^1\Sigma$

electronic transition:

$$\sigma = \sigma_o + B_{v'}J'(J'+1) - D_{v'}[J'(J'+1)]^2 - B_{v''}J''(J''+1) + D_{v''}[J''(J''+1)]^2$$
$$\pm \frac{1}{2}\{q_{B'}J'(J'+1) + q_{D'}[J'(J'+1)]^2\} \qquad \text{in cm}^{-1}$$

where σ_o is the vibronic frequency and other parameters carry the usual meaning in

spectroscopy. The $\pm$ sign in this equation accounts for the fact that the P and R

branches are associated to the upper level of the Λ-doublet whereas the Q branch is

associated to the lower level of Λ-doublet. The band-specific molecular constants

from each of the eleven observed C_2 Phillips bands obtained from the least-squares

fitting are listed in TABLE 6. The assigned transitions together with the calculated

frequencies are listed in TABLE 7 to TABLE 17. Most transitions are observed

within 0.005 cm^{-1} from the calculated values. The difference is about the same

accuracy of the frequency calibration. The assigned transitions in each band are

shown in Fig. 29 to Fig. 39.

The quality of the least-squares fitting for each individual band is shown by the

residual plots illustrated in Fig. 40 to Fig. 50. In each of these plots, the "best fit

datum" is set as the standard reference point at the center of the plot. The other data

are arranged based on the square of the residue (between the observed and calculated

transition frequency) from the reference point. In other words, a good fitting should

give a near straight line that is almost horizontal. In case of perturbation, an abrupt

change of slope is expected. It is seen that, for instance, the (5-1) band as shown in

TABLE 6   Molecular constants obtained by individual fit with a total of eleven observed C_2 Phillips bands.

Parameters	(4-2)	(3-1)	(2-0)	(6-3)	(5-2)	(4-1)
σ_o	10832.3542(34)	11120.3388(18)	11412.2662(32)	12011.4367(31)	12319.1530(58)	12631.5462(97)
$B_{v'}$	1.53921(28)	1.55679(13)	1.57412(21)	1.50469(39)	1.52281(38)	1.53961(71)
$D_{v'} \times 10^6$	6.56(70)	6.83(26)	6.88(39)	8.1(46)	10.15(79)	7.0(18)
$B_{v''}$	1.77415(29)	1.79290(13)	1.81118(21)	1.75555(35)	1.77502(39)	1.79286(74)
$D_{v''} \times 10^6$	7.22(77)	7.25(27)	7.13(37)	8.7(48)	9.95(86)	6.7(20)
$q_{B'} \times 10^4$	-1.68(66)	-1.80(35)	-0.96(61)	-2.0(11)	-0.8(13)	-3.7(18)
$q_{D'} \times 10^8$	-1(22)	-3(12)	-38(18)	30(120)	-98(43)	84(67)
variance	0.000021	0.000006	0.000017	0.000006	0.000055	0.000139

Parameters	(3-0)	(8-4)	(7-3)	(6-2)	(5-1)
σ_o	12947.8230(17)	13122.4906(40)	13449.1293(51)	13781.4361(98)	14118.3430(29)
$B_{v'}$	1.55671(11)	1.46928(25)	1.48689(38)	1.50457(62)	1.52199(18)
$D_{v'} \times 10^6$	6.55(18)	6.84(63)	7.14(97)	7.1(13)	6.52(31)
$B_{v''}$	1.81103(11)	1.73608(26)	1.75547(38)	1.77428(63)	1.79286(18)
$D_{v''} \times 10^6$	6.97(19)	7.52(69)	7.9(10)	6.9(14)	6.97(31)
$q_{B'} \times 10^4$	-2.04(27)	-1.86(69)	-2.7(11)	-4.4(20)	-2.03(52)
$q_{D'} \times 10^8$	4.9(73)	-11(26)	55(42)	129(72)	4(15)
variance	0.000006	0.000015	0.000037	0.000140	0.000016

*All values are given in cm^{-1} and all the error quoted is one standard deviation.

TABLE 7   Assignment of transitions in (4-2) band of the C_2 Phillips band system.

Branch	J'	J''	Observed value (cm^{-1})	Calculated value (cm^{-1})	Difference (cm^{-1})
P	1	2	10824.7899	10824.7878	0.0021
	3	4	10815.3379	10815.3427	-0.0048
	5	6	10804.0192	10804.0206	-0.0014
	7	8	10790.8331	10790.8234	0.0097
	9	10	10775.7512	10775.7533	-0.0021
	11	12	10758.8094	10758.8128	-0.0034
	13	14	10740.0009	10740.0046	-0.0037
	15	16	10719.3350	10719.3316	0.0034
Q	2	2	10830.9473	10830.9451	0.0022
	4	4	10827.6582	10827.6574	0.0008
	6	6	10822.4922	10822.4914	0.0008
	8	8	10815.4444	10815.4480	-0.0036
	10	10	10806.5295	10806.5281	0.0014
	12	12	10795.7358	10795.7328	0.0030
	14	14	10783.0672	10783.0637	0.0035
	16	16	10768.5208	10768.5226	-0.0018
	18	18	10752.1042	10752.1112	-0.0070
	20	20	10733.8362	10733.8321	0.0041
R	1	0	10835.4312	10835.4325	-0.0013
	3	2	10840.1779	10840.1781	-0.0002
	5	4	10843.0402	10843.0419	-0.0017
	7	6	10844.0273	10844.0231	0.0042
	9	8	10843.1126	10843.1209	-0.0083
	11	10	10840.3319	10840.3352	-0.0033
	13	12	10835.6730	10835.6658	0.0072
	15	14	10829.1178	10829.1129	0.0049
	17	16	10820.6731	10820.6770	-0.0039
	19	18	10810.3573	10810.3587	-0.0014
	21	20	10798.1597	10798.1590	0.0007

TABLE 8   Assignment of transitions in (3-1) band of the C_2 Phillips band system.

Branch	J'	J''	Observed value (cm^{-1})	Calculated value (cm^{-1})	Difference (cm^{-1})
P	1	2	11112.6935	11112.6950	-0.0015
	3	4	11103.1626	11103.1631	-0.0005
	5	6	11091.7425	11091.7447	-0.0022
	7	8	11078.4418	11078.4414	0.0004
	9	10	11063.2571	11063.2553	0.0018
	11	12	11046.1890	11046.1883	0.0007
	13	14	11027.2446	11027.2427	0.0019
	15	16	11006.4196	11006.4208	-0.0012
	17	18	10983.7246	10983.7252	-0.0006
Q	2	2	11118.9211	11118.9227	-0.0016
	4	4	11115.6173	11115.6186	-0.0013
	6	6	11110.4239	11110.4268	-0.0029
	8	8	11103.3456	11103.3478	-0.0022
	10	10	11094.3839	11094.3821	0.0018
	12	12	11083.5308	11083.5307	0.0001
	14	14	11070.7948	11070.7945	0.0003
	16	16	11056.1776	11056.1746	0.0030
	18	18	11039.6693	11039.6724	-0.0031
	20	20	11021.2900	11021.2893	0.0007
R	1	0	11123.4556	11123.4521	0.0035
	3	2	11128.2601	11128.2611	-0.0010
	5	4	11131.1812	11131.1786	0.0026
	7	6	11132.2062	11132.2036	0.0026
	9	8	11131.3382	11131.3353	0.0029
	11	10	11128.5706	11128.5730	-0.0024
	13	12	11123.9174	11123.9160	0.0014
	15	14	11117.3597	11117.3639	-0.0042
	17	16	11108.9144	11108.9165	-0.0021
	19	18	11098.5768	11098.5738	0.0030

TABLE 9   Assignment of transitions in (2-0) band of the C_2 Phillips band system.

Branch	J'	J''	Observed value (cm^{-1})	Calculated value (cm^{-1})	Difference (cm^{-1})
P	1	2	11404.5498	11404.5476	0.0022
	3	4	11394.9324	11394.9335	-0.0011
	5	6	11383.4241	11383.4254	-0.0013
	7	8	11370.0220	11370.0247	-0.0027
	9	10	11354.7278	11354.7328	-0.0050
	11	12	11337.5541	11337.5513	0.0028
	13	14	11318.4779	11318.4816	-0.0037
	15	16	11297.5292	11297.5252	0.0040
	17	18	11274.6907	11274.6837	0.0070
	19	20	11249.9532	11249.9587	-0.0055
Q	2	2	11410.8463	11410.8442	0.0021
	6	6	11402.3149	11402.3129	0.0020
	8	8	11395.2046	11395.2043	0.0003
	12	12	11375.3094	11375.3045	0.0049
	14	14	11362.5135	11362.5151	-0.0016
	16	16	11347.8316	11347.8342	-0.0026
	18	18	11331.2605	11331.2631	-0.0026
	20	20	11312.8058	11312.8033	0.0025
R	1	0	11415.4152	11415.4143	0.0009
	3	2	11420.2874	11420.2873	0.0001
	5	4	11423.2601	11423.2615	-0.0014
	7	6	11424.3364	11424.3355	0.0009
	11	10	11420.7769	11420.7781	-0.0012
	13	12	11416.1395	11416.1442	-0.0047
	15	14	11409.6035	11409.6050	-0.0015
	17	16	11401.1685	11401.1596	0.0089
	19	18	11390.8029	11390.8066	-0.0037

TABLE 10 Assignment of transitions in (6-3) band of the C_2 Phillips band system.

Branch	J'	J''	Observed value (cm^{-1})	Calculated value (cm^{-1})	Difference (cm^{-1})
P	3	4	11994.3868	11994.3832	0.0036
	5	6	11982.8482	11982.8497	-0.0015
Q	2	2	12009.9297	12009.9322	-0.0025
	4	4	12006.4188	12006.4218	-0.0030
	6	6	12000.9040	12000.9060	-0.0020
	8	8	11993.3856	11993.3851	0.0005
	10	10	11983.8632	11983.8599	0.0033
	12	12	11972.3297	11972.3313	-0.0016
R	1	0	12014.4464	12014.4458	0.0006
	3	2	12018.9617	12018.9577	0.0040
	5	4	12021.4586	12021.4598	-0.0012
	7	6	12021.9505	12021.9514	-0.0009
	9	8	12020.4322	12020.4317	0.0005
	11	10	12016.9014	12016.9004	0.0010
	13	12	12011.3565	12011.3576	-0.0011
	15	14	12003.8039	12003.8035	0.0004
	17	16	11994.2383	11994.2388	-0.0005
	19	18	11982.6648	11982.6645	0.0003

TABLE 11   Assignment of transitions in (5-2) band of the C_2 Phillips band system.

Branch	J'	J''	Observed value (cm^{-1})	Calculated value (cm^{-1})	Difference (cm^{-1})
P	1	2	12311.5555	12311.5487	0.0068
	3	4	12301.9333	12301.9283	0.0050
	5	6	12290.2982	12290.2933	0.0049
	7	8	12276.6484	12276.6451	0.0033
	9	10	12260.9826	12260.9847	-0.0021
	11	12	12243.3099	12243.3129	-0.0030
	13	14	12223.6288	12223.6302	-0.0014
	15	16	12201.9218	12201.9369	-0.0151
	17	18	12178.2452	12178.2331	0.0121
Q	2	2	12317.6422	12317.6400	0.0022
	4	4	12314.1072	12314.1098	-0.0026
	6	6	12308.5615	12308.5625	-0.0010
	8	8	12300.9984	12300.9985	-0.0001
	10	10	12291.4228	12291.4181	0.0047
	12	12	12279.8207	12279.8221	-0.0014
	14	14	12266.2087	12266.2110	-0.0023
	16	16	12250.5860	12250.5855	0.0005
	18	18	12232.9470	12232.9466	0.0004
R	1	0	12322.2017	12322.1985	0.0032
	3	2	12326.7697	12326.7750	-0.0053
	5	4	12329.3226	12329.3302	-0.0076
	7	6	12329.8527	12329.8617	-0.0090
	9	8	12328.3606	12328.3667	-0.0061
	11	10	12324.8424	12324.8421	0.0003
	13	12	12319.3013	12319.2846	0.0167
	21	20	12276.6484	12276.6514	-0.0030

TABLE 12   Assignment of transitions in (4-1) band of the C_2 Phillips band system.

Branch	J'	J''	Observed value (cm^{-1})	Calculated value (cm^{-1})	Difference (cm^{-1})
P	1	2	12623.8772	12623.8681	0.0091
	3	4	12614.1687	12614.1638	0.0049
	5	6	12602.4296	12602.4346	-0.0050
	7	8	12588.6819	12588.6821	-0.0002
	9	10	12572.9062	12572.9075	-0.0013
	11	12	12555.1150	12555.1124	0.0026
	13	14	12535.3002	12535.2983	0.0019
	15	16	12513.4649	12513.4669	-0.0020
Q	2	2	12630.0313	12630.0278	0.0035
	4	4	12626.4845	12626.4846	-0.0001
	6	6	12620.9145	12620.9162	-0.0017
	8	8	12613.3115	12613.3219	-0.0104
	10	10	12603.6797	12603.7005	-0.0208
	12	12	12592.0418	12592.0508	-0.0090
	14	14	12578.3669	12578.3712	-0.0043
	16	16	12562.6771	12562.6598	0.0173
	18	18	12544.9467	12544.9146	0.0321
	20	20	12525.1085	12525.1330	-0.0245
R	3	2	12639.2664	12639.2614	0.0050
	5	4	12641.8716	12641.8684	0.0032
	7	6	12642.4460	12642.4450	0.0010
	9	8	12640.9912	12640.9898	0.0014
	11	10	12637.5005	12637.5019	-0.0014
	13	12	12631.9802	12631.9803	-0.0001
	15	14	12624.4229	12624.4239	-0.0010
	17	16	12614.8294	12614.8317	-0.0023
	19	18	12603.2051	12603.2030	0.0021

TABLE 13   Assignment of transitions in (3-0) band of the C_2 Phillips band system.

Branch	J'	J''	Observed value (cm^{-1})	Calculated value (cm^{-1})	Difference (cm^{-1})
P	1	2	12940.0708	12940.0703	0.0005
	3	4	12930.2851	12930.2835	0.0016
	5	6	12918.4669	12918.4644	0.0025
	7	8	12904.6167	12904.6145	0.0022
	9	10	12888.7334	12888.7359	-0.0025
	11	12	12870.8296	12870.8305	-0.0009
	13	14	12850.8993	12850.9006	-0.0013
	15	16	12828.9457	12828.9486	-0.0029
	17	18	12804.9808	12804.9772	0.0036
	19	20	12778.9886	12778.9890	-0.0004
Q	2	2	12946.2967	12946.2977	-0.0010
	4	4	12942.7412	12942.7388	0.0024
	6	6	12937.1465	12937.1465	0.0000
	8	8	12929.5233	12929.5213	0.0020
	10	10	12919.8644	12919.8637	0.0007
	12	12	12908.1759	12908.1745	0.0014
	14	14	12894.4541	12894.4546	-0.0005
	16	16	12878.7037	12878.7049	-0.0012
	18	18	12860.9239	12860.9267	-0.0028
	20	20	12841.1237	12841.1214	0.0023
	22	22	12819.2902	12819.2903	-0.0001
R	1	0	12950.9320	12950.9362	-0.0042
	3	2	12955.6344	12955.6355	-0.0011
	5	4	12958.2974	12958.2976	-0.0002
	7	6	12958.9226	12958.9216	0.0010
	9	8	12957.5041	12957.5069	-0.0028
	11	10	12954.0534	12954.0526	0.0008
	13	12	12948.5550	12948.5585	-0.0035
	15	14	12941.0272	12941.0242	0.0030
	17	16	12931.4529	12931.4497	0.0032
	21	20	12906.1785	12906.1804	-0.0019

TABLE 14   Assignment of transitions in (8-4) band of the C_2 Phillips band system.

Branch	J'	J''	Observed value (cm^{-1})	Calculated value (cm^{-1})	Difference (cm^{-1})
P	3	4	13105.4051	13105.4013	0.0038
	7	8	13079.7877	13079.7848	0.0029
	9	10	13063.7854	13063.7839	0.0015
	11	12	13045.6558	13045.6579	-0.0021
	13	14	13025.4010	13025.4093	-0.0083
	15	16	13003.0467	13003.0411	0.0056
Q	2	2	13120.8893	13120.8904	-0.0011
	4	4	13117.1549	13117.1568	-0.0019
	6	6	13111.2896	13111.2903	-0.0007
	8	8	13103.2919	13103.2916	0.0003
	10	10	13093.1634	13093.1619	0.0015
	12	12	13080.9056	13080.9023	0.0033
	14	14	13066.5121	13066.5146	-0.0025
	16	16	13049.9982	13050.0006	-0.0024
	18	18	13031.3642	13031.3625	0.0017
R	5	4	13131.8384	13131.8414	-0.0030
	7	6	13131.8396	13131.8414	-0.0018
	9	8	13129.7034	13129.7029	0.0005
	11	10	13125.4297	13125.4254	0.0043
	13	12	13119.0045	13119.0089	-0.0044
	15	14	13110.4575	13110.4532	0.0043
	17	16	13099.7585	13099.7588	-0.0003
	19	18	13086.9249	13086.9261	-0.0012

TABLE 15   Assignment of transitions in (7-3) band of the C_2 Phillips band system.

Branch	J'	J''	Observed value (cm^{-1})	Calculated value (cm^{-1})	Difference (cm^{-1})
P	3	4	13431.8661	13431.8632	0.0029
	5	6	13420.0110	13420.0101	0.0009
	7	8	13406.0149	13406.0135	0.0014
	9	10	13389.8790	13389.8762	0.0028
	11	12	13371.5991	13371.6014	-0.0023
	13	14	13351.1897	13351.1928	-0.0031
	15	16	13328.6564	13328.6544	0.0020
Q	2	2	13447.5155	13447.5186	-0.0031
	4	4	13443.7546	13443.7607	-0.0061
	6	6	13437.8488	13437.8557	-0.0069
	8	8	13429.8060	13429.8043	0.0017
	10	10	13419.6073	13419.6071	0.0002
	12	12	13407.2659	13407.2651	0.0008
	14	14	13392.7797	13392.7795	0.0002
	16	16	13376.1523	13376.1515	0.0008
	18	18	13357.3842	13357.3826	0.0016
	20	20	13336.4731	13336.4746	-0.0015
R	1	0	13452.1045	13452.1027	0.0018
	3	2	13456.4366	13456.4368	-0.0002
	5	4	13458.6368	13458.6196	0.0172
	7	6	13458.6358	13458.6504	-0.0146
	9	8	13456.5323	13456.5291	0.0032
	11	10	13452.2594	13452.2559	0.0035
	13	12	13445.8272	13445.8314	-0.0042
	15	14	13437.2575	13437.2565	0.0010
	17	16	13426.5330	13426.5327	0.0003

TABLE 16   Assignment of transitions in (6-2) band of the C_2 Phillips band system.

Branch	J'	J''	Observed value (cm^{-1})	Calculated value (cm^{-1})	Difference (cm^{-1})
P	1	2	13773.8214	13773.7994	0.0220
	3	4	13764.0051	13764.0046	0.0005
	5	6	13752.0533	13752.0535	-0.0002
	7	8	13737.9445	13737.9477	-0.0032
	9	10	13721.6875	13721.6892	-0.0017
	11	12	13703.2853	13703.2803	0.0050
	13	14	13682.7182	13682.7232	-0.0050
	15	16	13660.0195	13660.0206	-0.0011
	17	18	13635.1773	13635.1752	0.0021
Q	2	2	13779.8208	13779.8192	0.0016
	4	4	13776.0421	13776.0461	-0.0040
	6	6	13770.1115	13770.1164	-0.0049
	8	8	13762.0143	13762.0291	-0.0148
	10	10	13751.7730	13751.7833	-0.0103
	12	12	13739.3695	13739.3775	-0.0080
	14	14	13724.8168	13724.8100	0.0068
	16	16	13708.1144	13708.0787	0.0357
	18	18	13689.1598	13689.1815	-0.0217
R	3	2	13788.8421	13788.8420	0.0001
	5	4	13791.0778	13791.0782	-0.0004
	7	6	13791.1522	13791.1523	-0.0001
	9	8	13789.0649	13789.0639	0.0010
	11	10	13784.8091	13784.8122	-0.0031
	13	12	13778.4009	13778.3972	0.0037
	15	14	13769.8201	13769.8186	0.0015
	17	16	13759.0759	13759.0765	-0.0006
	19	18	13746.1704	13746.1714	-0.0010

TABLE 17   Assignment of transitions in (5-1) band of the C_2 Phillips band system.

Branch	J'	J''	Observed value (cm^{-1})	Calculated value (cm^{-1})	Difference (cm^{-1})
P	1	2	14110.6324	14110.6298	0.0026
	3	4	14100.7470	14100.7503	-0.0033
	5	6	14088.7071	14088.7059	0.0012
	7	8	14074.4976	14074.4985	-0.0009
	9	10	14058.1269	14058.1300	-0.0031
	11	12	14039.6005	14039.6023	-0.0018
	13	14	14018.9184	14018.9179	0.0005
	15	16	13996.0801	13996.0790	0.0011
	17	18	13971.0934	13971.0885	0.0049
	19	20	13943.9455	13943.9489	-0.0034
Q	2	2	14116.7149	14116.7184	-0.0035
	4	4	14112.9434	14112.9278	0.0156
	6	6	14106.9700	14106.9714	-0.0014
	8	8	14098.8502	14098.8498	0.0004
	10	10	14088.5645	14088.5635	0.0010
	12	12	14076.1105	14076.1133	-0.0028
	14	14	14061.4993	14061.5002	-0.0009
	16	16	14044.7271	14044.7251	0.0020
	18	18	14025.7871	14025.7894	-0.0023
	20	20	14004.6958	14004.6946	0.0012
R	1	0	14121.3842	14121.3867	-0.0025
	3	2	14125.8444	14125.8478	-0.0034
	5	4	14128.1390	14128.1393	-0.0003
	7	6	14128.2598	14128.2605	-0.0007
	9	8	14126.2081	14126.2104	-0.0023
	11	10	14121.9896	14121.9886	0.0010
	13	12	14115.5951	14115.5946	0.0005
	15	14	14107.0294	14107.0281	0.0013
	17	16	14096.2895	14096.2892	0.0003
	19	18	14083.3764	14083.3779	-0.0015
	21	20	14068.2951	14068.2946	0.0005

Fig. 29 Stick spectrum of (4-2) band in C₂ Phillips system with relative intensity.
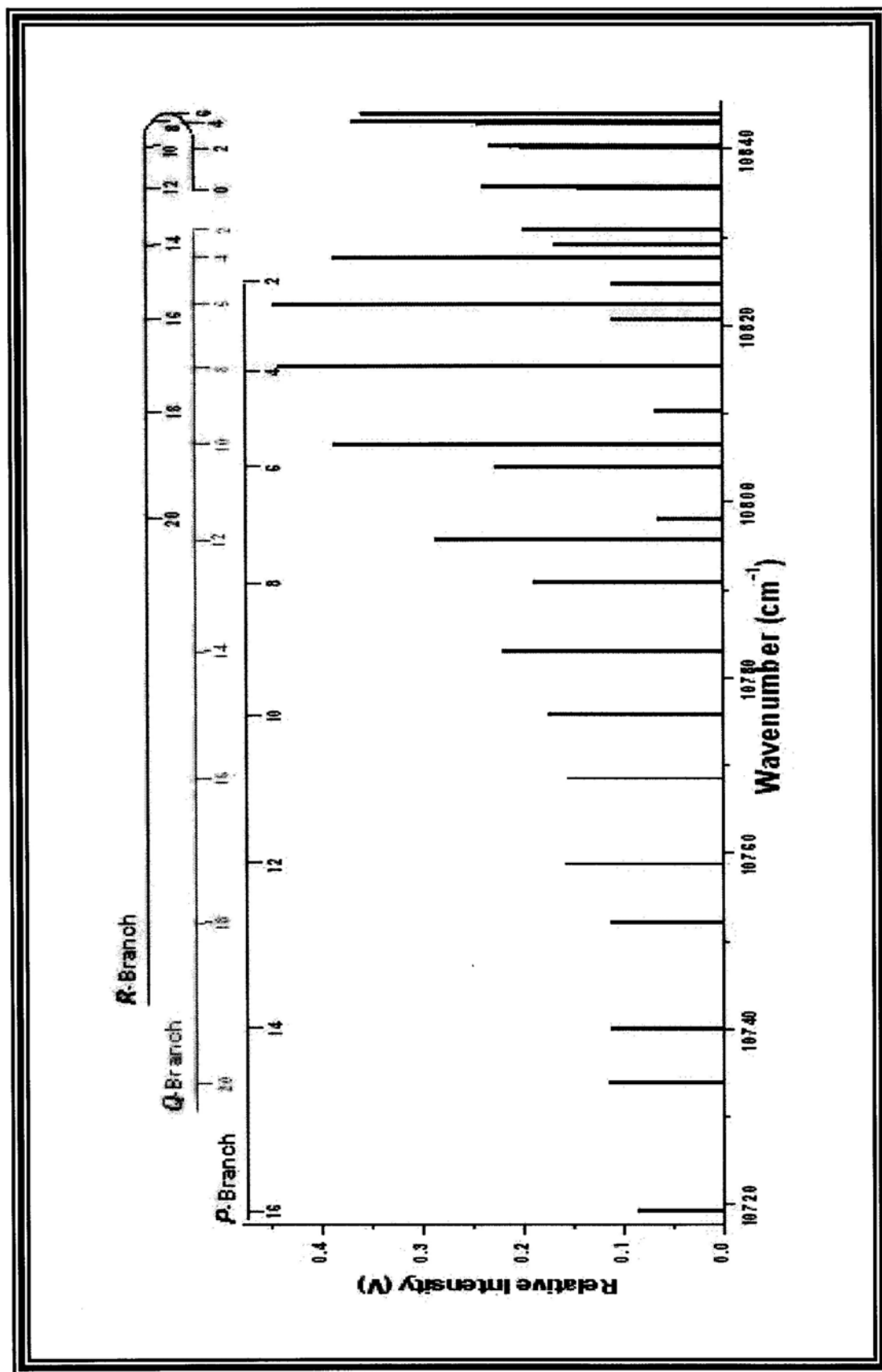

79

Fig. 30 Stick spectrum of (3-1) band in C₂ Phillips system with relative intensity.
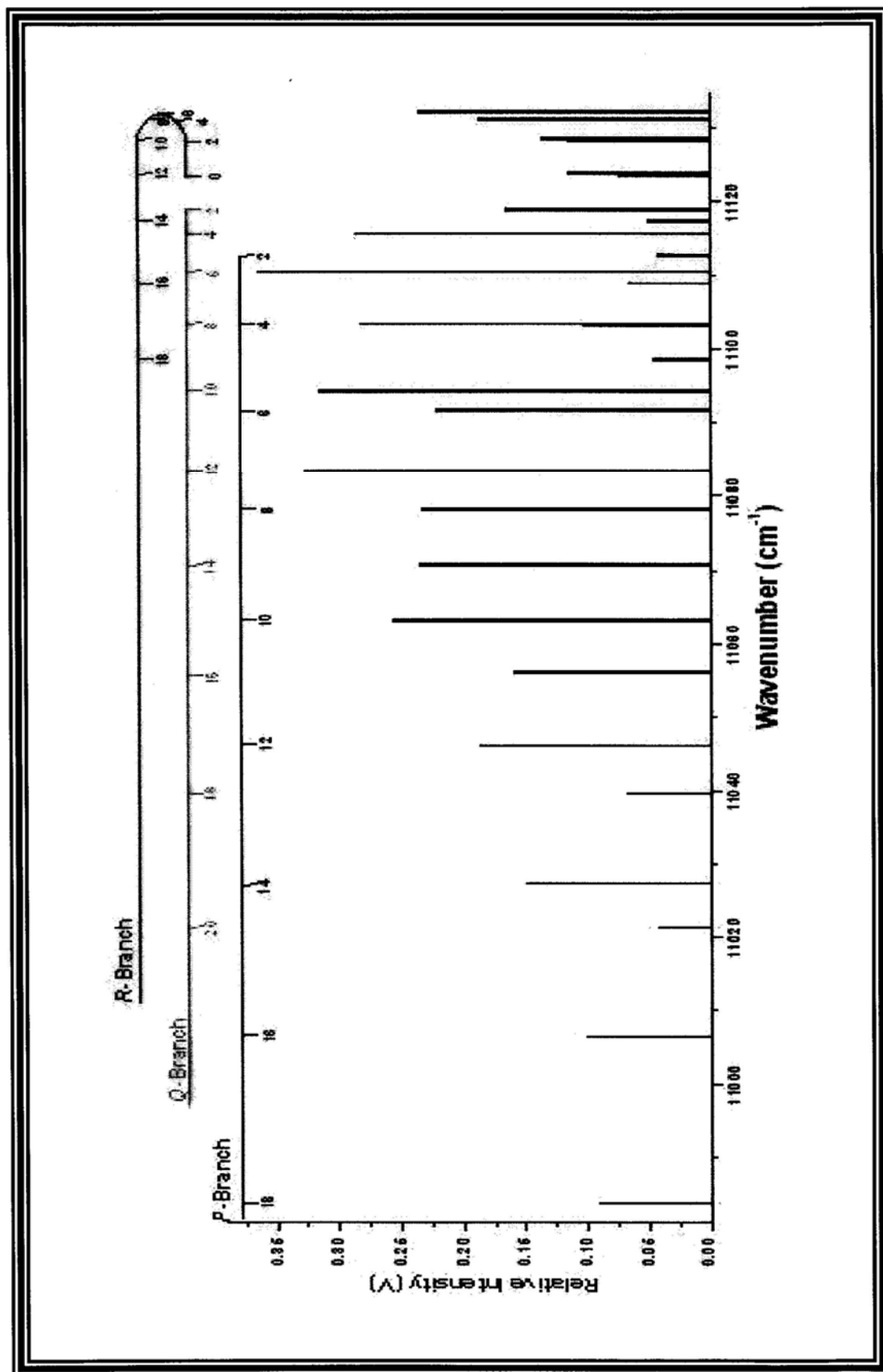
Fig. 31   Stick spectrum of (2-0) band in C_2 Phillips system with relative intensity.
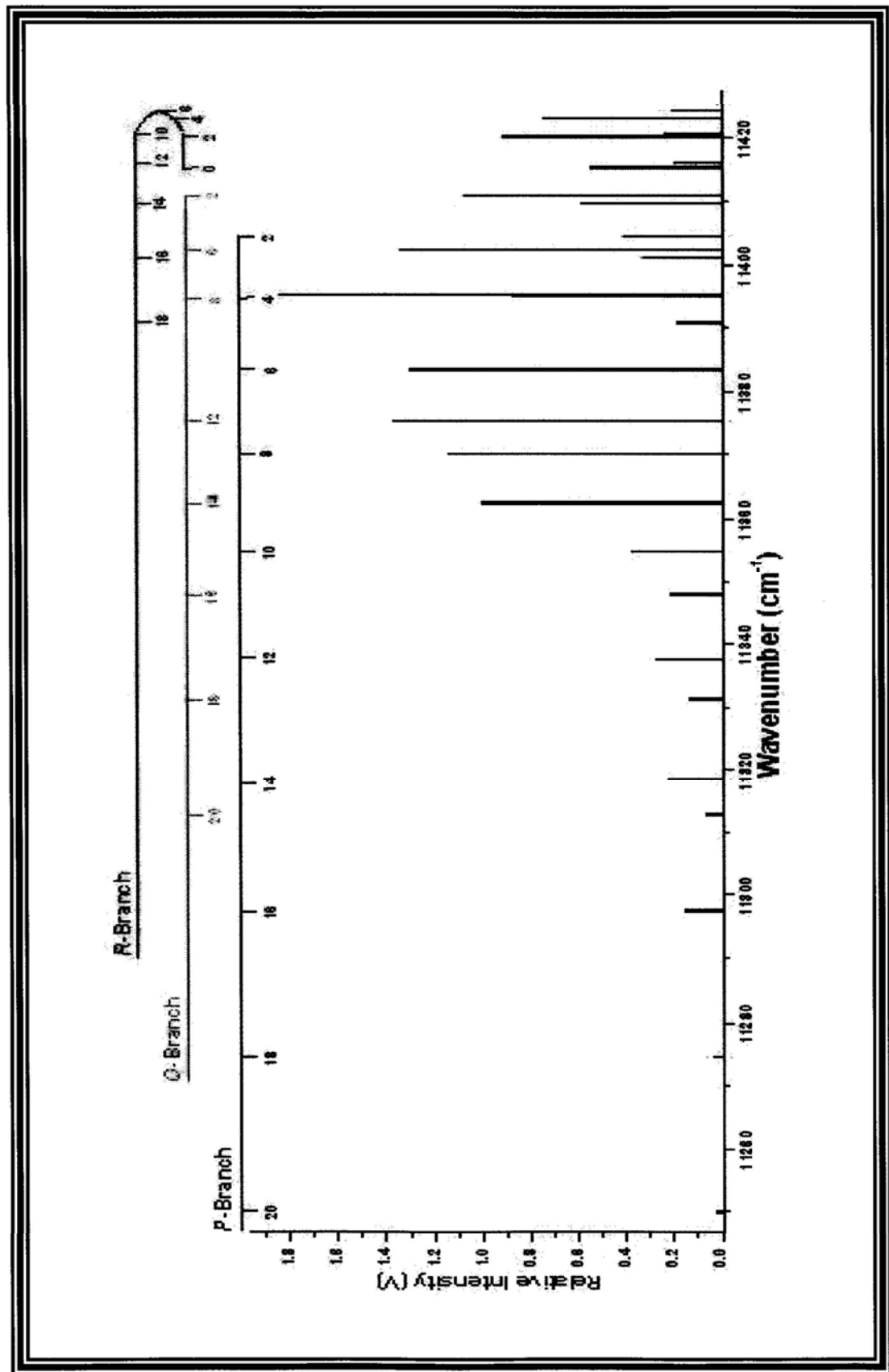
Fig. 32   Stick spectrum of (6-3) band in C_2 Phillips system with relative intensity.
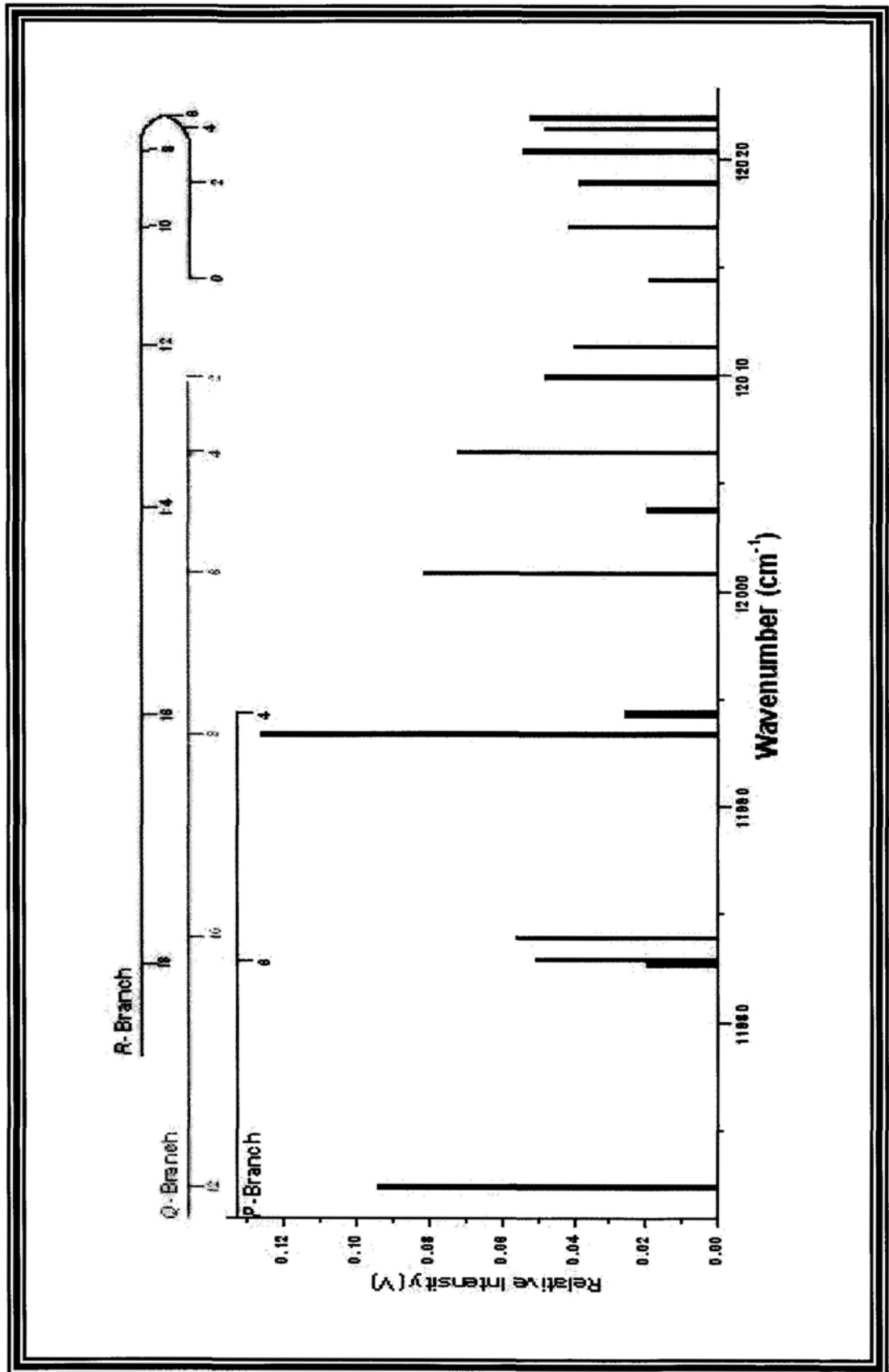
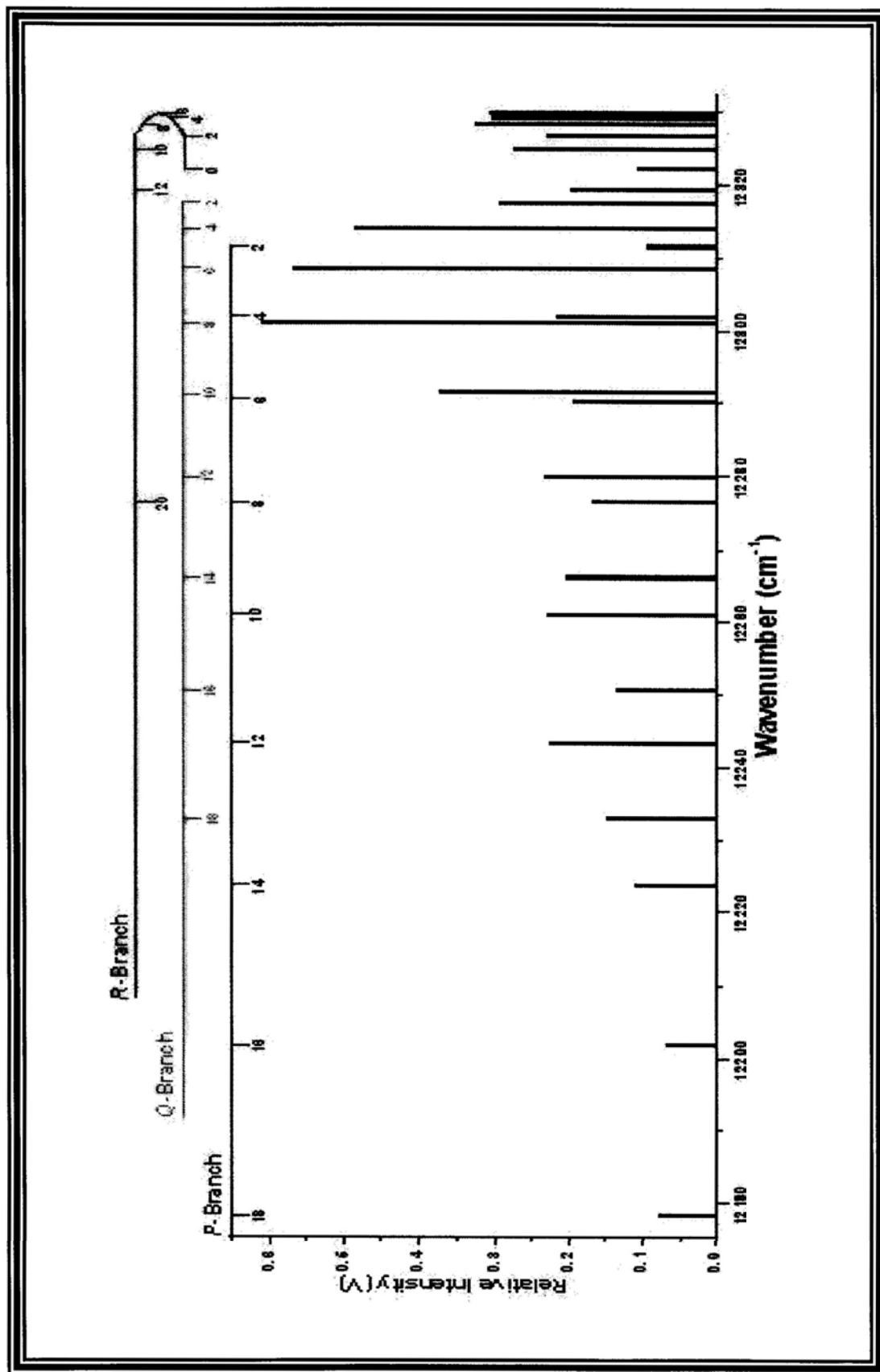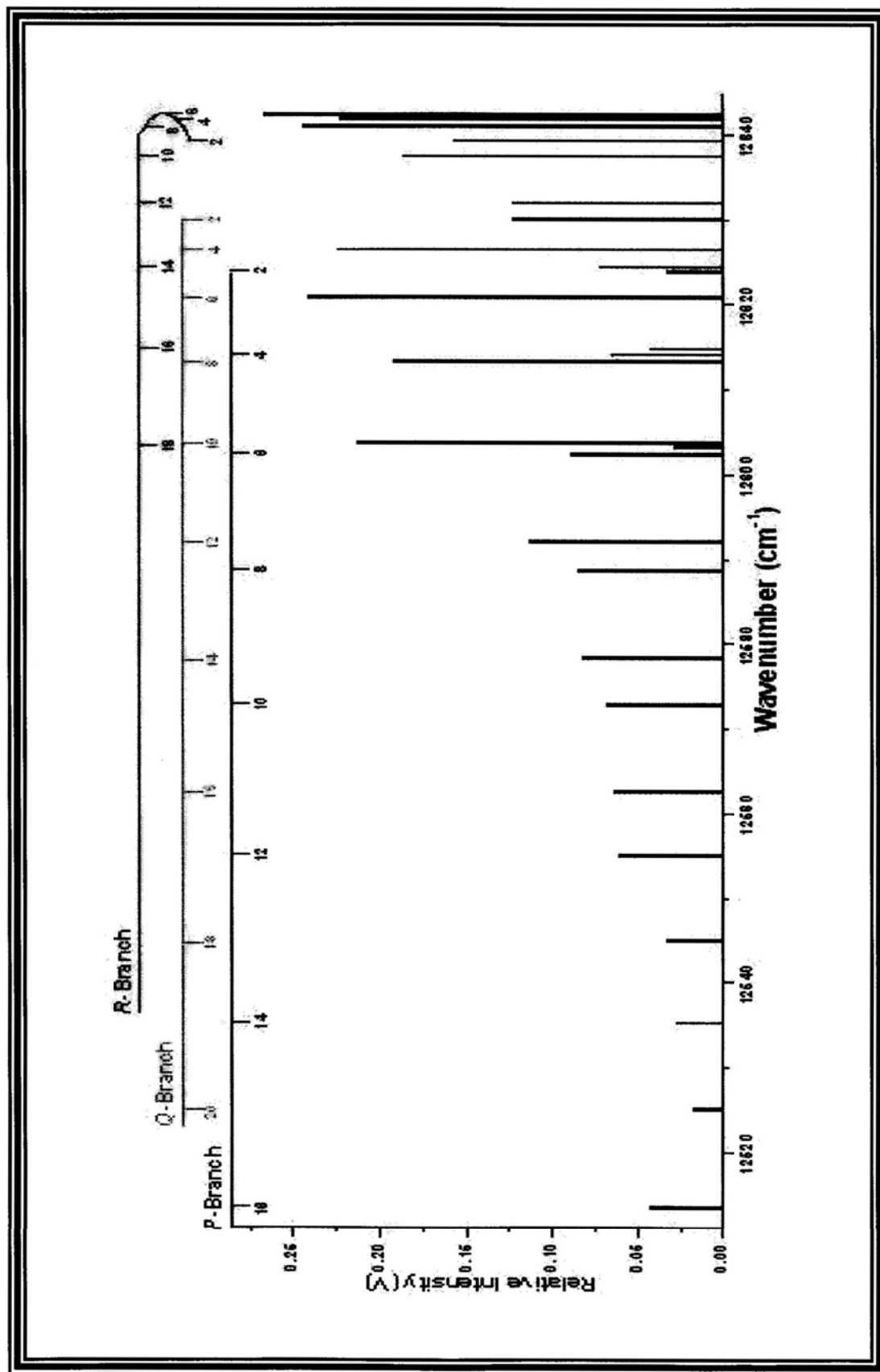Fig. 33   Stick spectrum of (5-2) band in C₂ Phillips system with relative intensity.

Fig. 34   Stick spectrum of (4-1) band in C$_2$ Phillips system with relative intensity.

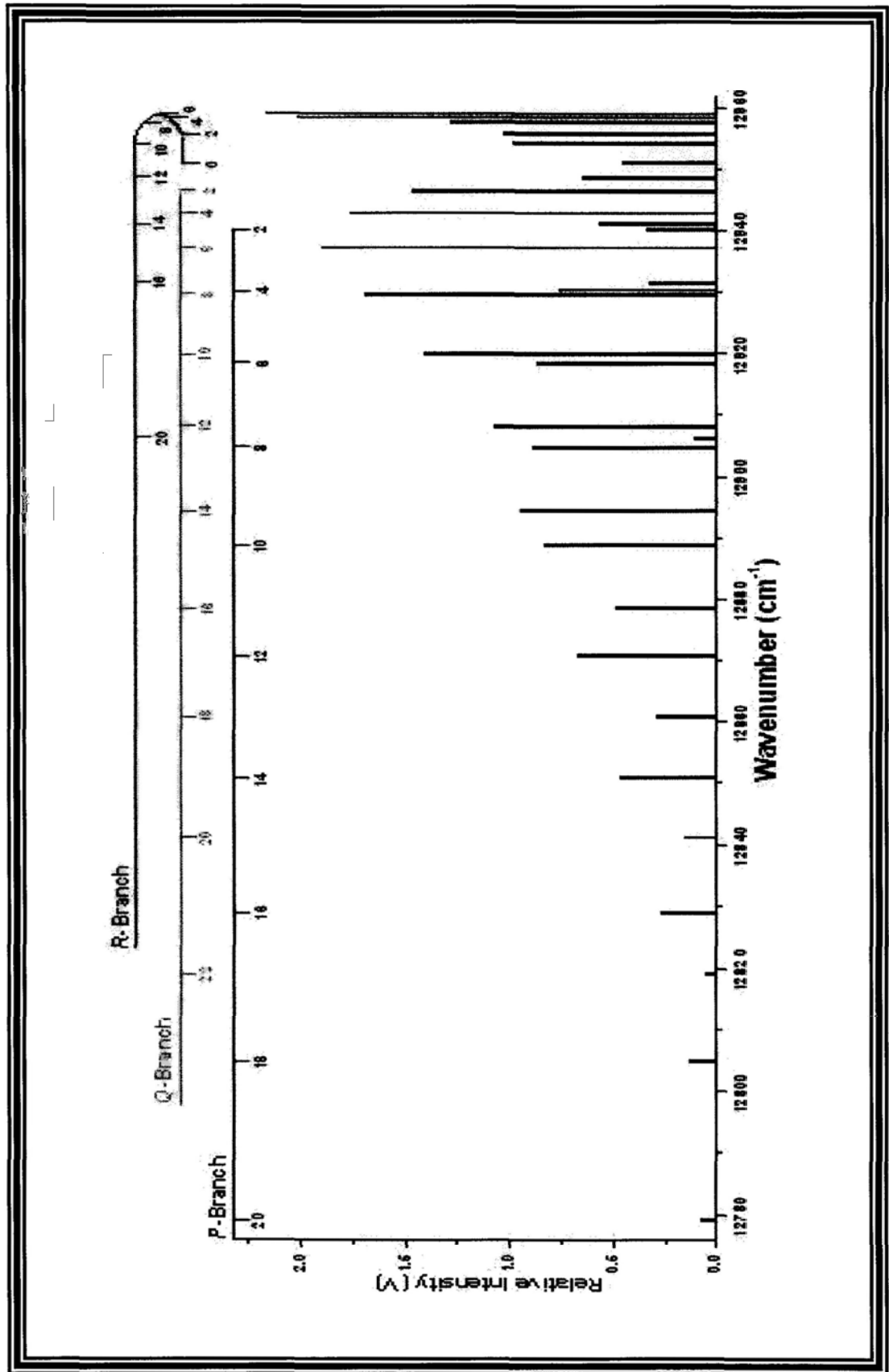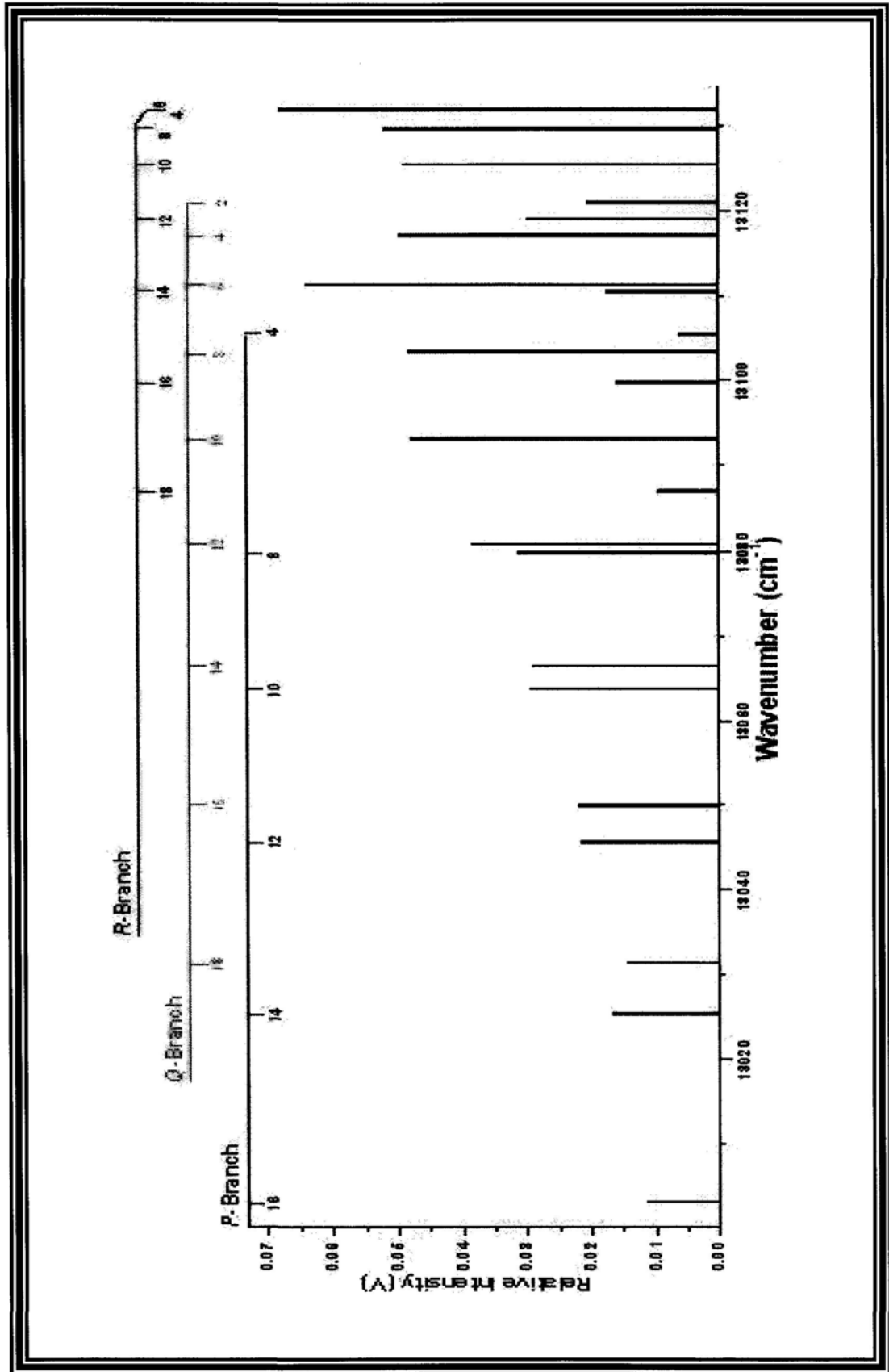Fig. 35   Stick spectrum of (3-0) band in C$_2$ Phillips system with relative intensity.

Fig. 36   Stick spectrum of (8-4) band in C_2 Phillips system with relative intensity.

86

Fig. 37 Stick spectrum of (7-3) band in C$_2$ Phillips system with relative intensity.
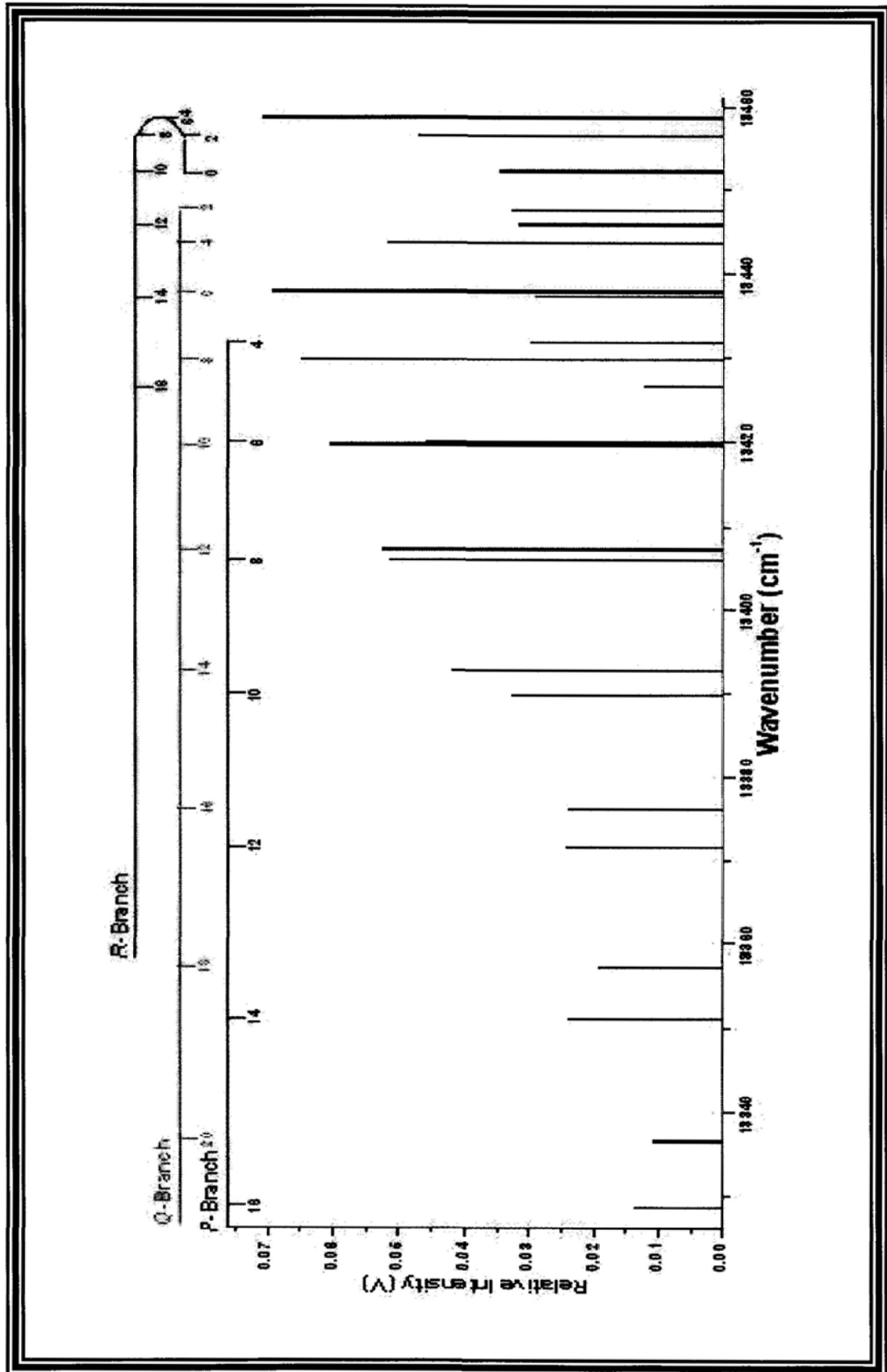
Fig. 38   Stick spectrum of (6-2) band in C_2 Phillips system with relative intensity.
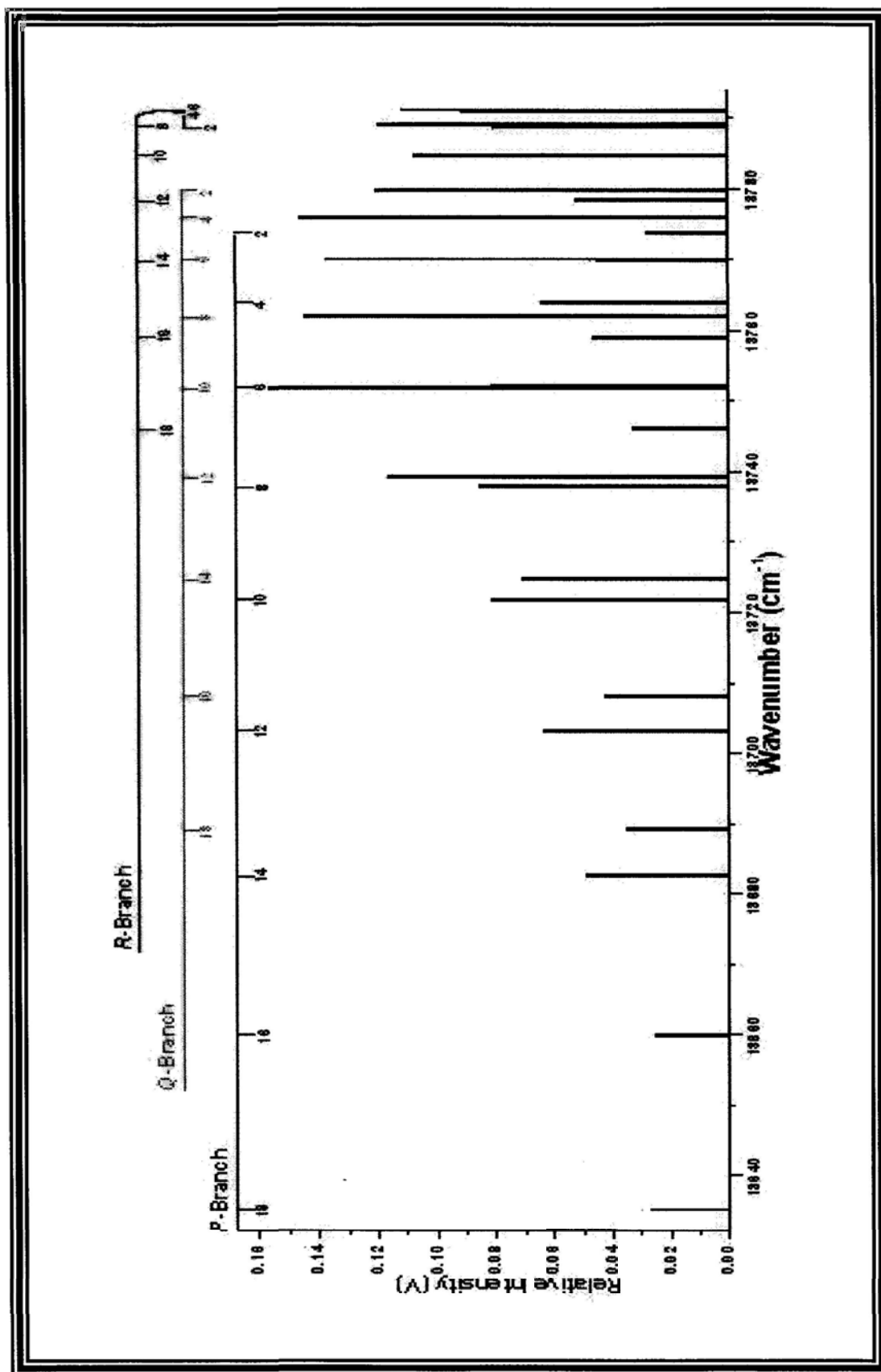
Fig. 39   Stick spectrum of (5-1) band in C₂ Phillips system with relative intensity.
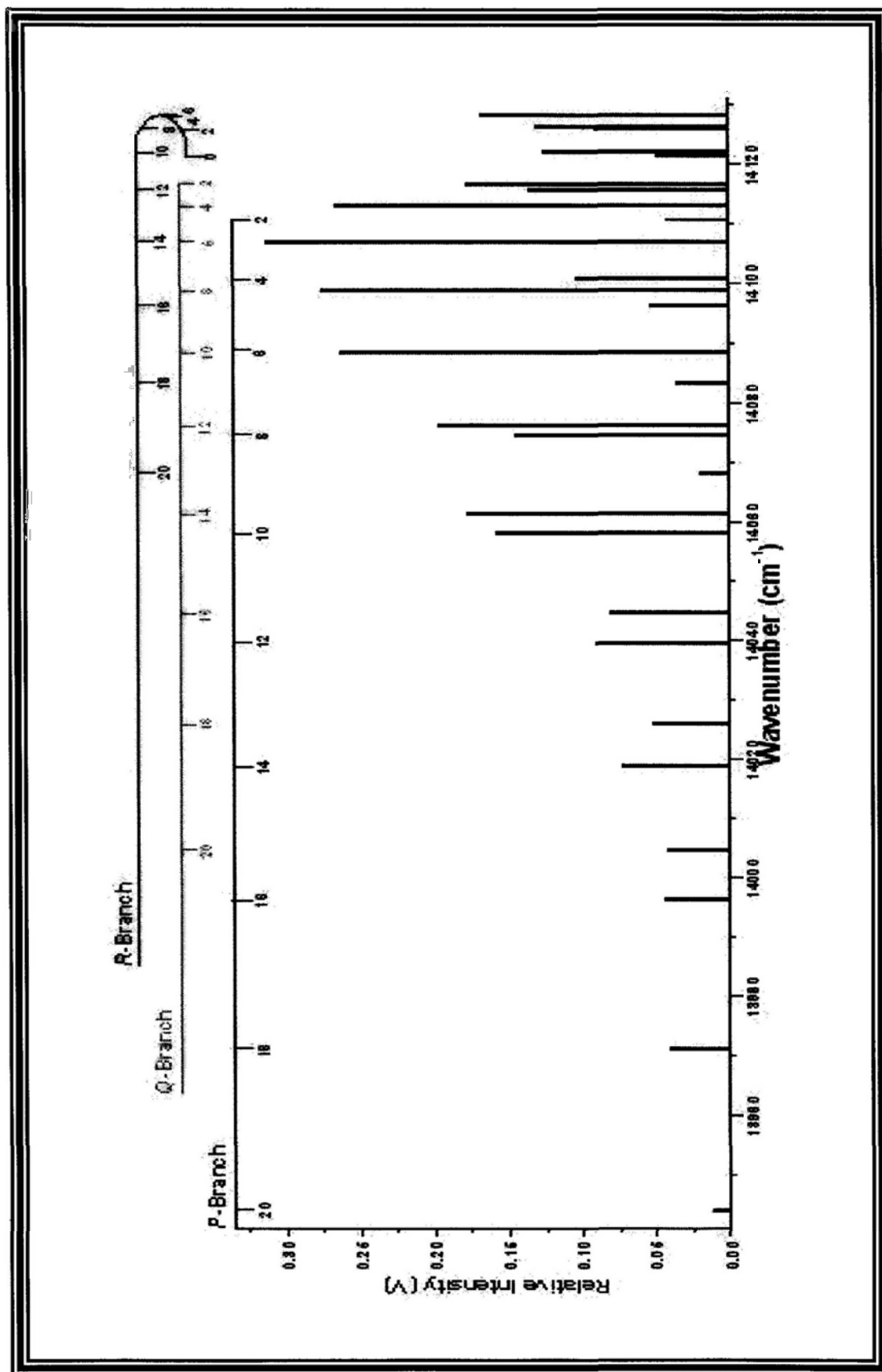
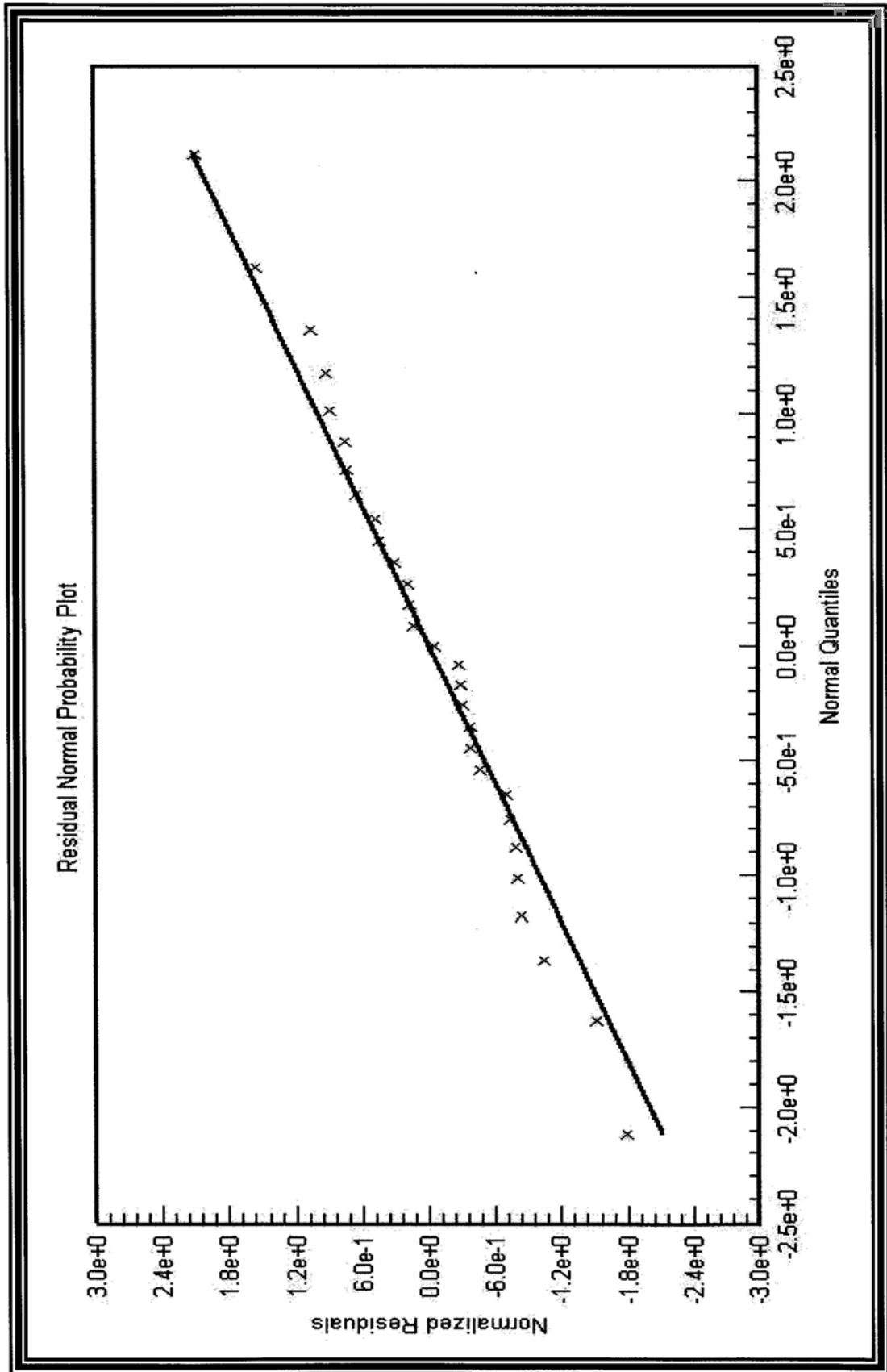Fig. 40   Residual normal probability plot of (4-2) band in C_2 Phillips system.

Fig. 41   Residual normal probability plot of (3-1) band in C_2 Phillips system.

Fig. 42   Residual normal probability plot of (2-0) band in C_2 Phillips system.

Residual Normal Probability Plot

Normal Quantiles

Normalized Residuals

Fig. 43 Residual normal probability plot of (6-3) band in C_2 Phillips system.

Fig. 44   Residual normal probability plot of (5-2) band in C_2 Phillips system.

Residual Normal Probability Plot

Normalized Residuals

Normal Quantiles

Fig. 45   Residual normal probability plot of (4-1) band in C_2 Phillips system.

Fig. 46   Residual normal probability plot of (3-0) band in C_2 Phillips system.
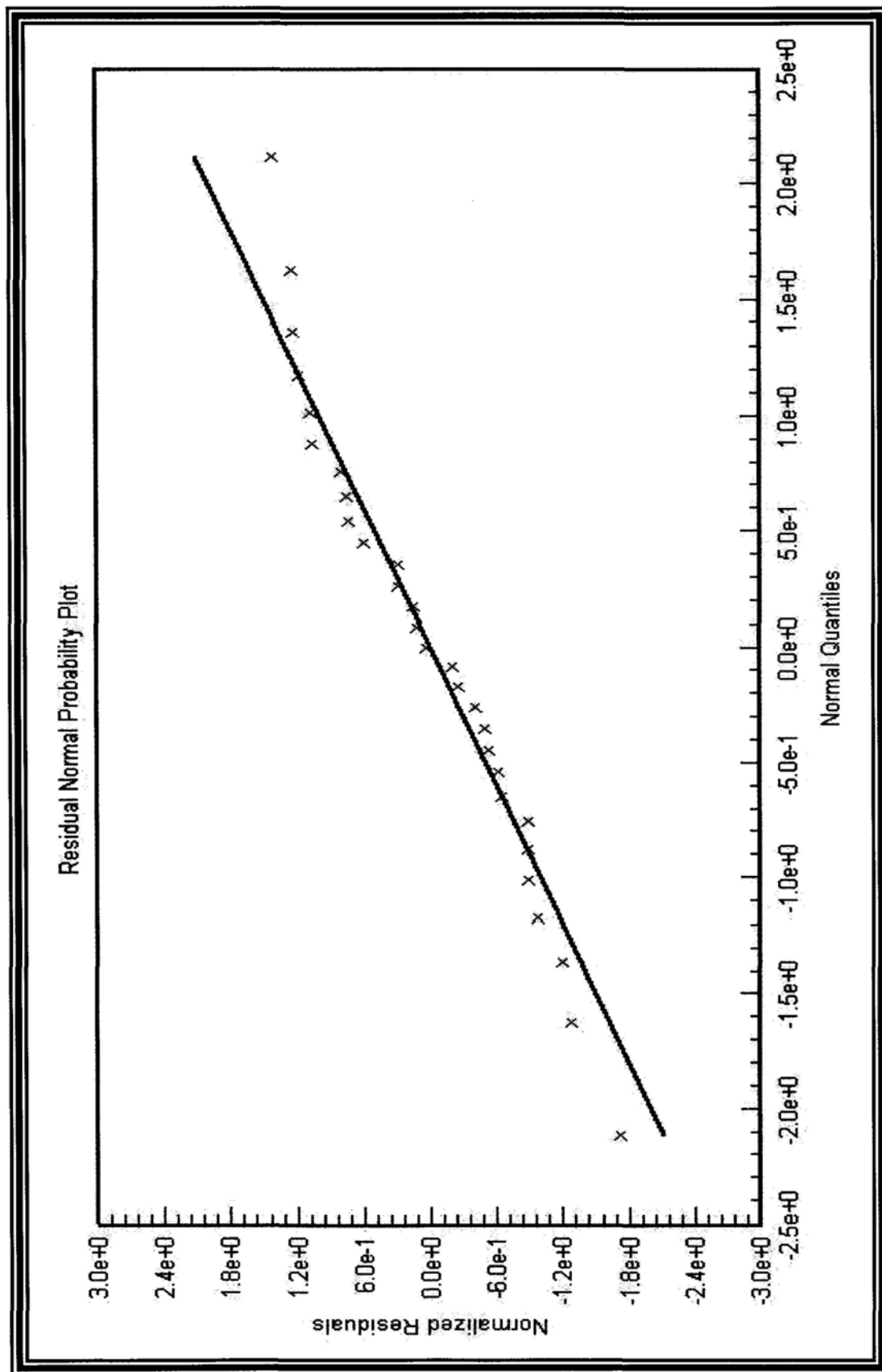
Fig. 47   Residual normal probability plot of (8-4) band in C_2 Phillips system.

Fig. 48   Residual normal probability plot of (7-3) band in C_2 Phillips system.
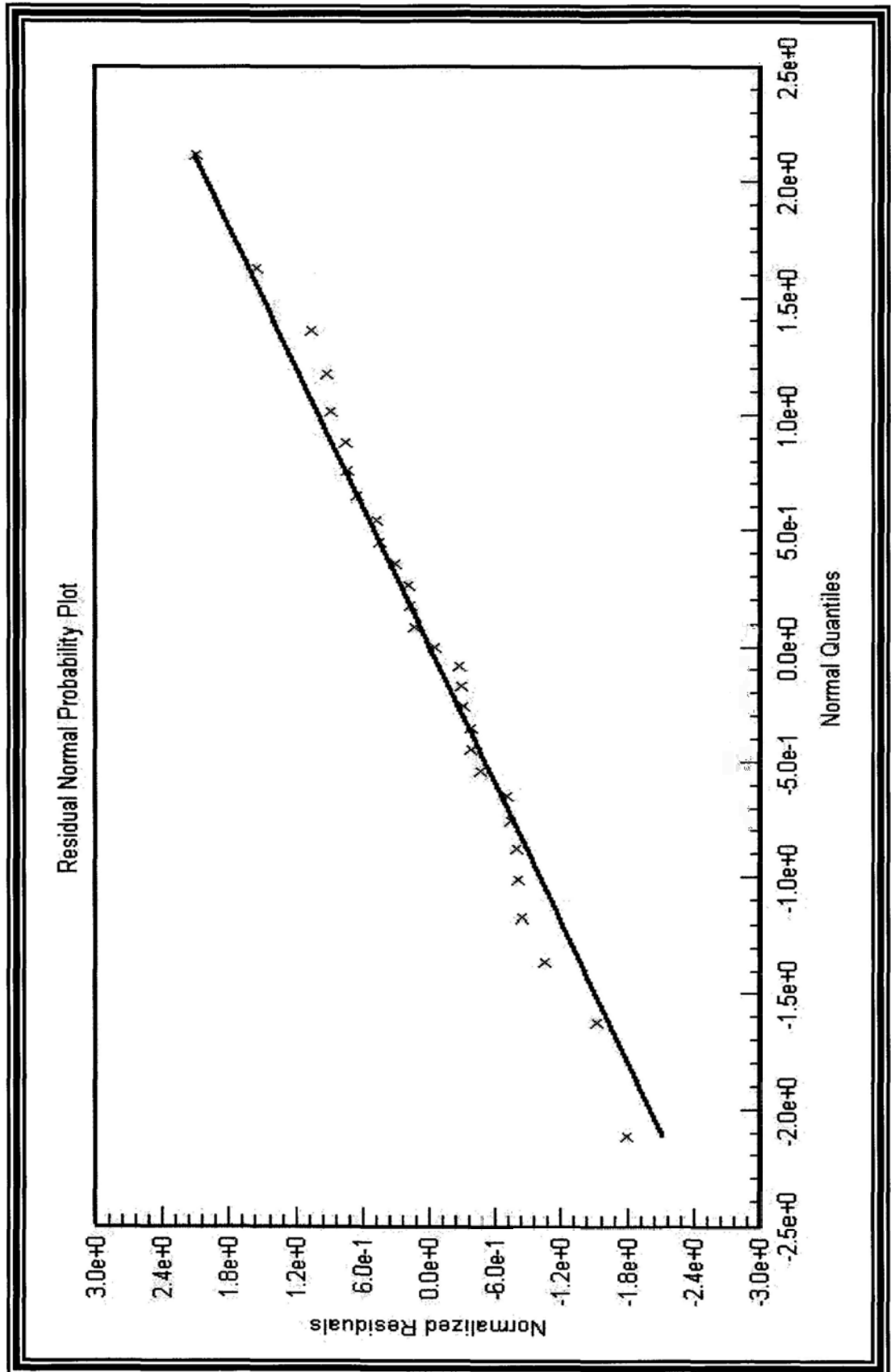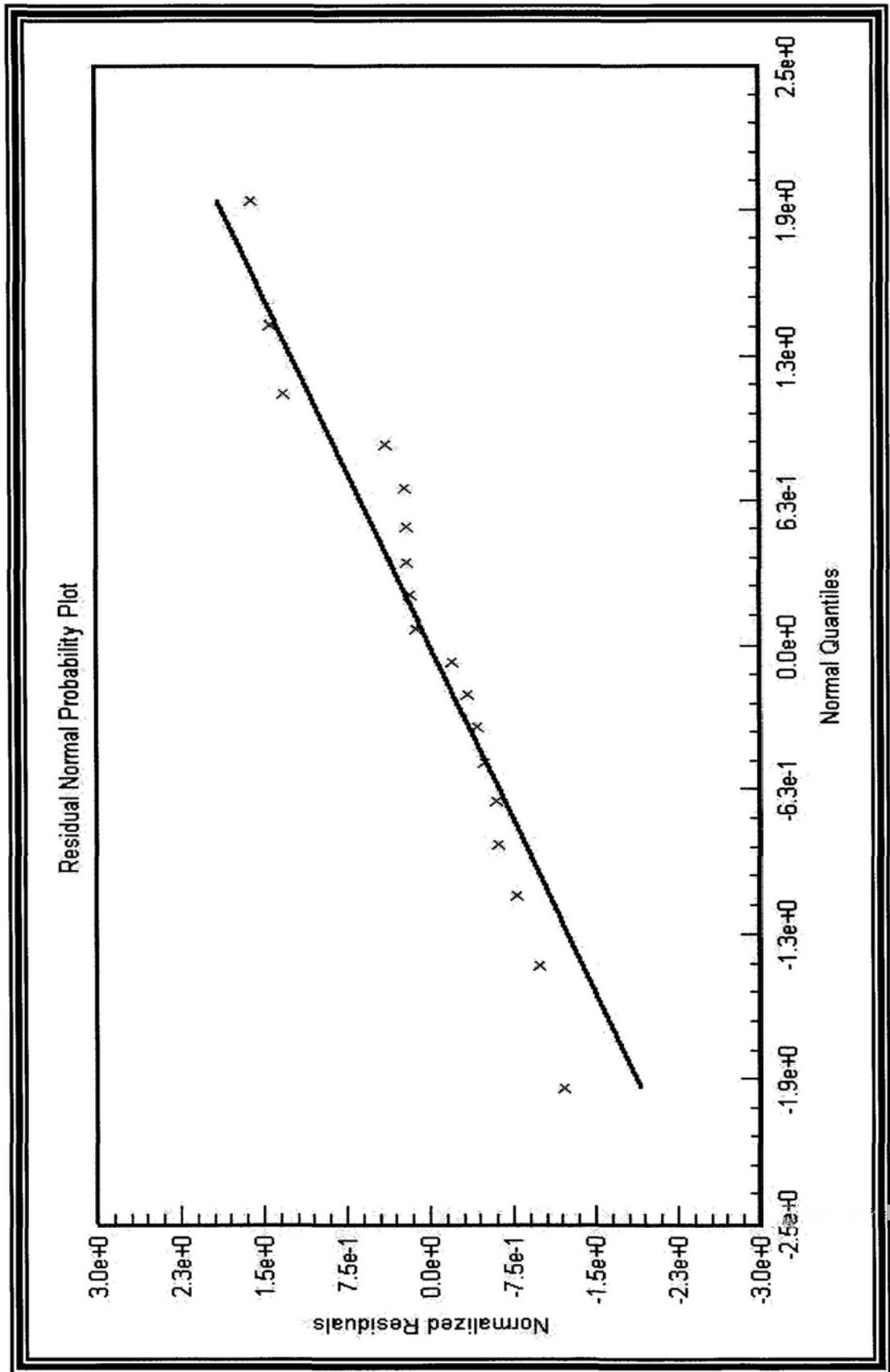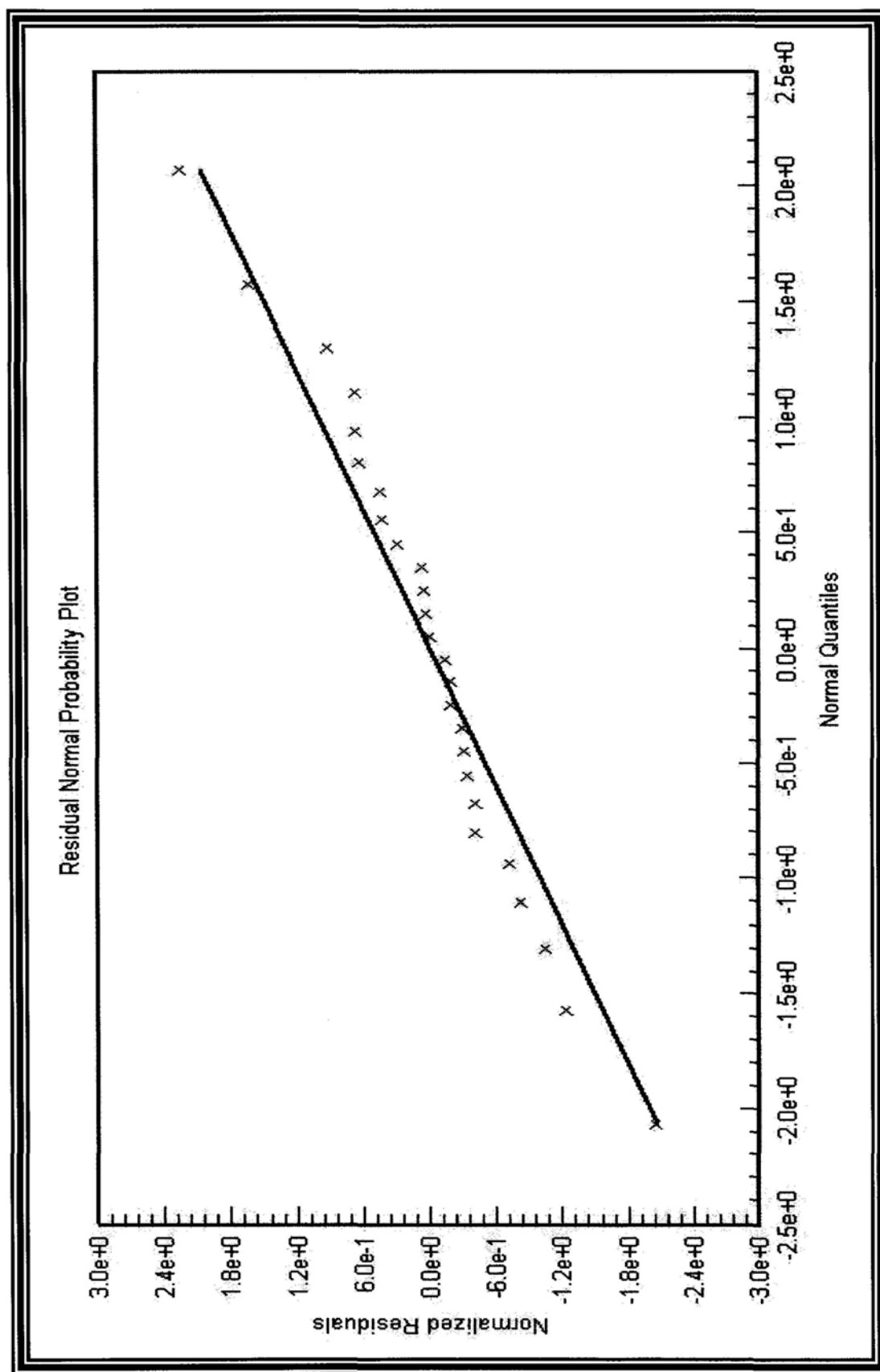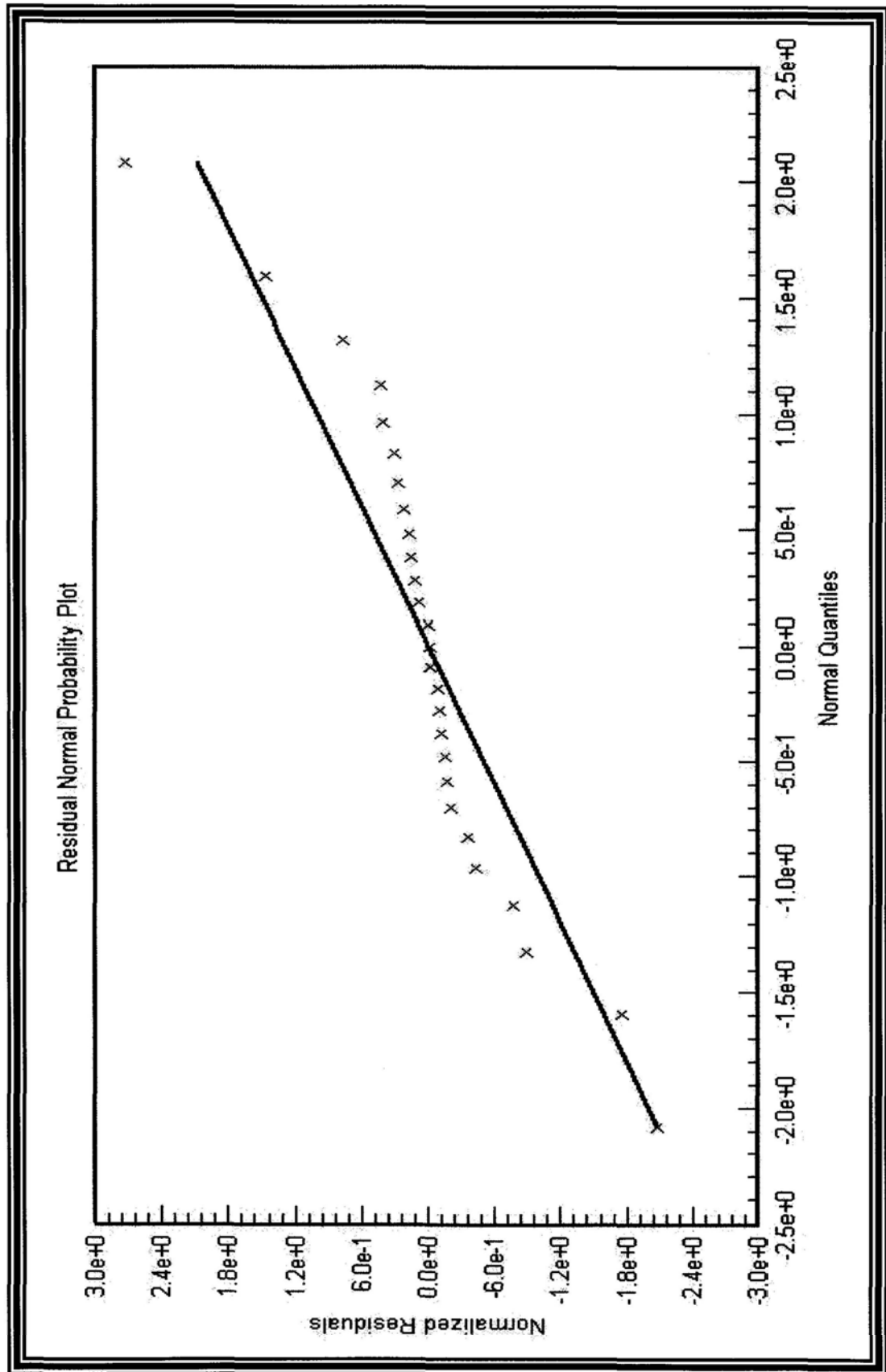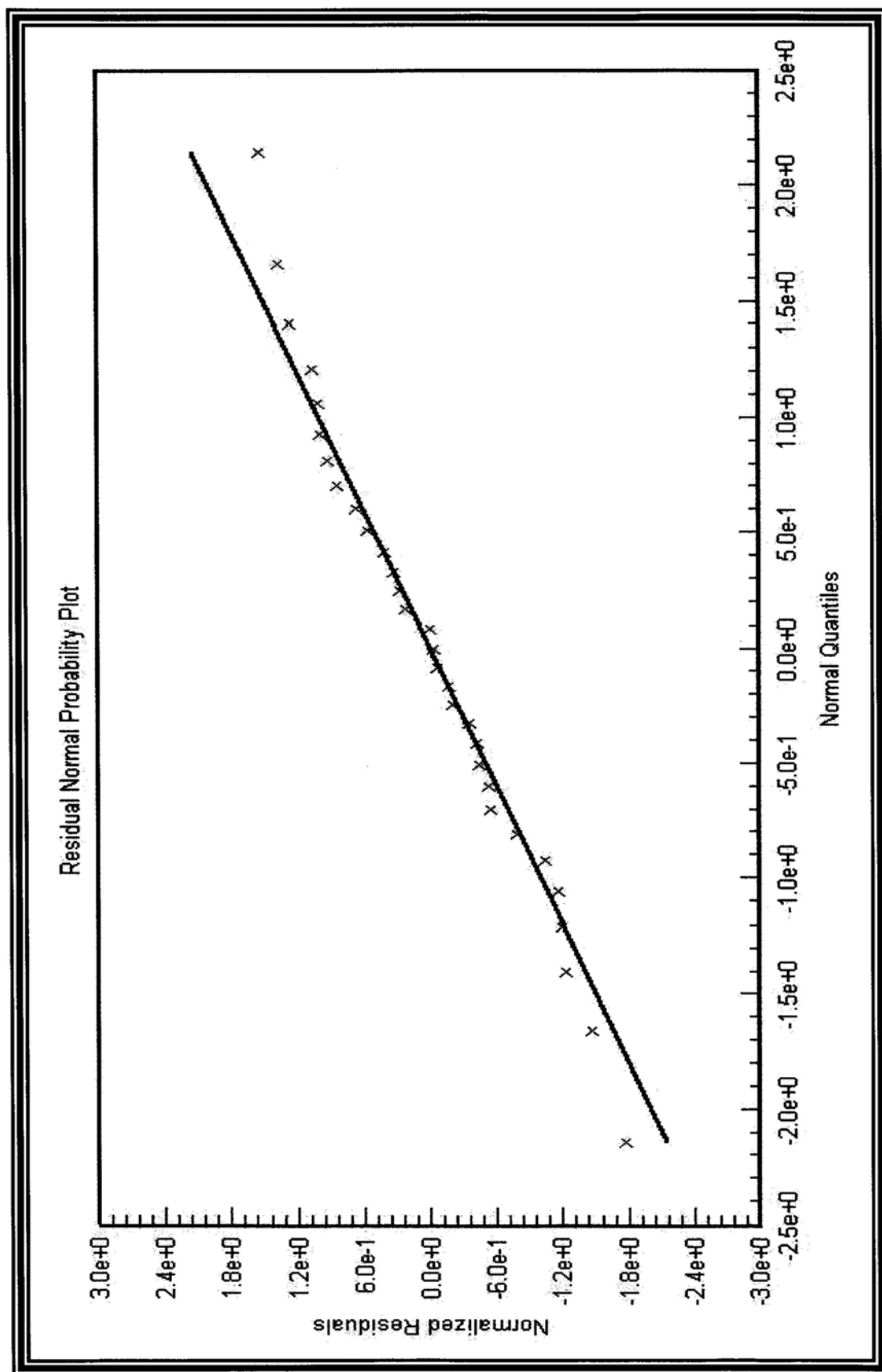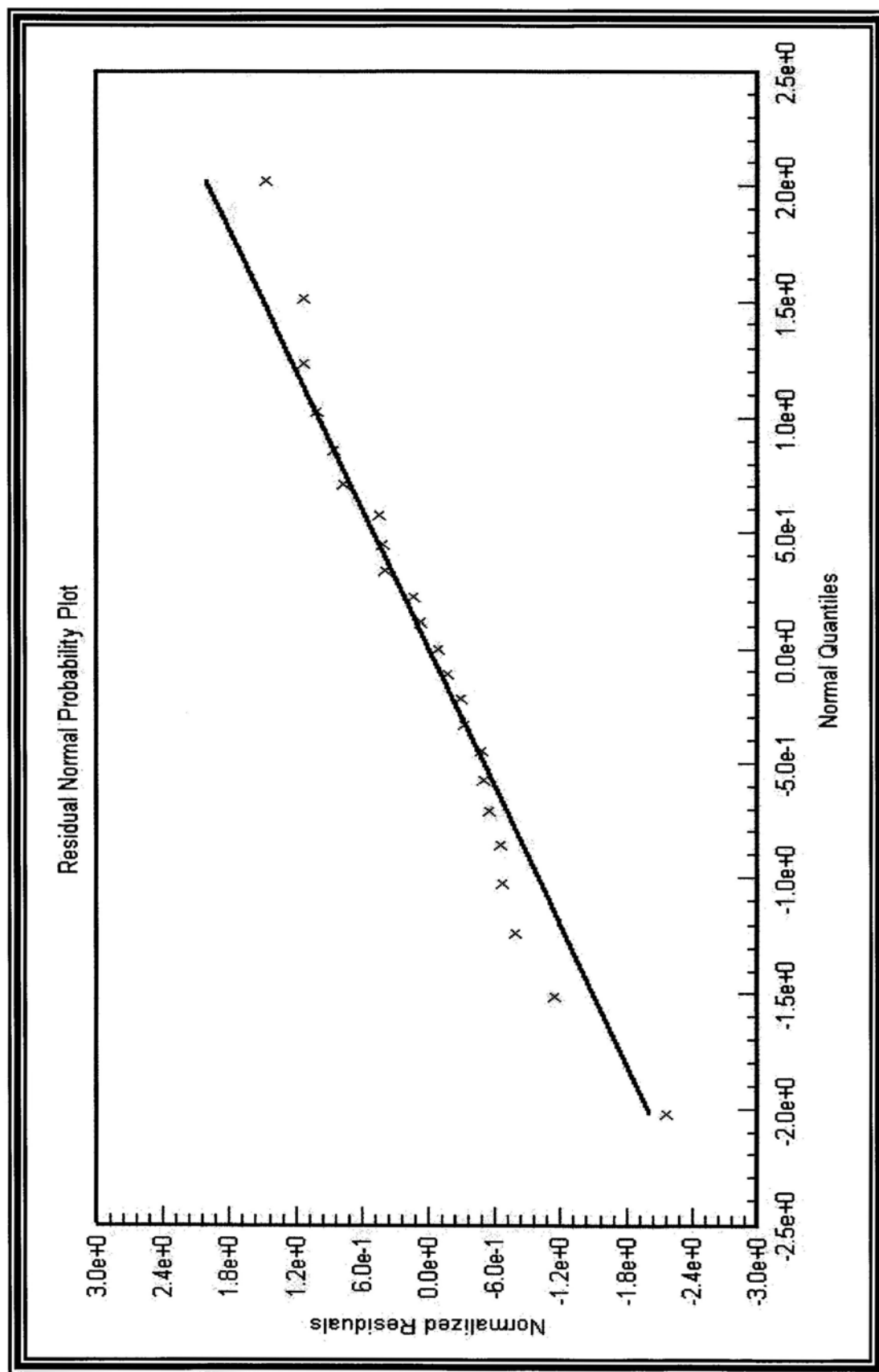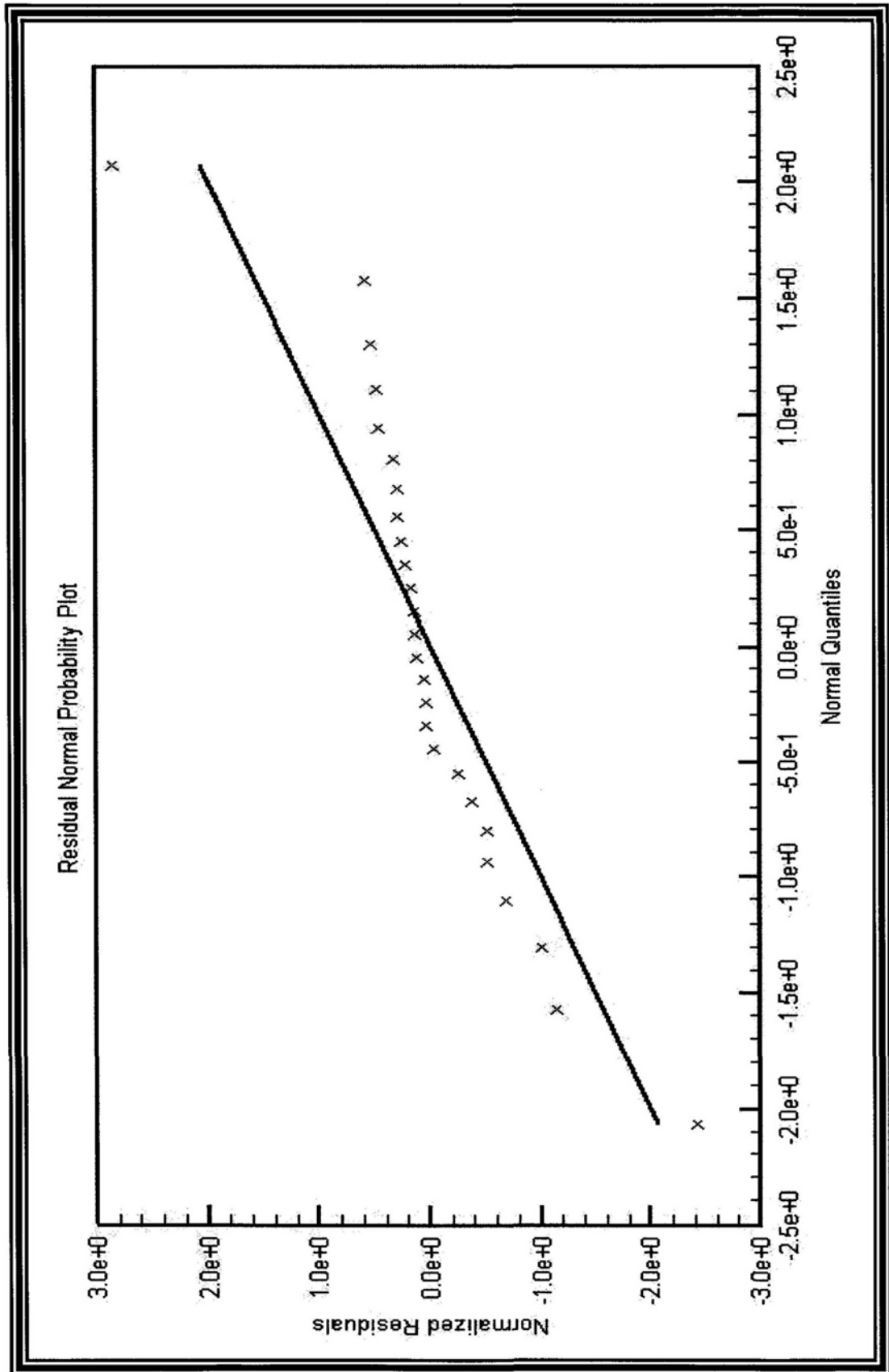

98

Fig. 49   Residual normal probability plot of (6-2) band in C_2 Phillips system.

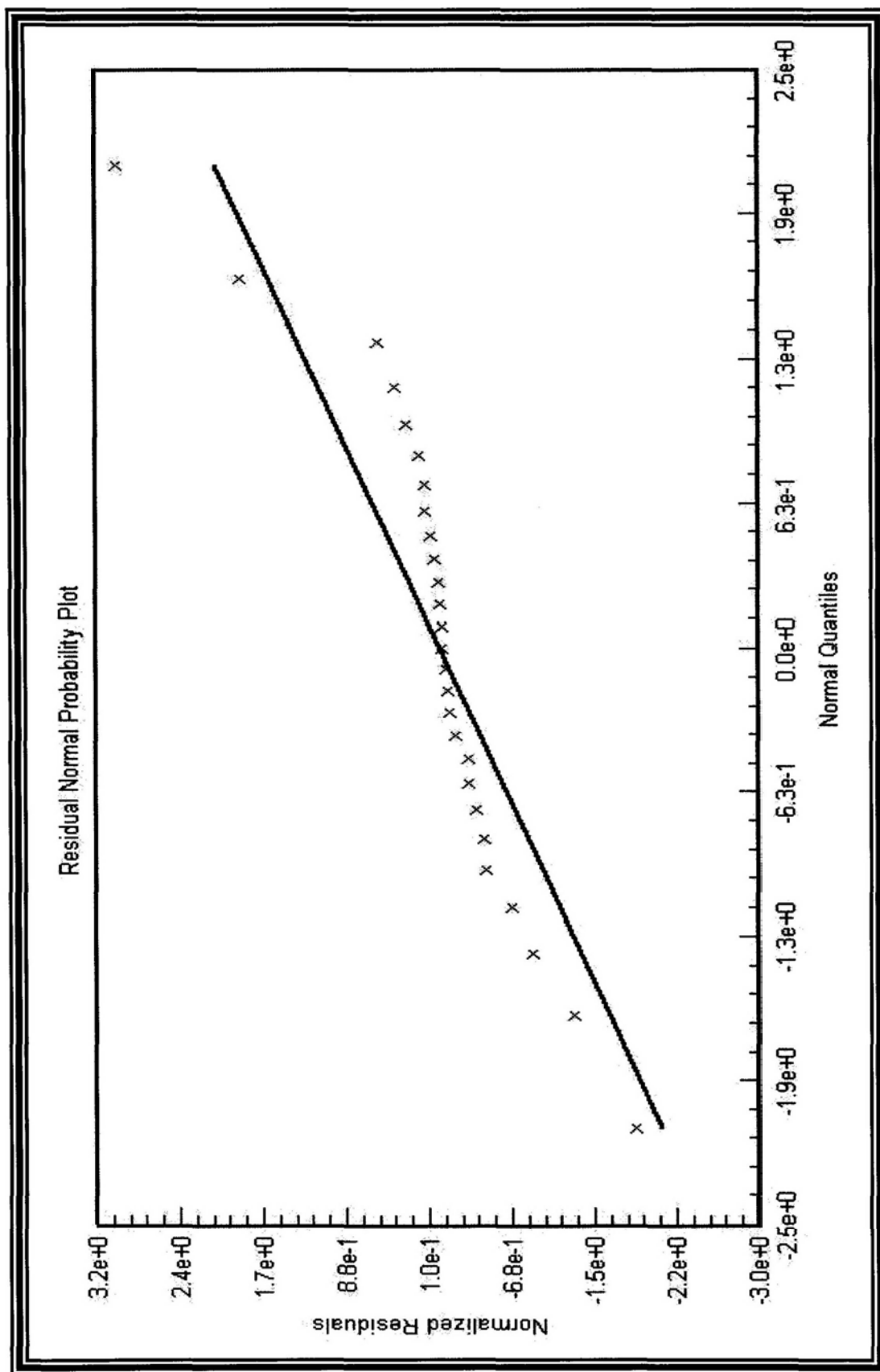Residual Normal Probability Plot

99

Fig. 50   Residual normal probability plot of (5-1) band in C_2 Phillips system.
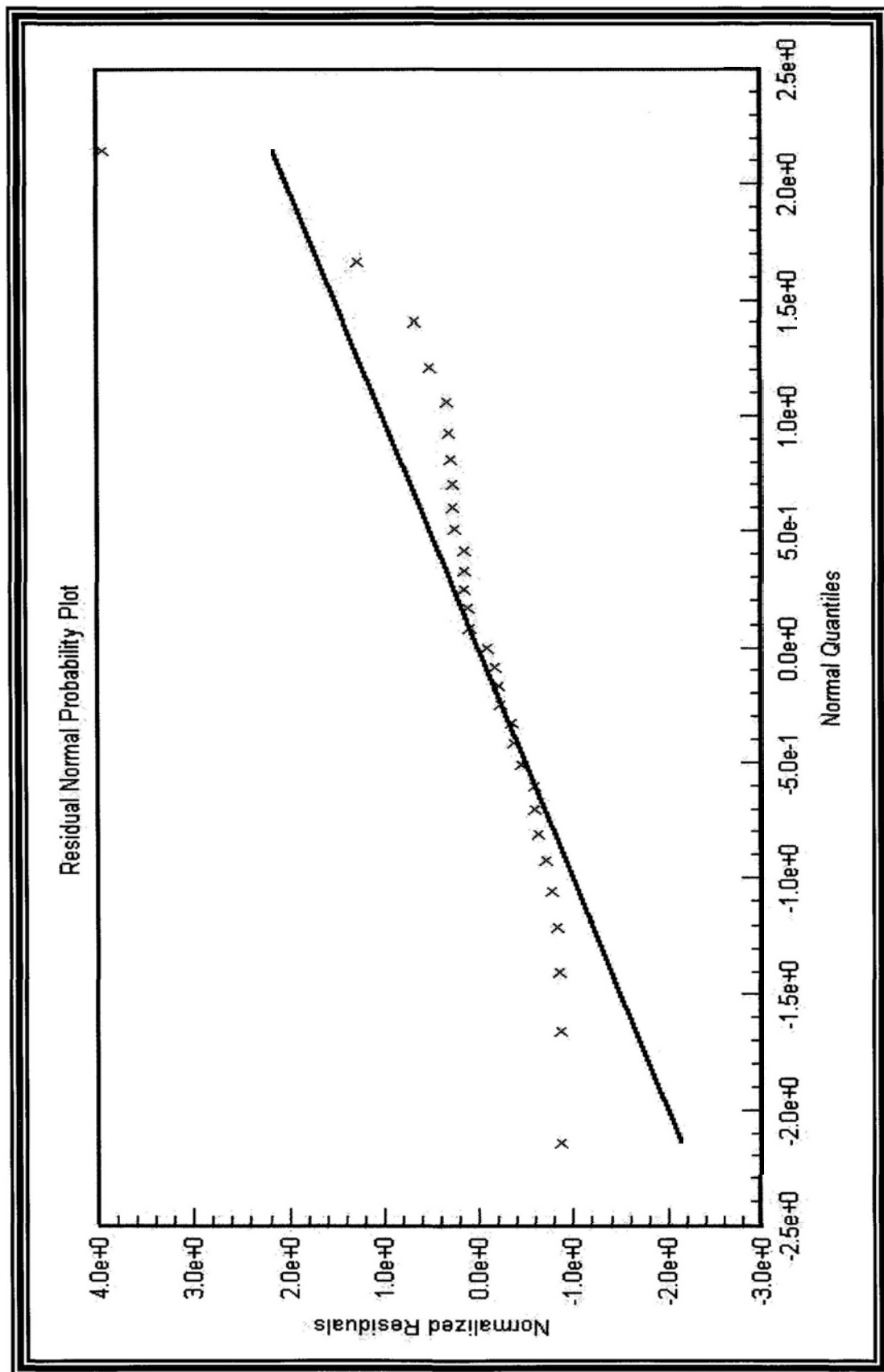

100

Fig. 50 which is expected to be perturbed due to the great slope change. In fact, Ballik and Ramsay[49] has pointed out that the upper electronic state, $A^1\Pi_u$ state of the Phillips system, is perturbed by the $A'''^3\Sigma_u^+$ state. In the vibrational levels, $v' = 4, 5$ and 6, perturbations to the rotational levels with $J > 18$ has been observed.

Although the band-specific fits give satisfactory results, the vibronic bands observed in our experiments involved levels with $v'' < 4$. For a better fitting result, we combined our data with the twelve bands (over 500 transitions) observed by Douay et al.[53] for determining a set of molecular constants using least-squares fitting. These vibronic bands involved high v transitions in both lower and upper electronic states.

We therefore carry out a global fit in which all bands are simultaneously fitted to a Hamiltonian[52] expressed in equilibrium molecular constants:

$$\begin{aligned}
\bar{v} = & T_e + \omega_e'(v'+\tfrac{1}{2}) - \omega_e\chi_e'(v'+\tfrac{1}{2})^2 + \omega_e y_e'(v'+\tfrac{1}{2})^3 - \omega_e z_e'(v'+\tfrac{1}{2})^4 + \omega_e a_e'(v'+\tfrac{1}{2})^5 \\
& - \omega_e''(v''+\tfrac{1}{2}) + \omega_e\chi_e''(v''+\tfrac{1}{2})^2 - \omega_e y_e''(v''+\tfrac{1}{2})^3 + \omega_e z_e''(v''+\tfrac{1}{2})^4 - \omega_e a_e''(v''+\tfrac{1}{2})^5 \\
& + \left[B_e' - \alpha_e'(v'+\tfrac{1}{2}) + \gamma_e'(v'+\tfrac{1}{2})^2 + \delta_e'(v'+\tfrac{1}{2})^3\right]J'(J'+1) \\
& - \left[B_e'' - \alpha_e''(v''+\tfrac{1}{2}) + \gamma_e''(v''+\tfrac{1}{2})^2 + \delta_e''(v'+\tfrac{1}{2})^3\right]J''(J''+1) \\
& - \left[D_e' + \beta_e'(v'+\tfrac{1}{2})\right][J'(J'+1)]^2 + \left[D_e'' + \beta_e''(v''+\tfrac{1}{2})\right][J''(J''+1)]^2 \\
& \pm \tfrac{1}{2}\left\{q_{B'}J'(J'+1) - q_{\alpha'}(v'+\tfrac{1}{2})J'(J'+1) + q_{D'}[J'(J'+1)]^2\right\} \qquad \text{in cm}^{-1}
\end{aligned}$$

In order to account accurately for the high vibrational states (v' up to 8 and v'' up to 6) involved, high order anharmonicity constants $\omega_e z_e$ and $\omega_e a_e$ were introduced in the Hamiltonian for least-squares fitting. Most transitions are observed at frequencies within 0.005 cm^{-1} as in the band-specific fits. The new fitted spectroscopic

parameters[57] are listed in TABLE 18. It is seen that the agreements are in general

excellent except for the high order parameters while the fitted values of $\omega_e z_e$ and $\omega_e a_e$

give fairly large uncertainty. However, their inclusion in the fitting can reduce the

residue.

3G Further discussion

Using the observed equilibrium rotational constants, the corresponding bond

lengths r_e in the $X^1\Sigma_g^+$ and $A^1\Pi_u$ states are computed using equation[2]

$$B_e = \frac{\hbar}{4\pi c \mu r_e} \, ,$$

where μ is the reduced mass of C_2. The equilibrium bond lengths were determined to

be 1.24188 Å in the $X^1\Sigma_g^+$ state and 1.31771 Å in the $A^1\Pi_u$ state, respectively. These

values are also consistent with ab $initio$ calculations.[58] When comparing the bond

lengths of C_2 from our experimental results and that of C_2^- by Rehfuss et $al.$[59] (TABLE

19), it is seen that the equilibrium bond lengths are about the same for both species.

According to valence bonding theory, C_2^- [KK$(\sigma_g2s)^2(\sigma_u2s)^2(\pi_u2p)^4(\sigma_u2p)^1$] has one

more bonding electron in the σ_u2p bonding orbital and therefore has a bond order of 2.5

compared to that of 2 for C_2 [KK$(\sigma_g2s)^2(\sigma_u2s)^2(\pi_u2p)^4$]. In contrary to simple

bonding theory, C_2^- exhibits a slightly longer bond length than C_2. Similar phenomenon

has also been observed in the isoelectronic pair CN^+ and CN.

TABLE 18   Equilibrium spectroscopic constants of C_2 obtained from the global fit.

Parameters	$A^1\Pi_u$ state		$X^1\Sigma_g^+$ state	
	This work	Douay et al.	This work	Douay et al.
T_e	8391.4148(29)	8391.4085(46)	0.0	0.0
ω_e	1608.2317(38)	1608.1990(52)	1855.0663(63)	1855.0142(129)
$\omega_e\chi_e$	12.0848(25)	12.0597(27)	13.6007(54)	13.5547(124)
$\omega_e y_e$	-0.00288(72)	-0.010555(39)	-0.1160(20)	-0.1321(50)
$\omega_e z_e \times 10^4$	-9.08(90)	—	12.60(32)	35.7(89)
$\omega_e a_e \times 10^4$	2.74(41)	—	-10.03(19)	-11.16(57)
B_e	1.616608(11)	1.6166275(24)	1.820053(11)	1.820099(37)
α_e	0.0169466(33)	0.0169691(51)	0.0179143(44)	0.018012(63)
$\gamma_e \times 10^4$	-0.4237(95)	-0.334(25)	-0.886(17)	-0.633(286)
$\delta_e \times 10^6$	-0.629(81)	-1.54(33)	-18.38(21)	-20.6(37)
$D_e \times 10^6$	6.5005(63)	6.5086(54)	6.9526(66)	6.9640(124)
$\beta_e \times 10^8$	2.38(13)	2.53(29)	6.75(12)	6.41(69)
Λ-doubling parameters				
$q_B \times 10^4$	-1.971(24)	-1.9676(70)	—	—
$q_\alpha \times 10^6$	-1.34(54)	2.74(34)	—	—
$q_D \times 10^9$	6.1(16)	—	—	—

All values are quoted in cm^{-1} with one standard deviation in the last decimal place shown in parentheses.   The variance of the fit is 0.0045 cm^{-1}.

*   Data obtained from M. Douay, R. Nietmann, and P. F. Bernath, *J. Mol. Spectrosc.* **131**, 250 (1988).

TABLE 19   Comparison between the equilibrium bond lengths (r_e) of C_2^- and C_2.

	$A^1\Pi_u$	$X^1\Sigma_g^+$
C_2	1.31771 Å	1.24188 Å
	$A^2\Pi_u$	$X^2\Sigma_g^+$
$^*C_2^-$	1.30768 Å	1.26831 Å

*   Data obtained from

B. D. Rehfuss, D. J. Liu, B. M. Dinelli, M. F. Jagod, W. C. Ho, M. W. Crofton and T. Oka, *J. Chem. Phys.* **89**, 129 (1988).

Furthermore, the anharmonic force constants f_2, f_3 and f_4 of the vibrational potential

$$V/hc = \frac{1}{2} f_2 q^2 + \frac{1}{3!} f_3 q^3 + \frac{1}{4!} f_4 q^4 + \cdots \ (cm^{-1}) \ ,$$

can be determined using following equations

where $f_2 = \omega_e$,

$$f_3 = -\left[\alpha_e + \frac{6B_e^2}{\omega_e} \right] \left[\frac{\omega_e^3}{2B_e^3} \right]^{1/2} \ ,$$

and $f_4 = -16\omega_e \chi_e + \frac{5f_3^2}{3\omega_e}$.

TABLE 20 lists their numeric values for C_2. In the table, the corresponding values for C_2^- are also listed for comparison. Once again, the extra bonding electron in C_2^- has little effect in the potential although the potential of C_2 appears to be slightly more anharmonic. Both these results demonstrate the limitation of simple valence theory, with which a satisfactory explanation is not offered.

3H Unidentified bands

In addition to the Phillips system of C_2 observed in the CH_4/He plasma, two unidentified vibronic bands have been observed in the 12150 cm^{-1} and 12450 cm^{-1} regions (Fig. 51) with a total of about 100 transitions and 150 transitions, respectively. These two bands exhibit the same discharge chemistry and

TABLE 20 Comparison between the anharmonic force constants between C_2^- and C_2.

C_2	$A\,^1\Pi_u$	$X\,^1\Sigma_g^+$
f_2	1608.2317	1855.0663
f_3	-592.3	-659.3
f_4	170.2	172.4
$^*C_2^-$	$A\,^2\Pi_u$	$X\,^2\Sigma_g^+$
f_2	1666.4	1781.2
f_3	-587.6	-616.8
f_4	172.6	169.2

All values are quoted in cm^{-1}.

* Data obtained from

B. D. Rehfuss, D. J. Liu, B. M. Dinelli, M. F. Jagod, W. C. Ho, M. W. Crofton and T. Oka, *J. Chem. Phys.* **89**, 129 (1988).

Fig. 51 Two unidentified bands at 12150 cm^{-1} (blue one) and 12450 cm^{-1} (red one) during CH$_4$/He gaseous discharge. The corresponding S/N ratio is also magnified.
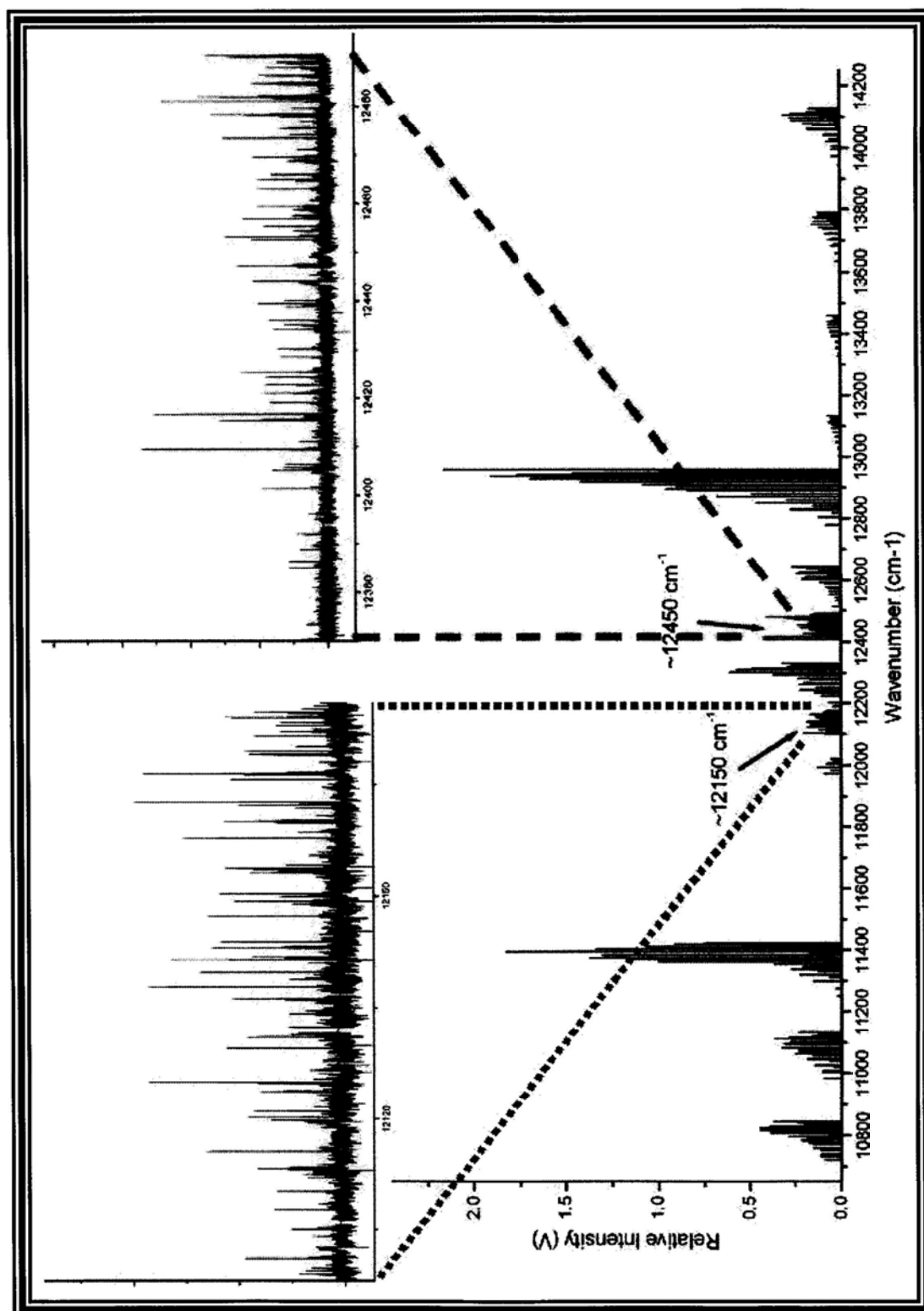
comparable intensities as the vibronic bands of the Phillips system. These two

bands, however, exhibited no apparent spectral pattern with much more dense

transitions. The linewidths of these transitions (shown in Fig. 52 and 53) were

about the same as those for C_2 Phillips system, suggesting the species may have

similar molecular mass as C_2. Moreover, by using CD_4 instead of CH_4 in the

discharges, the absorption frequencies of these two bands (Fig. 54 and Fig. 55)

remain unchanged indicating that these species do not contain any hydrogen atom.

Based on these observations, it is expected that these bands are due to species

with two carbons only. Nevertheless, the frequencies of these two bands do not fit

into any of the known rovibronic systems of C_2, C_2^- and C_2^+. Also, the dense and

complex structure of these two bands suggests that they may be due to states with

high electronic angular momentum. It was proposed by Ballik and Ramsay[49] that

the $A'''^3\Sigma_u^+$ state may have perturbation with high v levels of the $A^1\Pi_u$ state, and it is

plausible that these two bands arises from this perturbation. Further investigation

along this direction is underway for their identification and detailed assignments.

3I Summary

Zero-background absorption laser spectroscopy has been applied to measure the

very weak Phillips system of C_2. A total 11 vibronic bands are measured with

Fig. 52   One of the peak in unidentified bands at 12150 cm^{-1}.   The absorption peak
gives a linewidth of ~0.033 cm^{-1} which is same as linewidth of C$_2$ Phillips band
system transition.
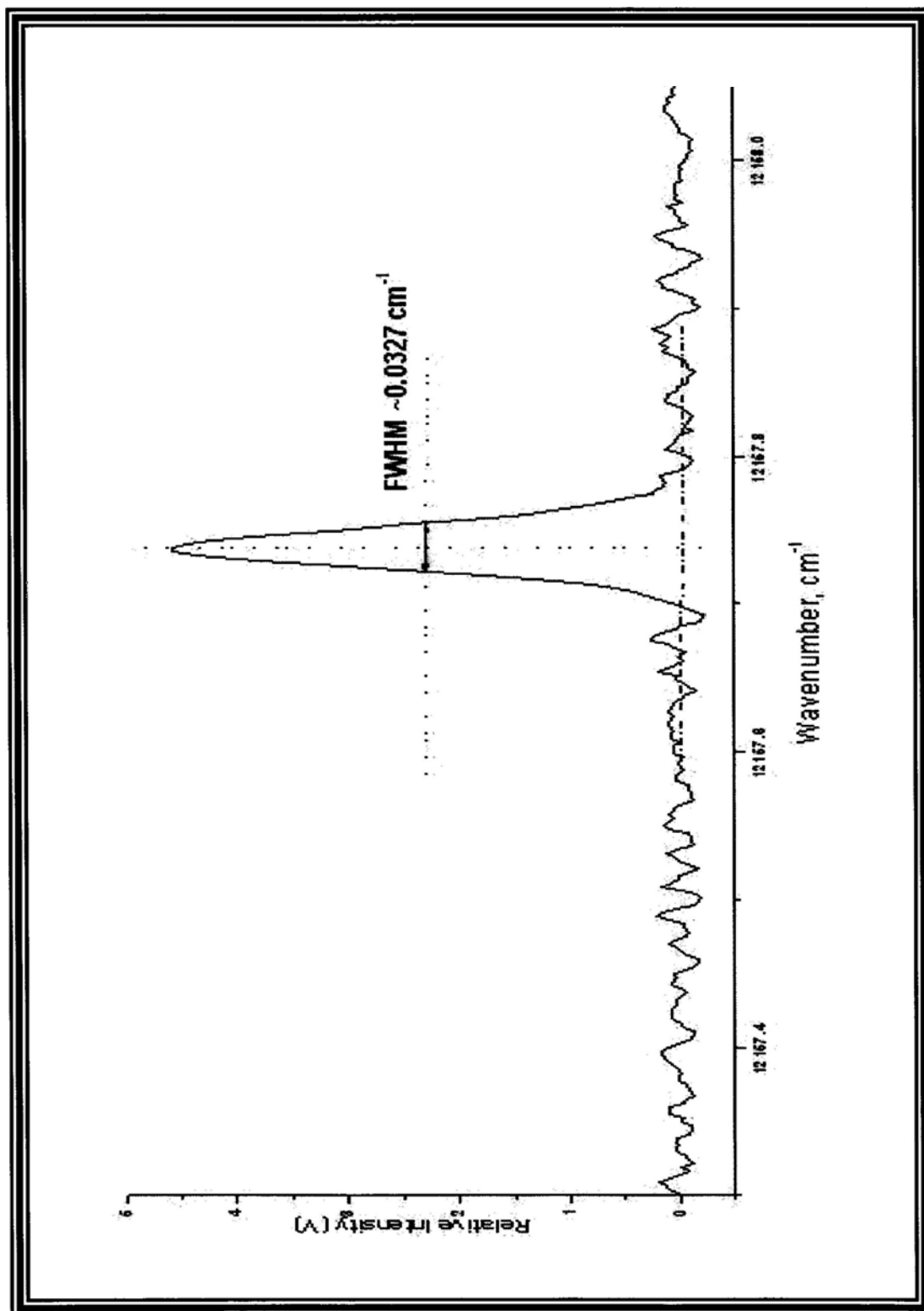
Fig. 53   One of the peak in unidentified bands at 12450 cm^{-1}.   The absorption peak gives a linewidth of ~0.033 cm^{-1} which is same as linewidth of C$_2$ Phillips band system transition.
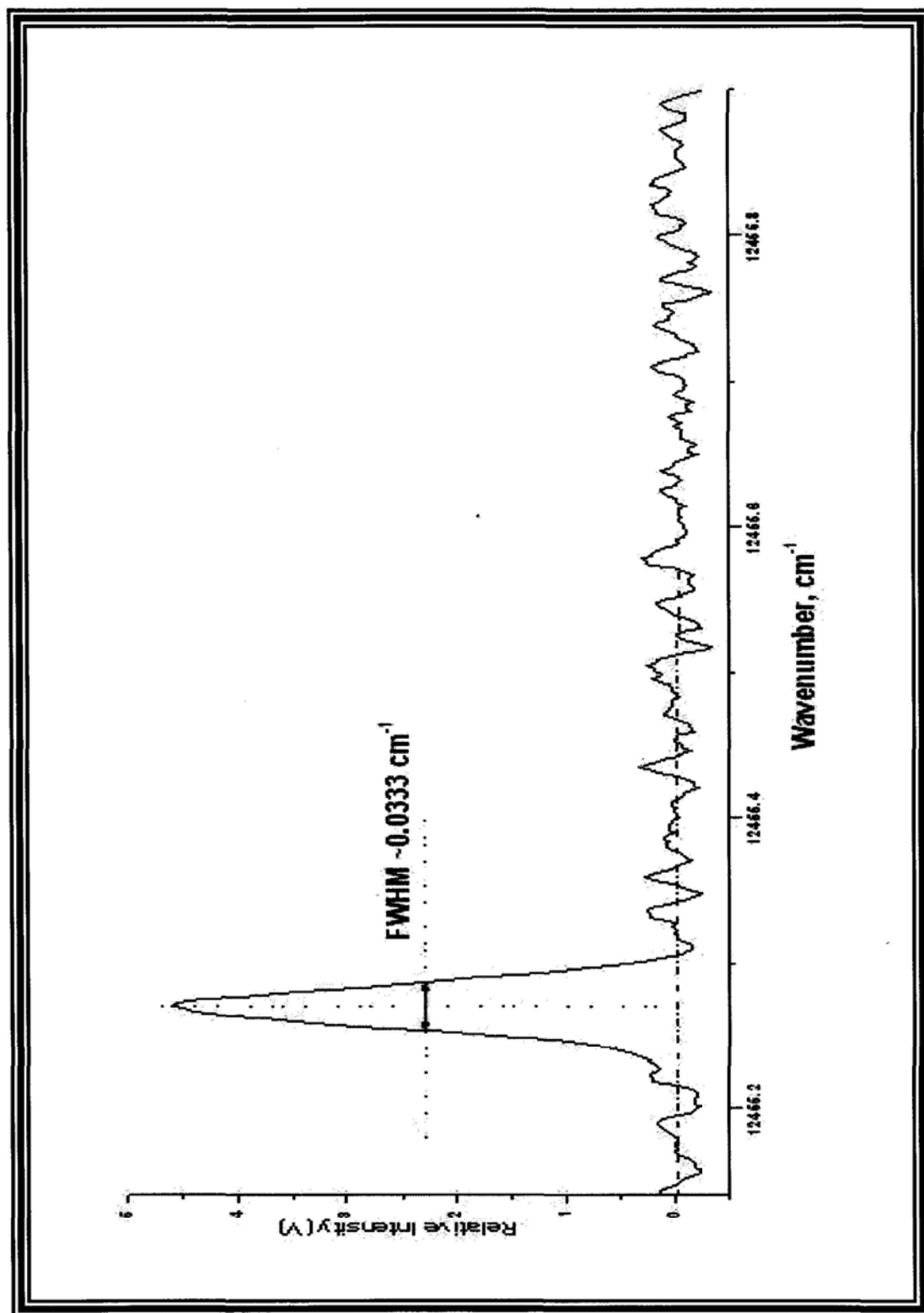
Fig. 54   Effect of isotopic substitution in unidentified bands at 12150 cm^{-1}.   The use of CD$_4$ replacing CH$_4$ gives no frequency shift in such transitions.
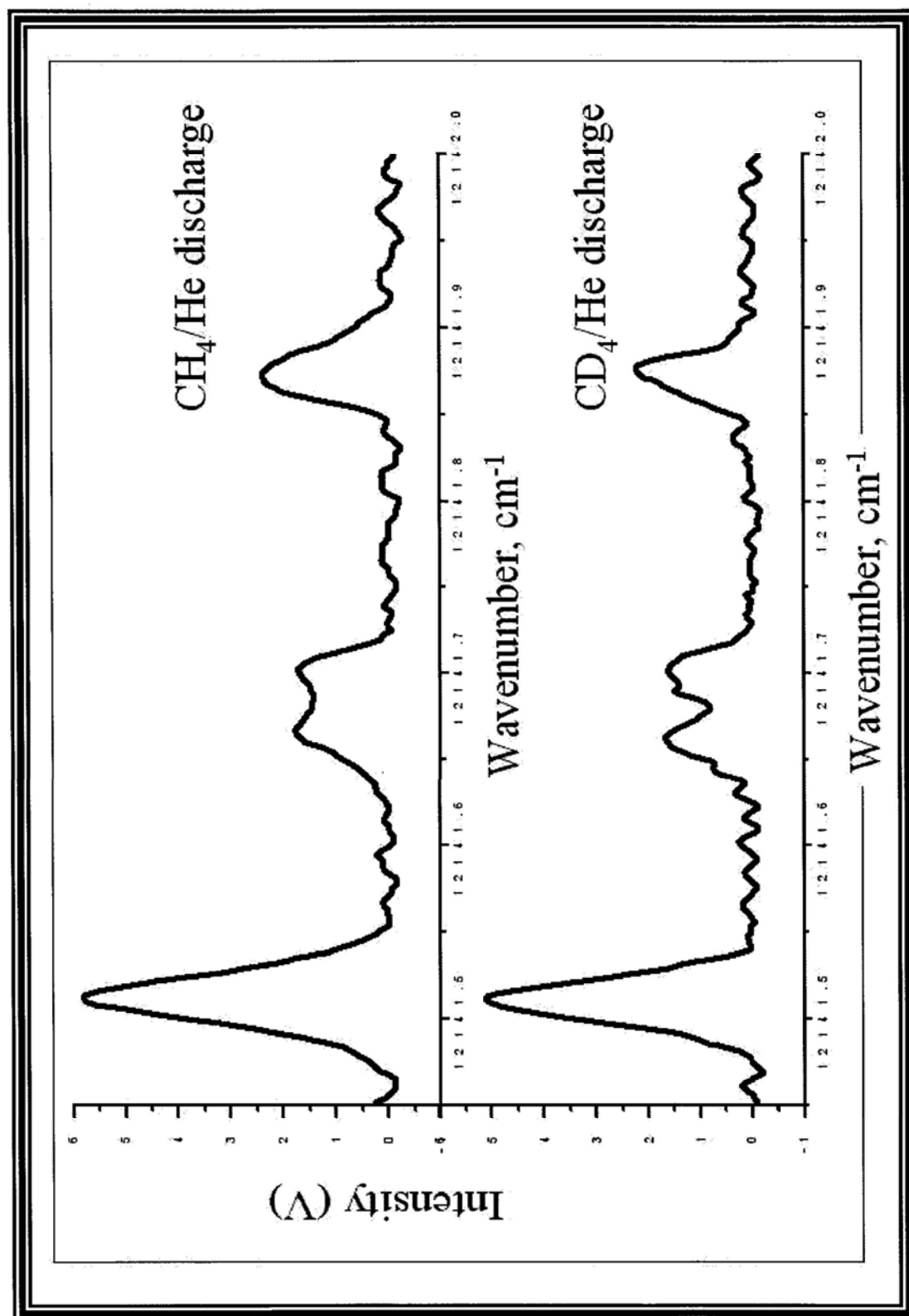
Fig. 55 Effect of isotopic substitution in unidentified bands at 12450 cm⁻¹. The use of CD₄ replacing CH₄ gives no frequency shift in such transitions.
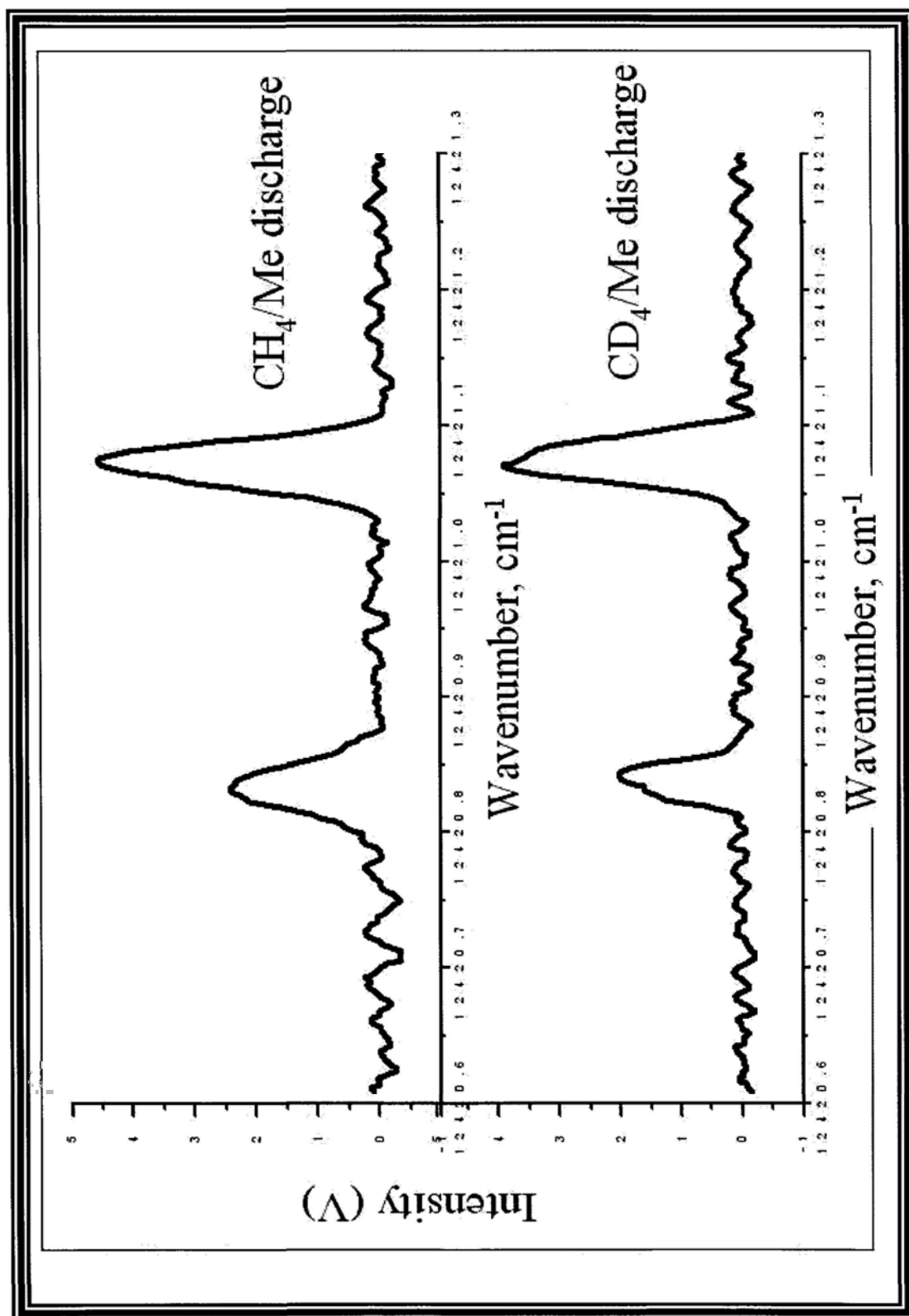
unprecedented accuracy. By combining the data from this work with those from Douay *et al.*,[53] a set of molecular constants is obtained from least-squares fitting. Due to high observed v levels in the $^{1}\Pi_{u}$ state, high order anharmonic constants $\omega_{e}z_{e}$ and $\omega_{e}a_{e}$ are obtained for the first time. These highly accurate parameters are useful for laboratory and astronomical studies.

Chapter 4

Discussion And Conclusion

4A Discharge Chemistry

In a gaseous plasma generated by high voltage discharges, a variety of reactions occur simultaneously and consecutively. These reactions include ionization and dissociation/fragmentation, ion-electron recombination and various ion-molecule reactions. To make things worse, the gas plasma is not at equilibrium state conditions. As a result, the detailed understanding of the dynamics, kinetics and mechanisms of the reactions in the plasma is next to impossible. Nevertheless, it is possible to have a grasp of the overall scheme of reactions based on the previous kinetic studies of various ion-molecule reactions in the gas phase.

Helium-dominated discharge plasma has been used in this work. Helium has been chosen for its inert chemical reactivity. Ground state helium atoms therefore are not expected to have reaction with the reactive species generated. On the other hand, the productions of reactive species are triggered by the reaction of helium atoms with the energetic electrons emitted from the cathode since helium is the most abundant species in the system. As atoms with full-filled electronic shell, helium has small proton affinity (only 1.9 eV)[60] and zero electron affinity. Since helium
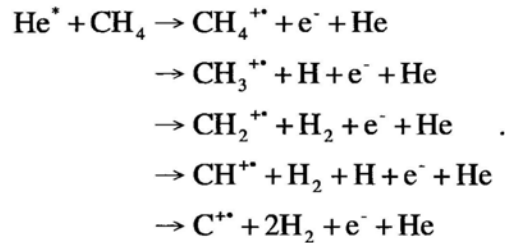
has the highest ionization potential (24 eV), it is difficult to ionize helium atom via

collision with high energy electrons from the cathode,

$$He + e^- \rightarrow He^+ + 2e^-.$$
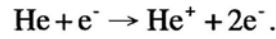
Instead, excitation of helium atoms to metastable states 2^3S and 2^1S (19.8 eV

and 20.6 eV, respectively) is expected,

$$He + e^- \rightarrow He^* + e^-.$$
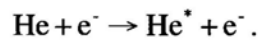
The radiative lifetimes of these excited metastable states are 9.0×10^3 seconds[61] and

1.97×10^{-2} seconds,[62] respectively.   Therefore, during the discharge, one of simulated

mechanisms is by using the metastable excited states of helium to ionize the CH_4 by

Penning ionization,

$$\begin{aligned}
He^* + CH_4 &\rightarrow CH_4^{+\bullet} + e^- + He \\
&\rightarrow CH_3^{+\bullet} + H + e^- + He \\
&\rightarrow CH_2^{+\bullet} + H_2 + e^- + He \\
&\rightarrow CH^{+\bullet} + H_2 + H + e^- + He \\
&\rightarrow C^{+\bullet} + 2H_2 + e^- + He
\end{aligned}$$

and C_2 is then generated from the recombination of $C^{+\bullet}$ and e^-,

$$2C^{+\bullet} + 2e^- \rightarrow C_2$$
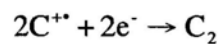
The formation of $C^{+\bullet}$ appears to be the rate determining step for the production of C_2

in the CH_4/He plasma.   Since the metastable helium atoms have less electronic

energy available for reaction compared to helium ions, the reaction products favor

less fragmentation.[63]   Hence, in our CH_4/He discharge, when the He* is reacted

with CH_4, $CH_4^{+\bullet}$ is more favorable product compared to other radicals or ions in the product distribution. It is unlikely that $C^{+\bullet}$ is formed in a one-step dissociation process. The low production in C_2 is therefore expected.

4B. Other plasma systems

In addition to the CH_4/He discharge, absorptions of other plasmas have also been recorded. In an attempt at improving the signals of C_2 Phillips system, C_2H_2/He plasma has also been studied. Not only the signals of the Phillips system have been improved but also the Swan system due to $d^3\Pi_g$ - $a^3\Pi_u$ has been observed. Spectrum in pure helium discharge has also been studied for a comparison with some unidentified broad lines observed in CH_4/He plasma. These observations also provide some insight to the chemistry in the plasma. While the detailed analysis of these spectra may take extensive time, some preliminary analysis are offered here.

(1) C_2H_2/He plasma

The production of C_2 in CH_4/He plasma requires the formation of C-C bond. This process is expected to be the rate determining step in the formation of C_2. The low concentration of CH_4 in the gas mixture limits the production efficiency. In order to improve the C_2 production, C_2H_2/He plasma has also been studied. Comparing to the case of CH_4, the formation of C_2 in C_2H_2/He plasma requires only

the removal of hydrogen atoms, which is expected to be much easier.

The optimization of discharge conditions has been carried as discussed in Chapter 3. It has been found that the optimized gas mixture and discharge conditions for the C_2H_2/He discharge is similar to those for CH_4/He plasma. In our experiments, we used a gaseous mixture of C_2H_2/He in a ratio of 1:170 with a total pressure of ~860 mTorr and carried out a discharge using 5 kHz *ac* at a peak current of ~1 A. Two frequency regions, namely as 12100-12500 cm^{-1} and 13750-14200cm^{-1}, have been scanned.

In general the absorption signals in the C_2H_2/He plasma are more than twice compared to those in the CH_4/He plasma (Fig. 56 and Fig. 57). As a result, many more weaker lines have been observed for the two unidentified bands centered at 12150 cm^{-1} and 12450cm^{-1} as shown in Fig. 58 and Fig. 59. This improvement will be crucial in the identification of the bands. Similar signal enhancement has also been observed in the 13750-14200cm^{-1} region (Fig. 60). It has been found that in addition to the Phillips system, vibronic bands in the Swan system of C_2 with $\Delta v = -4$ have also been observed with slightly weak intensity. The bands are expected to be very weak due to the small Franck–Condon factor as a result of large change in vibrational quantum number. In a preliminary analysis, four bands corresponding to (6-10), (5-9), (4-8) and (3-7) have been observed. Because of the perturbations

Fig. 56   Spectra comparison between the CH$_4$/He discharge and C$_2$H$_2$/He discharge at 12150 cm^{-1}.   There is a great improvement in signal intensity under C$_2$H$_2$/He discharge.
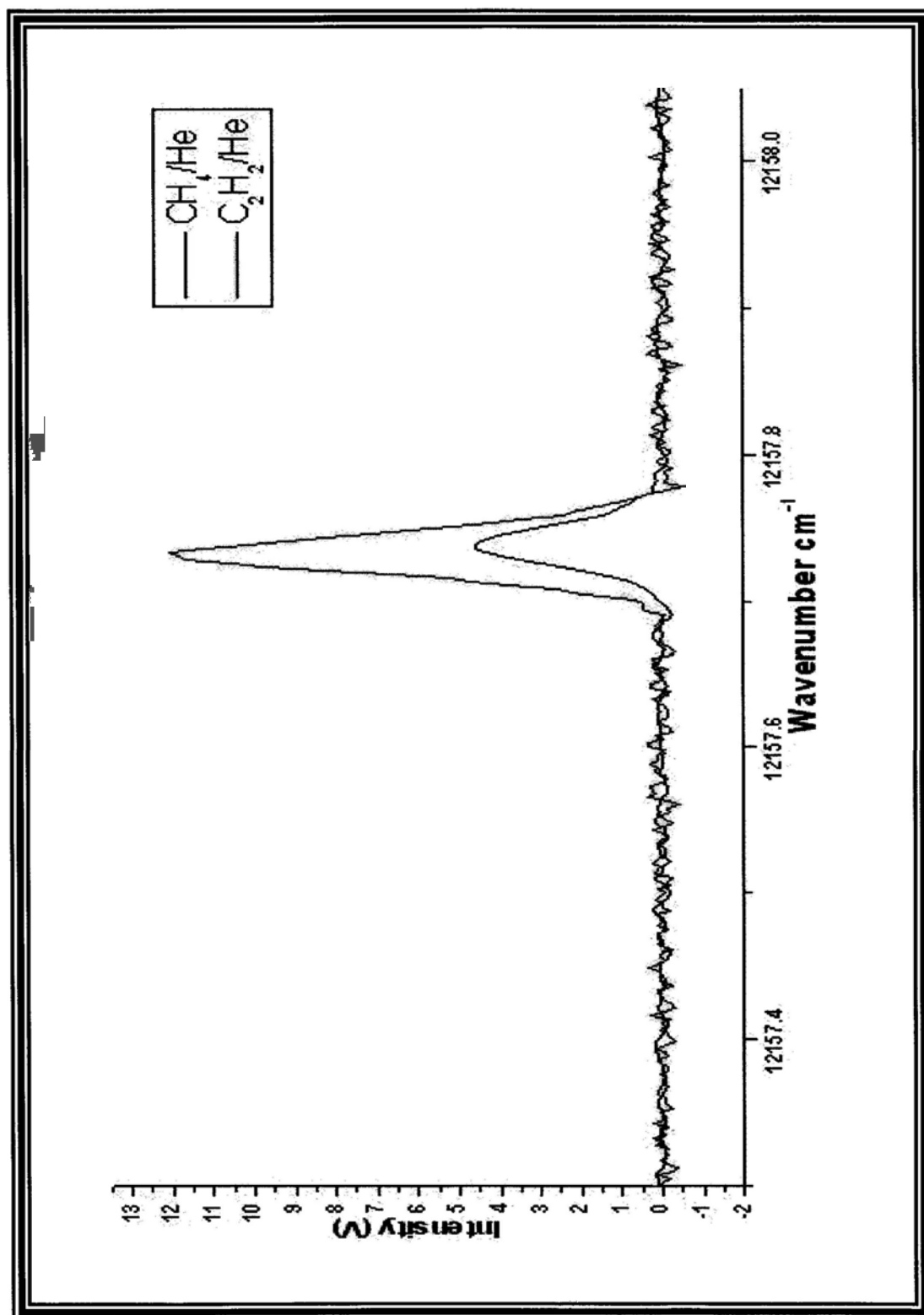
Fig. 57 Spectra comparison between the CH$_4$/He discharge and C$_2$H$_2$/He discharge at 12450 cm^{-1}. There is a great improvement in signal intensity under C$_2$H$_2$/He discharge.
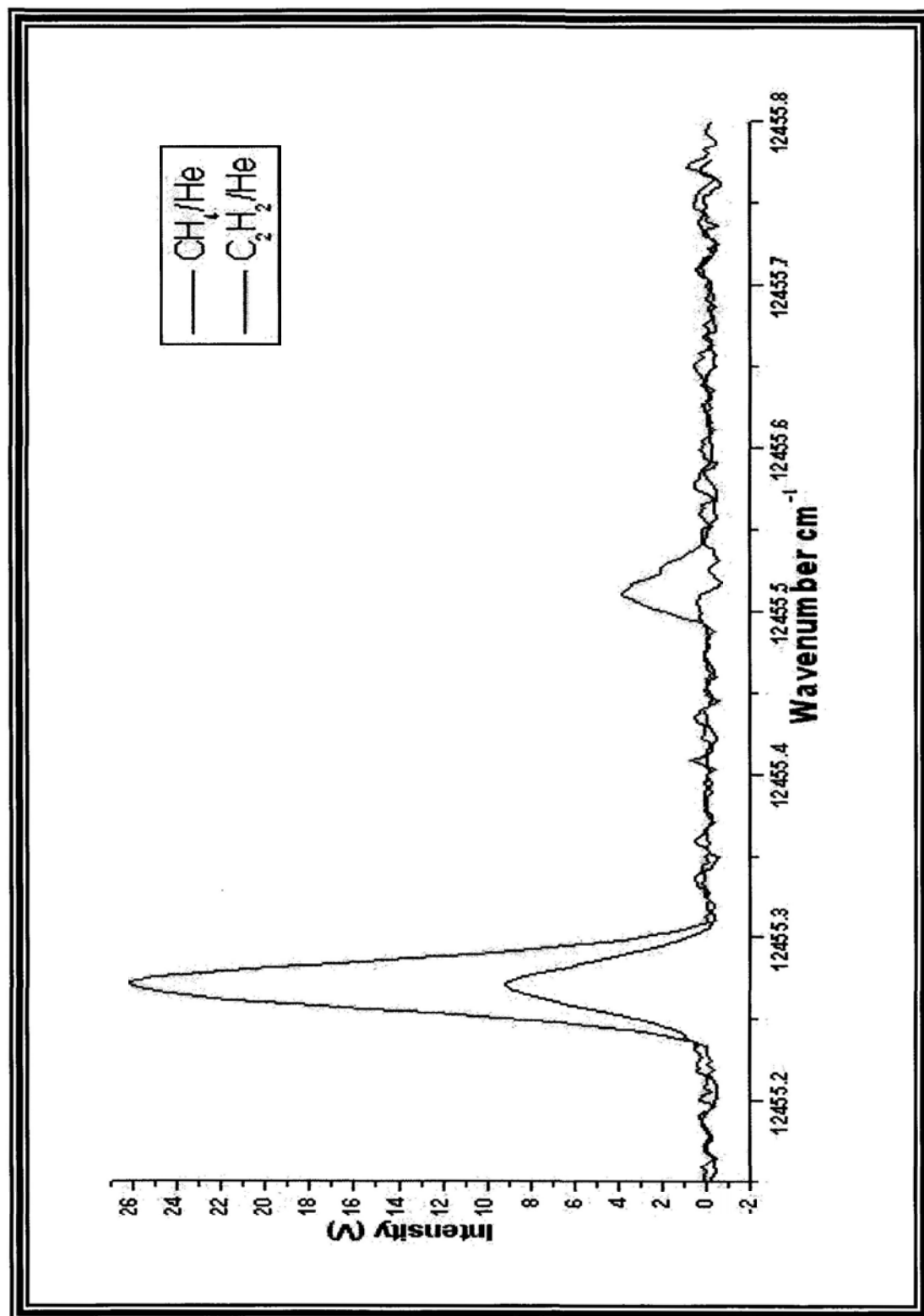
Fig. 58 Spectrum of unidentified bands at 12150 cm^{-1} under C_2H_2/He discharge.

Many transition lines are appeared by using C_2H_2/He discharge.
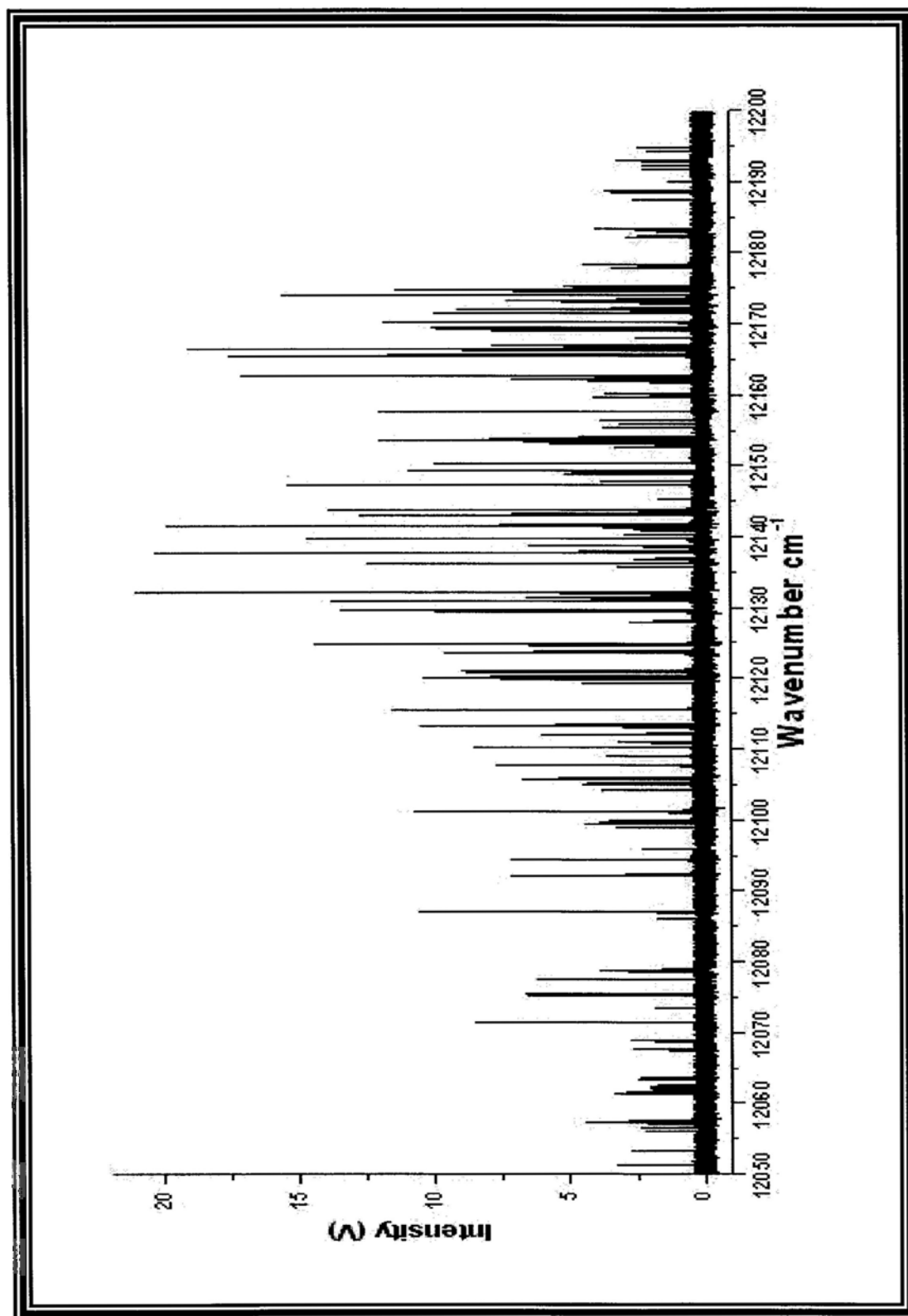
Fig. 59 Spectrum of unidentified bands at 12450 cm^{-1} under C_2H_2/He discharge.

Many transition lines are appeared by using C_2H_2/He discharge.
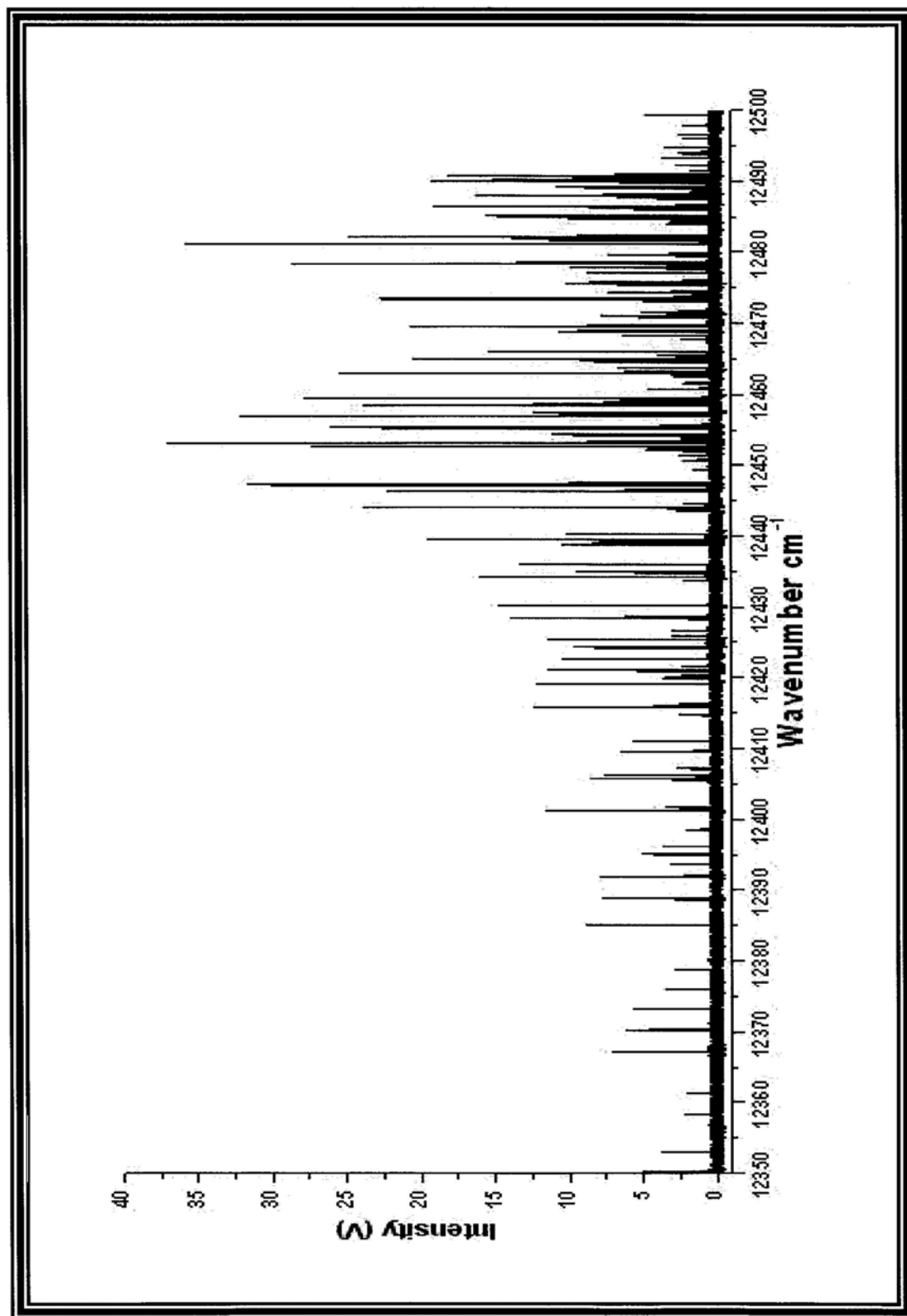
Fig. 60 Observation of vibronic bands in the 13750-14200cm^{-1} region by using C$_2$H$_2$/He discharge. In a preliminary analysis, four bands corresponding to (6-10), (5-9), (4-8) and (3-7) of the C$_2$ Swan system with Δv = -4 have been observed.
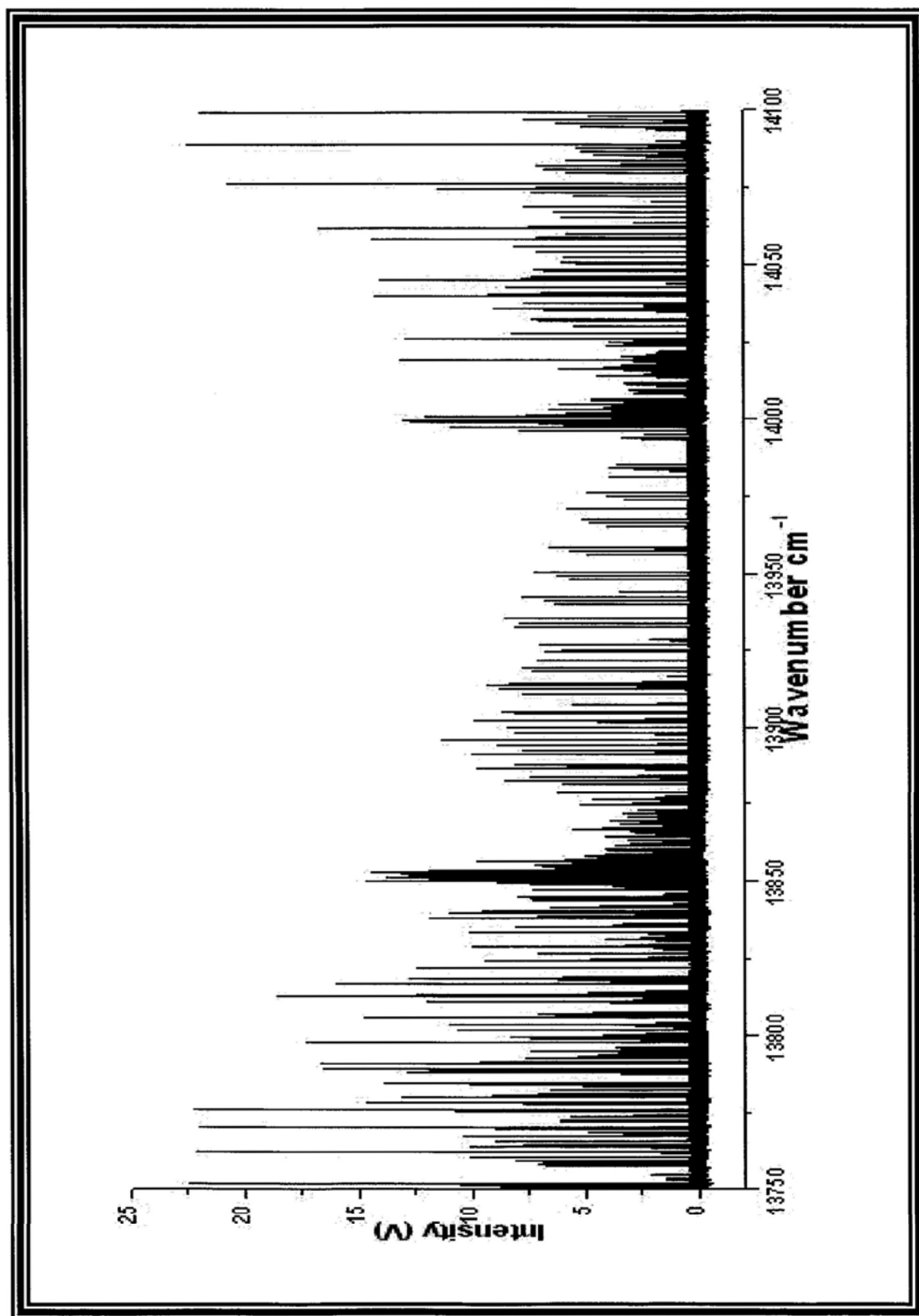
with other electronic states, the spectral pattern appears to be more complex than typical triplet-triplet transitions. Detailed analysis and assignment are underway to deduce the corresponding molecular parameters from least-squares fitting.

It is interesting to note that the C_2 observed in CH_4/He are solely in the X state while those observed in C_2H_2/He are in both X and A states. In the CH_4/He case, a C-C bond has to be formed in producing C_2. As a result, the electrons involved in the C-C bond formation are expected to pair up to form singlet state in the formation process. On the other hand, the formation of C_2 from C_2H_2 does not involve C-C bond formation. As a result, it is more likely that electrons involved in the C-C bonds are excited to form triplet states during the collision with energetic helium atoms.

(2) Pure helium plasma

In the CH_4/He gaseous discharge, we have observed about 80 transitions in the 10300-13000 cm^{-1} region in addition to the C_2 transition lines. These "board" transitions exhibited a typical linewidth of 0.6 cm^{-1} to 0.8 cm^{-1} (FWHM). Fig. 61 shows one of the examples at 12415.35 cm^{-1}. Assuming the observed linewidth to be Doppler-broadened, the corresponding mass of that species has been estimated to be about 4-8 gmol^{-1} based on the previous mentioned equation:

$$\Delta v_D = \frac{2v}{c}\sqrt{2\ln2 \times \frac{kT_{tran}}{m}}$$

Fig. 61   A "board" transition found in CH₄/He.   From its FWHM, we expect this transition is due helium containing species.
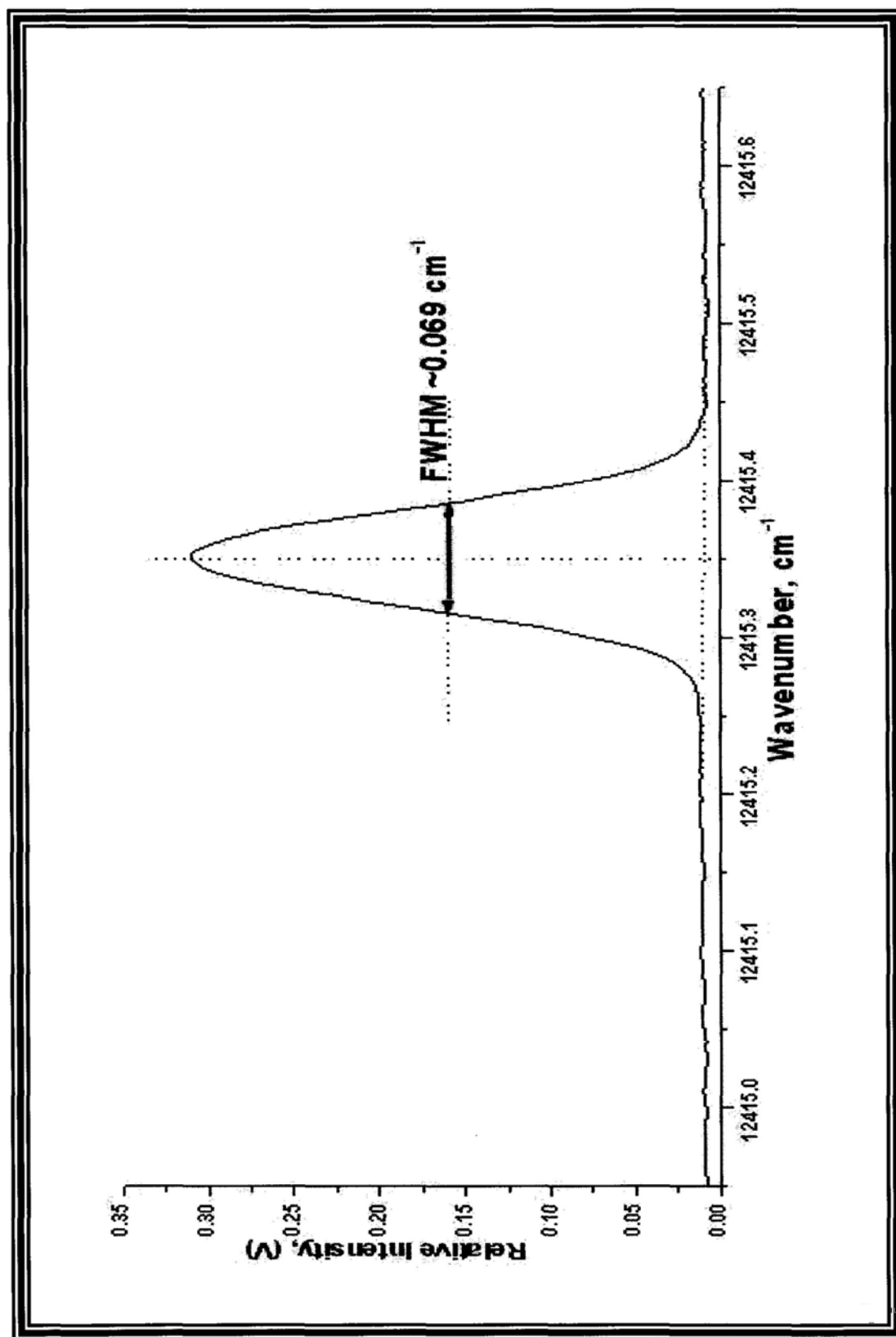
using a translational temperature of about 400 K. A number of species, namely Rydberg states of helium atom, HeH^+ or He_2 may give rise to these transitions. In order to further investigate the nature of the species, we have recorded the near infrared absorption of pure helium discharge in the 10300 cm^{-1} to 14250 cm^{-1} region. Fig. 62 shows the overall spectrum. It is seen that the spectrum is too condensed to be the rovibrational spectrum of helium-containing species. Based on the high density and complicated pattern of the lines, it is likely due to the bands of Rydberg states. Further experiments are necessary to clarify if He or He_2 are involved in the spectrum.

4C. Concluding Remarks

In summary, a number of state-of-the-art apparatus including a high resolution NIR laser spectrometer, a high power *ac* discharge power supply and a 2 m hollow cathode discharge cell have been custom-designed and built from scratch for spectroscopic studies of short-life species in gaseous plasmas. During the process, I was presented a rare opportunity to deal with various difficulties. This valuable exposure has helped me to develop from an inexperienced student into a researcher in the field.

In this thesis, the details of apparatus are discussed. The NIR laser

Fig. 62   Pure helium discharge in the 10300 cm⁻¹ to 14250 cm⁻¹ region.
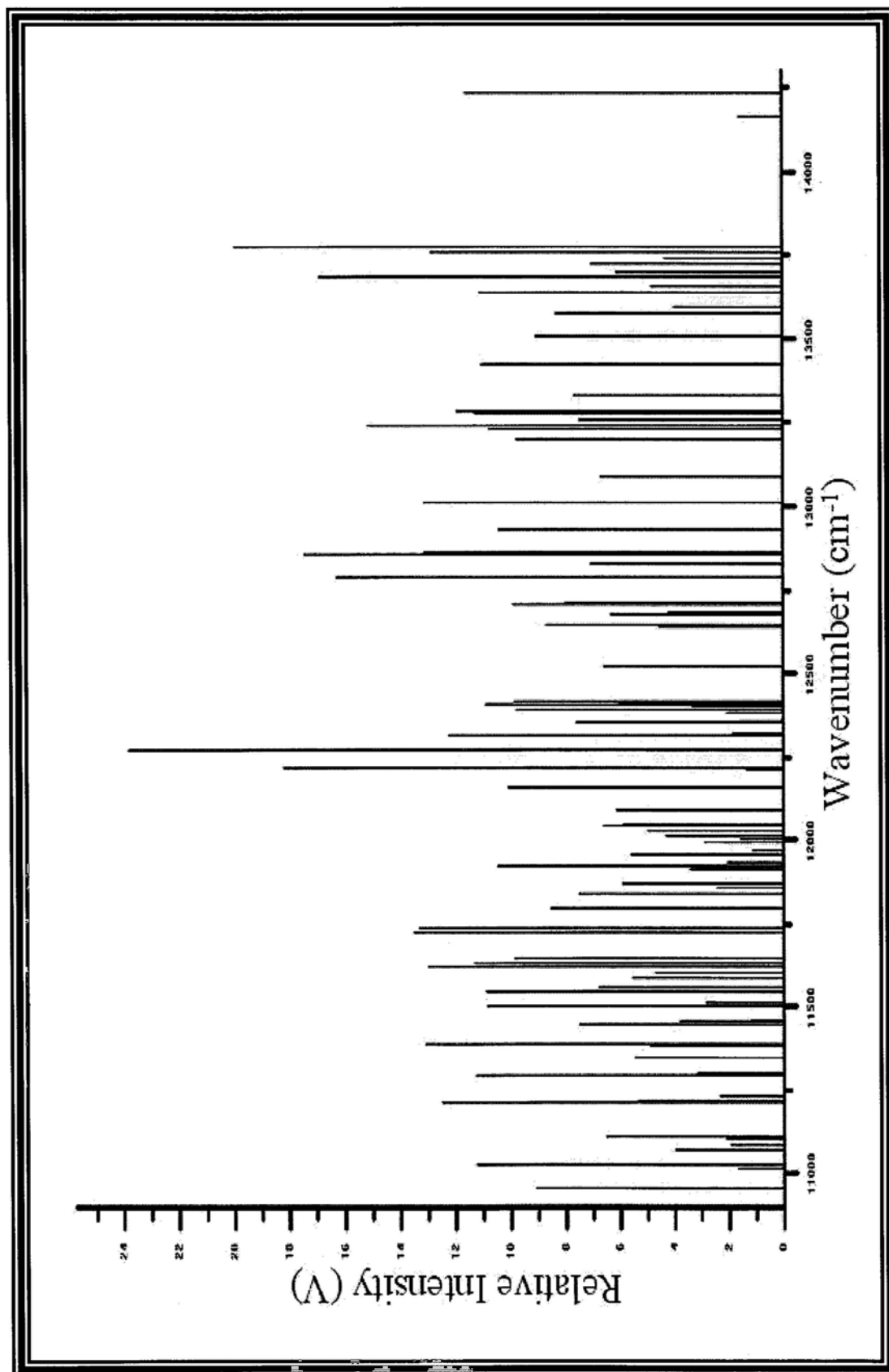
spectrometer is capable of measuring frequency with an accuracy of ~0.0010 cm^{-1}.

the high power *ac* discharge station allows a peak discharge current of up to 2.5 A.

The implementation of the zero-background concentration modulation detection

scheme affords a sensitivity of 1.2×10^{-6} in fractional absorption. The

unprecedented accuracy and sensitivity achieved by the system allows measuring

detailed spectra of ions and radicals in plasma generated in gaseous plasma.

As an illustration, the weak Phillips band system of C_2 has been observed using

near infrared laser absorption spectroscopy. A total 11 vibronic bands have been

measured. By combining the data from this work with those from Douay *et al.*,[53] a

new set of molecular constants with high accuracy have been obtained for laboratory

and astronomical studies.

Two unidentified bands have been observed at 12150 cm^{-1} and 12450 cm^{-1} in

both CH_4/He and C_2H_2/He plasmas. These bands are expected to be due to species

with two carbons based on the isotopic substitution and linewidths. The intricate

structure and high line density in the bands suggest they may be forbidden vibronic

bands involving states with high electronic spin. Analysis of these bands is

underway.

The apparatus built for these works can be used for studying other species such

as molecular ions and radicals in the nitrogen family and oxygen family.

Spectroscopic studies of these species will provide fundamental information in molecular structures and dynamics that will no doubt help the astronomical observations.

REFERENCES

[1]   See, for a review, A. D. Morgan *"Essays on the Life and Work of Newton"*, (The Open Court Publishing Company, Chicago and London, 1914).

[2]   G. Herzberg, *Molecular Spectra and Molecular Structure: 1. Spectra of Diatomic Molecules* (D. Van Nostrand Company Inc., New Jersey, 1950).

[3]   G. Herzberg, *Molecular Spectra and Molecular Structure: II. Infrared and Raman Spectra of Polyatomic Molecules* (D. Van Nostrand Company Inc., New Jersey, 1945).

[4]   G. Herzberg, *Molecular Spectra and Molecular Structure: III. Electronic Spectra and Electronic Structure of Polyatomic Molecules* (D. Van Nostrand Company Inc., New Jersey, 1967).

[5]   E. R. Menzel, *Laser spectroscopy: techniques and applications* (Dekker, New York, 1995).

[6]   N. L. Bauld, *Radicals, Ion Radicals, and Triplets* (Wiley-VCH, New York, 1997).

[7]   S. Scheiner, *Molecular Interactions: From van der Waals to Strongly Bound Complexes* (John Wiley & Sons Ltd., New York, 1997).

[8]   E. R. Dobbs, *Solid Helium Three* (Oxford University Press, London, 1993).

[9]   M. W. Crofton, M. F. Jagod, B. D. Rehfuss and T. Oka, *J. Chem. Phys.* **91**, 5139 (1989).

[10]   E. T. White, J. Tang and T. Oka, *Science* **284**, 135 (1999).

[11]   D. J. Liu and T. Oka, *Phys. Rev. Lett.* **54**, 1787 (1985).

[12]   G. Herzberg, *Nobel Lecture in Chemistry (1971-1980)* (World Scientific, Singapore, 1993).

[13]   A. Dalgarno, *NATO ASI Series* **6**, 341 (1974).

[14]   A. von Engel, *Ionized Gases* (Oxford University Press, London, 1955).

[15]   See, for an example, A. Tanabashi and T. Amano, *J. Mol. Spectrosc.* **215**, 285 (2002).

[16]   See, for an example, Y. A. Lebedev, M. V. Mokeev, P. V. Solomakhin, V. A. Shakhatov, A. V. Tatarinov, I. L. Epstein, *J. Phys. D: Appl. Phys.* **41**, 194001 (2008).

[17]   J. L. Gottfried, B. J. McCall and T. Oka, *J. Chem. Phys.* **118**, 10890 (2003).

[18]   K. Shimoda, *Introduction to Laser physics* (Springer Verlag, Berlin, 1986).

[19]   S. Gerstenkorn, J. Verges and J. Chevillard, *Atlas Du Spectre D'absorption De La Molecule D'iode* (Laboratoire Aimé Cotton, Orsay, 1982).

[20]   G. Hernandez, *Fabry-Perot Interferometers* (Cambridge University Press, London, 1986).

[21]   L. S. Rothman, C. P. Rinsland, A. Goldman, S. T. Massie, D. P. Edwards, J. M. Flaud, A. Perrin, C. Camy-Peyret, V. Dana, J. Y. Mandin, J. Schroeder, A. Mccann, R. R. Gamache, R. B. Wattson, K. Yoshino, K. V. Chance, K. W. Jucks, L. R. Brown, V. Nemtchinov and P. Varanasi, *J. Quant. Spectrosc. Radiat. Transfer* **60**, 665 (1998).

[22]   K. A. Rubinson and J. F. Rubinson, *Contemporary Instrumental Analysis* (Prentice Hall, New Jersey, 2000).

[23]   I. R. Dunkin, *Matrix-isolation Techniques: A Practical Approach* (Oxford University Press, London, 1998).

[24]   E. Whittle, D. A. Dows and G. C. Pimentel, *J. Chem. Phys.* **22**, 1943 (1954).

[25]   M. E. Jacox, *Rev. Chem. Intermed.* **2**, 1 (1978).

[26]   D. M. Hembree, E. R. Hinton, Jr., R. R. Kemmerer, G. Mamantov and E. L. Wehry, *Appl. Spectrosc.* **33**, 477 (1979).

[27]   J. U. White, *J. Opt. Soc. Am.* **32**, 285 (1942).

[28]   W. Demtröder, *Laser Spectroscopy* (Springer Verlag, Berlin, 1996).

[29]   W. F. Egan, *Phase-Lock Basics* (John Wiley & Sons Ltd., New York, 1998).

[30]   A. B. Meinel, *Astrophys. J.* **112**, 562 (1950).

[31]   M. Rösslein, C. M. Gabrys, M. F. Jagod and T. Oka, *J. Mol. Spectrosc.* **153**, 738 (1992).

[32] See, for reference, P. R. Bunker, *Molecular Symmetry and Spectroscopy* (Academic Press, New York, 1979).

[33] W. Pauli, *Z. Phys.* **31**, 765 (1925).

[34] M. Born and J. R. Oppenheimer, *Ann. Physik (Leipzig)* **84**, 457 (1927).

[35] See, for references, H. Eyring, J. Walter and G. E. Kimball, *Quantum Chemistry* (Wiley, New York, 1944).

[36] See, for example, J. W. Brault, L. Delbouille, N. Grevesse, G. Roland, A. J. Sauval and L. Testerman, *Astron. Astrophys.* **108**, 201 (1982).

[37] See, for example, B. E. Reddy, D. L. Lambert, G. Gonzalez and D. Yong, *Ap. J.* **564**, 482 (2002).

[38] See, for example, U. Fink and M. D. Hicks, *Ap. J.* **459**, 729 (1996).

[39] See, for example, C. Cecchi-Pestellini and A. Dalgarno, *Mon. Not. R. Astron. Soc.* **331**, L31 (2002).

[40] See, for example, J. A. Barnard and J. N. Bradley, *Frame and Combustion* 2nd ed. (Chapman and Hall, London, 1985).

[41] See, for references, K. P. Huber and G. Herzberg, *Molecular Spectra and Molecular Structure IV. Constants of Diatomic Molecules* (Van Nostrand Reinhold, New York, 1979).

[42] P. F. Fougere and R. K. Nesbet, *J. Chem. Phys.* **44**, 285 (1966).

[43] J. Barsuhn, *Z. Naturforsch. Teil A* **27**, 1031 (1972).

[44] J. O. Arnold, S. R. Langhoff, *J. Quant. Spectrosc. Radiat. Transfer* **19**, 461

(1978).

[45] K. Kirby and B. Liu, *J. Chem. Phys.* **70**, 893 (1979).

[46] D. M. Cooper and R. W. Nicholls, *J. Quant. Spectrosc. Radiat. Transfer* **15**,

139 (1975).

[47] E. Clementi, *Ap. J.* **132**, 898 (1960).

[48] J. G. Phillips, *Ap. J.* **107**, 389 (1948).

[49] E. A. Ballik and D. A. Ramsay, *Ap. J.* **137**, 84 (1963).

[50] I. R. Marenin and H. R. Johnson, *J. Quant. Spectrosc. Radiat. Transfer* **10**,

305 (1970).

[51] J. Chauville, J. P. Maillard and A. W. Mantz, *J. Mol. Spectrosc.* **68**, 399

(1977).

[52] S. P. Davis, M. C. Abrams, J. G. Phillips and M. L. P. Rao, *J. Opt. Soc. Am. B*

5, 10 (1988).

[53] M. Douay, R. Nietmann and P. F. Bernath, *J. Mol. Spectrosc.* **131**, 250 (1988).

[54] See, for references, R. C. Johnson, *An Introduction to Molecular Spectra*

(Methuen and Co., Ltd., London, 1949).

[55] P. H. Dwivedi, D. Branch, J. N. Huffaker and R. A. Bell, *Ap. J. S. S.* **36,** 573

(1978).

[56]   See, for references, K. A. Dill and S. Bromberg, *Molecular Driving Forces:*

Statistical Thermodynamics In Chemistry And Biology (Taylor & Francis.,

London, 2002).

[57]   M. C. Chan, S. H. Yeung, Y. Y. Wong, Y. Li, W. M. Chan and K. H. Kim,

Chem. Phys. Lett. **390**, 340 (2004).

[58]   See, for example, H. Meißner and I. Ema, *J. Mol. Struct. (Theochem)* **547**,

171 (2001).

[59]   B. D. Rehfuss, D. J. Liu, B. M. Dinelli, M. F. Jagod, W. C. Ho, M. W. Crofton

and T. Oka, *J. Chem. Phys.* **89**, 129 (1988).

[60]   W. T. Huntress, Jr., *Ap. J. S. S.* **33,** 495 (1977).

[61]   J. R. Woodworth and W. H. Moos, *Phys. Rev. A* **12,** 2455 (1975).

[62]   R. S. VanDyck, C. E. Johnson and H. A. Shugart, *Phys. Rev. Lett.* **25,** 1403

(1970); *Phys. Rev. A* **4,** 1327 (1971).

[63]   B. D. Rehfuss, *PhD. Thesis*, The University of Chicago (1990).